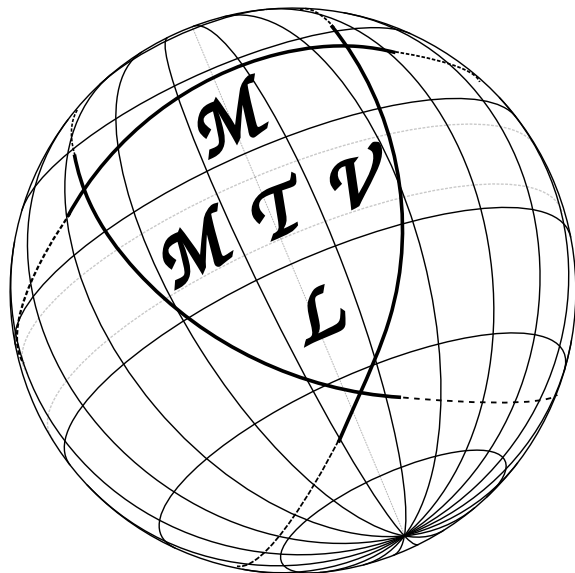


A FAST C++ TEMPLATE LIBRARY FOR TOTAL  
VARIATION MINIMIZATION OF MANIFOLD-VALUED TWO-  
AND THREE-DIMENSIONAL IMAGES



Master Thesis

*written by*  
Pascal Debus

*supervised by*  
Markus Sprecher,  
Prof. Dr. Philipp Grohs  
Seminar for Applied Mathematics  
ETH Zurich

October 1, 2015

## Abstract

In this thesis, a versatile, multi-threaded C++ template library for total variation (TV) minimization of manifold-valued image data is introduced. The library implements two minimizers: the iteratively reweighted least squares (IRLS) algorithm using the Riemannian Newton method for the optimization step and the proximal point algorithm. Pixels can take values in Euclidean space, on the Sphere, the special orthogonal group, the set of positive definite matrices and the Grassmann manifold while images can be either two- or three-dimensional. Some semi-analytic expressions for the derivatives of the squared distance functions using Kronecker products and a short overview about the relevant Grassmann manifold theory is provided along with a high level documentation of the library and its design concepts. The last part demonstrates the library's capabilities on different applications in image and video processing, medical imaging and computer vision. Performance is measured and compared for the IRLS and the proximal point implementations. Lastly the influence of the noisy original data on the the minimizer is investigated.

**Key words.** total variation minimization, manifold-valued data, iteratively reweighted least squares, proximal point algorithm, Riemannian Newton method

# Contents

<b>List of Figures</b>	<b>4</b>
<b>List of Tables</b>	<b>5</b>
<b>List of Algorithms</b>	<b>6</b>
<b>List of Abbreviations</b>	<b>7</b>
<b>1 Introduction</b>	<b>8</b>
1.1 Grayscale images . . . . .	8
1.1.1 Edge preservation . . . . .	9
1.1.2 Discretization . . . . .	9
1.2 Color images . . . . .	10
1.3 Manifold-valued images . . . . .	10
1.4 Objective and outline of this thesis . . . . .	10
<b>2 Theory</b>	<b>12</b>
2.1 Generalization of the functional . . . . .	12
2.1.1 The Riemannian distance . . . . .	12
2.2 Algorithms . . . . .	13
2.2.1 Proximal point . . . . .	13
2.2.2 Iteratively reweighted least squares . . . . .	14
2.3 Riemannian Newton method . . . . .	15
2.3.1 Gradient . . . . .	15
2.3.2 Hessian . . . . .	16
2.3.3 Newton equation . . . . .	16
2.3.4 Newton equation for the TV functional . . . . .	17
2.3.5 Tangent space restriction . . . . .	18
2.4 Manifolds . . . . .	18
2.4.1 Euclidean space . . . . .	18
2.4.2 Sphere $S^n$ . . . . .	19
2.4.3 Special orthogonal group SO(n) . . . . .	20
2.4.4 Symmetric positive definite matrices SPD(n) . . . . .	21
2.4.5 Grassmannian Gr(n,p) . . . . .	22
2.5 Fréchet derivatives of matrix logarithm and square root . . . . .	27
2.5.1 Derivative of the matrix square root . . . . .	27
2.5.2 Derivative of the matrix logarithm . . . . .	28

<b>3 The Manifold Total Variation Minimization Template Library</b>	<b>29</b>
3.1 Capabilities . . . . .	29
3.2 Design concepts . . . . .	30
3.2.1 Goals . . . . .	30
3.2.2 Levels of parallelization . . . . .	32
3.2.3 C++ techniques . . . . .	33
3.3 Components . . . . .	34
3.3.1 Manifold class . . . . .	35
3.3.2 Data class . . . . .	37
3.3.3 Functional class . . . . .	38
3.3.4 TV minimizer class . . . . .	39
3.3.5 Visualization class . . . . .	39
3.3.6 Utility functions . . . . .	41
3.4 Using MTVMTL . . . . .	42
3.4.1 Prerequisites . . . . .	42
3.4.2 Installation . . . . .	43
3.4.3 Compilation of own projects using CMake . . . . .	43
3.4.4 Tutorial and typical use cases . . . . .	45
<b>4 Applications and Numerical Experiments</b>	<b>49</b>
4.1 Image denoising . . . . .	49
4.1.1 Grayscale . . . . .	49
4.1.2 Color . . . . .	50
4.1.3 Inpainting . . . . .	51
4.1.4 Recolorization . . . . .	51
4.1.5 Volume images . . . . .	52
4.2 SO(2) and SO(3) image data . . . . .	53
4.2.1 Synthetic data . . . . .	53
4.2.2 Fingerprint orientation data . . . . .	54
4.2.3 Reconstruction of a dense optical flow field . . . . .	54
4.3 SPD(3) image data . . . . .	55
4.3.1 Synthetic data . . . . .	55
4.3.2 Diffusion Tensor Magnetic Resonance Imaging . . . . .	56
4.3.3 3D DT MRI data . . . . .	57
4.4 Gr(3,1) image data . . . . .	58
4.4.1 Chromaticity denoising . . . . .	58
4.5 Performance analysis of the library . . . . .	58
4.5.1 Profiling . . . . .	59
4.5.2 Time complexity . . . . .	60
4.6 Comparison IRLS and Proximal Point minimizers . . . . .	62
4.7 Sensitivity to variations of the original data . . . . .	65
<b>5 Conclusion and Outlook</b>	<b>67</b>
5.1 Summary . . . . .	67
5.2 Extensions and improvements . . . . .	68
5.2.1 Performance . . . . .	68
5.2.2 Manifolds and minimizers . . . . .	68
5.2.3 Functionals . . . . .	68
5.3 Recursive computation on subdomains . . . . .	69
<b>Acknowledgements</b>	<b>71</b>
<b>A Listings</b>	<b>72</b>
<b>B Derivative Computations</b>	<b>77</b>
B.1 Vectorization-Kronecker-product identities . . . . .	77
B.2 Squared distance function on the special orthogonal group $SO(n)$ . . . . .	77

<b>C Performance metrics</b>	<b>79</b>
C.1 Cache Misses . . . . .	79
C.2 Page Faults . . . . .	80

# List of Figures

1.1	Comparison total variation . . . . .	9
2.1	Affine cross section map . . . . .	24
2.2	Vertical and horizontal spaces . . . . .	25
3.1	Calculation using pixel-wise kernels . . . . .	33
3.2	SIMD parallelization . . . . .	33
3.3	Overview of library components . . . . .	35
3.4	$SO(3)$ cube visualization . . . . .	40
3.5	$SPD(3)$ ellipsoid visualization . . . . .	41
3.6	3D $SPD(3)$ Volume Visualization of a helix . . . . .	41
3.7	3D Volume image renderer . . . . .	41
4.1	Color image "Cameraman" grayscale denoising . . . . .	49
4.2	Color image "Lena" linear vectorial denoising . . . . .	50
4.3	Large image "mathematicians" linear-vectorial denoising . . . . .	50
4.4	Large image "crayons" CBR-vectorial denoising . . . . .	51
4.5	Denoising linear vectorial . . . . .	51
4.6	Recolorization . . . . .	52
4.7	Denoising 3D Grayscale Volume Data PRPT . . . . .	52
4.8	Denoising 3D Grayscale Volume Data IRLS . . . . .	53
4.9	Inpainting of synthetic $SO(3)$ picture . . . . .	53
4.10	Fingerprint orientation denoising . . . . .	54
4.11	Dense optical flow reconstruction . . . . .	55
4.12	Denoising of synthetic $SPD(3)$ picture . . . . .	56
4.13	Denoising DT-MRI data . . . . .	57
4.14	Denoising 3D DTI-MRI data . . . . .	57
4.15	Color denoising . . . . .	58
4.16	Large image "crayons" CBR-vectorial denoising . . . . .	58
4.17	Time complexity IRLS $\mathbb{R}^3$ and $SPD(3)$ . . . . .	61
4.18	Test images . . . . .	62
4.19	Comparison IRLS & PRPT for Euclidean $\mathbb{R}^3$ and $S^2$ . . . . .	63
4.20	Comparison IRLS & PRPT for Euclidean $SO(3)$ . . . . .	64
4.21	Comparison IRLS & PRPT for $SPD(3)$ . . . . .	64
4.22	Comparison IRLS & PRPT for $Gr(3, 1)$ . . . . .	65
4.23	Sensitivity to variation . . . . .	66
5.1	Splitting the image domain . . . . .	69
5.2	Comparison full domain versus splitted domain denoising . . . . .	69

# List of Tables

2.1	Comparison vector space and manifold operations . . . . .	13
4.1	Share of total CPU cycles $M = \mathbb{R}^3$ . . . . .	59
4.2	Share of total CPU cycles $SPD(3)$ . . . . .	60
4.3	Share of total CPU cycles $SPD(3)$ , $300 \times 300$ pixel . . . . .	61

# List of Algorithms

2.1	Parallel proximal point algorithm . . . . .	15
2.2	IRLS algorithm . . . . .	16
2.3	Riemannian Newton method for real-valued functions . . . . .	17

# List of Abbreviations

**AVX** advanced vector extensions.

**BLAS** basic linear algebra subprograms.

**CBR** chromaticity-brightness.

**CGAL** computational geometry algorithms library.

**CSV** comma-separated values.

**CT** computer tomography.

**DTI** diffusion tensor imaging.

**DT-MRI** diffusion tensor magnetic resonance imaging.

**DW-MRI** diffusion weighted magnetic resonance imaging.

**GLEW** OpenGL extension wrangler library.

**GLUT** OpenGL utility toolkit.

**IRLS** iteratively reweighted least squares.

**MRI** magnetic resonance imaging.

**MTVMTL** Manifold total variation minimization library.

**NIfTI** neuroimaging informatics technology initiative.

**OMP** OpenMP.

**OpenCV** open computer vision.

**OpenGL** open graphics library.

**PRPT** proximal point.

**SIMD** single instruction multiple data.

**SO** special orthogonal.

**SPD** symmetric positive definite.

**SSE** streaming SIMD extensions.

**TV** total variation.

**VPP** Video++.

# Chapter 1

## Introduction

Various forms of noise occur in many forms of data acquisition, transmission and processing. This noise needs to be removed in order to obtain a meaningful interpretation of the data, to enable further processing or, as in many image processing applications, just for aesthetic reasons. A common everyday example for a noisy image is taking a picture with a digital camera (e.g. integrated in a smart phone) in a weakly illuminated room: Especially the dark areas of the picture are not uniform in color and brightness, but have small variations from pixel to pixel.

A noise removal algorithm needs to remove these small variations, but at the same time not alter important features of the data. In the case of images, important features are for example the edges, separating areas of different colors, which provide the necessary sharpness of the picture. These edges are characterized by large variations. The distinction between small and large variations is also helpful in the task of inpainting, which tries to restore the picture at unknown or damaged regions.

The method of total variation (TV) noise removal, which has the above described capabilities, was first introduced by Rudin, Osher and Fatemi [27] in 1992 for the case of real-valued, that means grayscale images. Their method is briefly summarized in the following section.

### 1.1 Grayscale images

Let  $u_0 : \mathbb{R} \supset \Omega \rightarrow \mathbb{R}$  describe the original, noise-free image where the image domain  $\Omega$  is usually a rectangular or cuboid subset of  $\mathbb{R}^2$  or  $\mathbb{R}^3$ , respectively. Assuming the original picture is corrupted by Gaussian noise  $n : \Omega \rightarrow \mathbb{R}$  with zero mean and variance  $\sigma^2$ , the noisy picture is given by  $u : \Omega \rightarrow \mathbb{R}$  where  $u = u_0 + n$ . The edge-preserving denoising of the picture is then equivalent to the solution  $u^* : \Omega \rightarrow \mathbb{R}$  of the following constrained optimization problem:

$$u^* = \operatorname{argmin}_{f:\Omega \rightarrow \mathbb{R}} \int_{\Omega} |\nabla u| dx \quad \text{s.t.} \quad (1.1)$$

$$\int_{\Omega} (u - u_0) dx = 0, \quad \text{and} \quad \int_{\Omega} (u - u_0)^2 dx = \sigma^2 \quad (1.2)$$

The first term,  $TV(u) = \int_{\Omega} |\nabla u| dx$ , is called the total variation of  $u$ . Rudin, Osher and Fatemi then use a partial differential equation (PDE) approach to solve the corresponding Euler-Lagrange equation for (1.1). Later, Chambolle and Lions [11] showed that (1.1) is equivalent to the minimization of the functional

$$J(u) = \frac{1}{2} \|u - u_0\|_2^2 + \lambda \int_{\Omega} |\nabla u| dx. \quad (1.3)$$

### 1.1.1 Edge preservation

A basic intuition why the  $L^1$  norm in (1.3) is better suited for conserving sharp discontinuities, such as edges, can be seen from the following plot, taken from [32]. Discretize the unit interval by setting  $x_i = i/N$  for  $i = 0, \dots, N := 100$  and define the finite differences  $(\Delta f)_i = f(x_{i+1}) - f(x_i)$ , where  $f$  is continuous and monotone on  $[0, 1]$  and satisfies  $f(0) = 0$  and  $f(1) = 1$ . Some possible  $f$  are shown in 1.1. Finally, define discretized versions,  $l^1$  and  $l^2$ , for the squared  $L^1$  and  $L^2$  norms of the gradient by  $l^p(\Delta f) := \sum_{i=0}^{N-1} |(\Delta f)_i|^p$  where  $p = 1, 2$ .

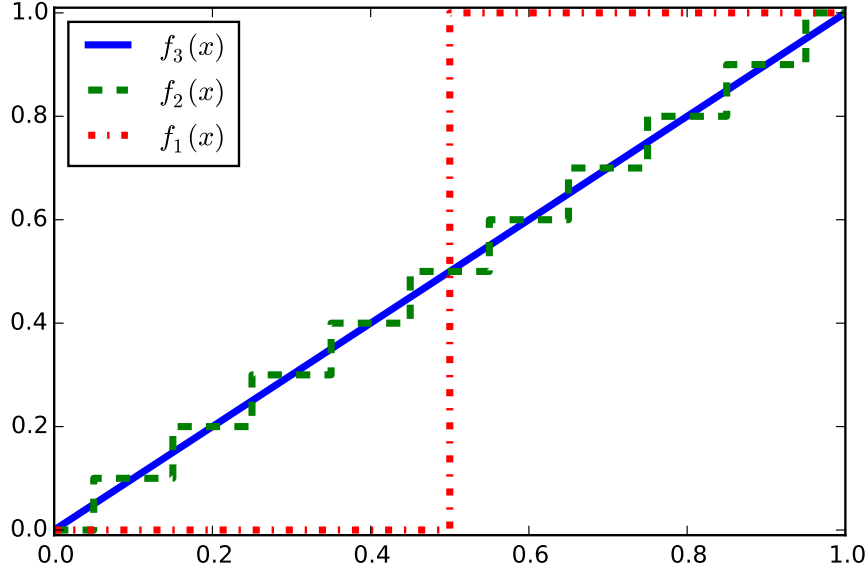


Figure 1.1: Plots of three functions with ( $N = 1, 10, 100$ ) steps and a total variation equal to 1.0

Function	$l^1(\Delta f_i)$	$l^2(\Delta f_i)$
$f_1$	1.0	1.0
$f_2$	1.0	0.1
$f_3$	1.0	0.01

One can see that the  $l^2$  variation term favours continuous transitions, such as  $f_3$ , rather than the sudden jump in  $f_1$  whereas the total variation is the same for all cases.

### 1.1.2 Discretization

For a grayscale image  $u : \Omega \subset \mathbb{R}^2 \rightarrow \mathbb{R}$  a discrete grid of pixels  $\Omega = \{1, 2, \dots, m\} \times \{1, 2, \dots, n\} \subset \mathbb{R}^2$  is chosen. The picture  $u$  then takes the values  $u_{i,j} := u((i, j)) \in [0, 1]$  at the points  $(i, j) \in \Omega$ , and a forward finite difference discretization of the gradient  $\nabla u := (u_x, u_y)^T$  can be used, where

$$(u_x)_{i,j} = \begin{cases} u_{i,j+1} - u_{i,j}, & 1 \leq j < n \\ 0, & j = n \end{cases} \quad (1.4)$$

$$(u_y)_{i,j} = \begin{cases} u_{i+1,j} - u_{i,j}, & 1 \leq i < m \\ 0, & i = m \end{cases}.$$

This leads to the *isotropic* TV functional

$$TV_{iso}(u) = \sum_{i,j} \sqrt{(u_{i+1,j} - u_{i,j})^2 + (u_{i,j+1} - u_{i,j})^2}. \quad (1.5)$$

This TV term corresponds to the formulation originally proposed by Rudin et al [27], where  $|\nabla u| = \sqrt{u_x^2 + u_y^2}$ . Another possibility is the *anisotropic* version of the functional, which allows for more flexibility in the reweighting process, described in 2.2.2, and is even necessary for the proximal point algorithm, described in 2.2.1. It is given by

$$TV_{aniso}(u) = \sum_{i,j} |u_{i+1,j} - u_{i,j}| + |u_{i,j_1} - u_{i,j}|. \quad (1.6)$$

To obtain the final expression for the functional, the 2-norms of the pixel-wise differences to the original picture  $u_0$  need to be added

$$J(u) = \sum_{i,j} (u_{i,j} - (u_0)_{i,j})^2 + \lambda TV(u). \quad (1.7)$$

## 1.2 Color images

The next step in the development of image denoising algorithms was their generalization to color images. From a mathematical perspective this just means considering pictures from  $\Omega \rightarrow C \simeq \mathbb{R}^3$  where the form and additional properties of  $C$  depend on the chosen color model.

In the most simple case of linear models, RGB for instance, one could choose  $C$  as  $[0, 1]^3$  and consider denoising each component individually (channel-by-channel model) or consider  $\mathbb{R}^3$  as a normed vector space of tuples  $(x_R, x_G, x_B)$  (linear-vectorial model).

Among the nonlinear models, the so-called chromaticity-brightness model, investigated by Chan et al [12], shows the closest resemblance to human perception. In this case, take  $C = S^2 \times [0, 1]$  such that the chromaticity takes values on the sphere  $S^2$  considered as a submanifold of the Euclidean space  $\mathbb{R}^3$ , while the brightness is real-valued, as in the case of grayscale images.

## 1.3 Manifold-valued images

Just by changing the color model from a linear to a non-linear one, pixels become non-trivially manifold-valued. Apart from non-linear color models, more complicated data arises in a variety of applications such as Diffusion Tensor Magnetic Resonance Imaging (DT-MRI), computer vision and robotics to name just a few. In most cases this data can be represented by matrices such that the pixels become matrix-valued as well.

In addition to that, the model underlying the data and the process of data acquisition result in a set of constraints imposed on the matrices. The set of matrices defined by those constraints often allows for a differentiable structure, thus enabling geometric optimization methods. For most types of manifold-data also "edges" in the data, for example between two neighboring, homogeneous areas of different orientations in the case of  $SO(3)$  data, are considered a feature that needs to be preserved. Since also manifold-valued data is subject to noise, the generalization of the algorithm to manifold-valued data is the next logical step.

## 1.4 Objective and outline of this thesis

In this thesis, the Manifold Total Variation Minimization Template Library (MTVMTL), an extendable multi-threaded C++ template library for the purpose of TV minimization of manifold-valued images, is introduced. The implemented minimization algorithms are based on the iteratively reweighted least squares (IRLS) adaption suggested by Sprecher and Grohs [16] as well as a proximal point algorithm by Weinmann et al [33]. The implementation is extended to 3D image cubes, the Grassmann manifold and also some quasi-analytic expressions for derivatives of the Riemannian distance function are provided.

The following Chapter 2 provides a short summary of the necessary theory, a description of the algorithms and relevant properties for each of the implemented manifolds. After that, Chapter 3

introduces the library itself and in particular its capabilities, design concepts, structure, installation and usage in the form of some typical use cases. In Chapter 4 numerical experiments are conducted, showing various application of the library as well as convergence behavior and comparisons between IRLS and proximal point based algorithms. Finally, chapter 5 concludes with possible extensions and adaptions of the library, in particular the possibility of recursive splitting of the image domain into smaller subproblems and the transition to distributed architectures.

# Chapter 2

## Theory

### 2.1 Generalization of the functional

The functional defined in (1.7) needs a vector space structure for differences to make sense. Hence, the functional must be transformed to be still valid in the more general setting of manifold-valued pixels. Since  $|x - y| = d(x, y)$  for the Euclidean distance on  $\mathbb{R}$ , the generalization to metric spaces  $(X, d)$  is the appropriate way to proceed.

To also include the case of 3D pictures and shorten the notation, a graph  $G$  is used to specify over which pairs of pixels the sums in (1.7) are taken. Let  $V$  be an index set of all pixels in our picture. Denote by  $E \subset V \times V$  the set of directed edges in  $G$  and by  $n(i) := \{j \in V : (i, j) \in E\}$  the set of  $i$ 's neighbors. Then

$$TV_{iso}(u) = \sum_{i \in V} \sqrt{\sum_{j \in n(i)} d^2(u_i, u_j)} \quad (2.1)$$

$$TV_{aniso}(u) = \sum_{(i, j) \in E} d(u_i, u_j). \quad (2.2)$$

Since forward discretization is used,  $n(i)$  just contains the next grid neighbors in each dimension, i.e. for  $u_i = u((j, k, l))$ , the neighbors are  $n(i) = \{u((j+1, k, l)), u((j, k+1, l)), u((i, k, l+1))\}$ . To also cover inpainting problems, let  $V_k \subset V$  be the index set of pixels where the pixels of the (noisy) original image  $u_0$  are known. The generalized functional is given by

$$J(u) = \frac{1}{2} \sum_{i \in V_k} d^2(u_i, (u_0)_i) + \lambda TV(u). \quad (2.3)$$

#### 2.1.1 The Riemannian distance

The metric  $d$  of course depends on the manifold. Distances on Riemannian manifolds can be measured using smooth curves  $\gamma : [a, b] \rightarrow M$  on the manifold. The length of this curve is

$$L(\gamma) = \int_a^b \sqrt{\langle \dot{\gamma}(t), \dot{\gamma}(t) \rangle_{\gamma(t)}} dt, \quad (2.4)$$

where  $\langle \cdot, \cdot \rangle_x$  denotes the inner product on  $T_x M$ , and the distance can consequently be defined as

$$d : M \times M \rightarrow \mathbb{R}, \quad dist(x, y) = \inf_{\Gamma} L(\gamma), \quad (2.5)$$

where  $\Gamma$  denotes the set of smooth curves connecting  $x, y \in M$ .

This rather general definition is used by Absil et al [4] whereas in this thesis Pennec et al's [8] approach using Riemannian exponential and logarithm map is more convenient. Their definitions are based on *geodesics* because they are precisely the curves that realize the above minimum.

Let  $M$  be a connected, geodesically complete Riemannian manifold. The exponential mapping  $\exp_x : T_x M \rightarrow M$  is defined by  $\exp_x(\nu) := \gamma(1)$  where  $\gamma : \mathbb{R} \rightarrow M$  is the unique geodesic with  $\gamma(0) = x$  and  $\dot{\gamma}(0) = \nu$ . Thus, the function maps the tangent vector  $\nu$  to the point  $y$  on the manifold reached after moving along  $\gamma$  for  $t = 1$ . The logarithm map is its inverse and hence yields the tangent vector  $\nu$  that belongs to the geodesic connecting  $x$  and  $y$ .

A nice overview of Pennec's reinterpretation of vector space operations was given in [23].

Operation	Vector space	Riemannian manifold
Subtraction	$\nu = y - x$	$\nu = \log_x(y)$
Addition	$y = x + v$	$y = \exp_x(\nu)$
Distance	$\text{dist}(x, y) = \ y - x\ $	$\text{dist}(x, y) = \ \log_x(y)\ _x$

Table 2.1: reinterpretation of vector space operations on Riemannian manifolds

## 2.2 Algorithms

The next topic that must be addressed is the minimization of the above defined functional. It brings about another challenge in the form of its non-differentiability. In the implementation, this problem is solved using two different methods. They are based on either working with a regularized version of the functional or by so-called proximal mappings. The latter is used by the proximal point algorithm which will be shortly summarized in the next section before proceeding to the iteratively reweighted least squares (IRLS) algorithm.

### 2.2.1 Proximal point

The proximal point algorithm for manifold-valued data which is implemented in the MTVMT library is based on the work of Weinmann et al [33] and belongs to the class of proximal splitting methods. A survey on these methods for Euclidean space data is provided in [13]. The general scope in the real case are convex optimization problems of the form

$$\underset{x \in \mathbb{R}^n}{\text{minimize}} f_1(x) + \dots + f_m(x) \quad (2.6)$$

where the  $f_i : \mathbb{R}^n \rightarrow ]-\infty, \infty]$  are convex functions but not necessarily differentiable. This is also true for the functional (2.3), even for the simple Euclidean case where the summands are given by  $d(x, y) = |x - y|$ .

Splitting means considering every summand  $f_i$  individually and minimizing it using its proximal mapping

$$\text{prox}_{f_i} x = \underset{y \in \mathbb{R}^n}{\text{argmin}} \left( f_i(y) + \frac{1}{2} \|x - y\|_2^2 \right). \quad (2.7)$$

For the case of a differentiable function  $f$ , the minimization problem (2.7) can be written in an explicit form such that  $\text{prox}_f x = x - \nabla f$ , which can be interpreted as a gradient descent step. In addition to that, one can show that the minimizers of  $f$  are exactly the fixed points of the proximal mapping (See [25], §2.3).

### Application to manifolds

Let  $M$  be a Riemannian manifold and  $\Omega$  as defined in 1.1.2. Due to the square root involved in the isotropic case, the method can only be applied to the anisotropic version of the functional (2.3) and

leads in the 2D case to the following splitting

$$J(u) = \sum_{i,j} F_{ij}(u) + \lambda \sum_{i,j} G_{ij}(u) + \lambda \sum_{i,j} H_{ij}(u) \quad (2.8)$$

$$F_{ij}(u) = d^2(u_{i,j}, (u_0)_{i,j}) \quad (2.9)$$

$$G_{ij}(u) = d(u_{i,j}, u_{i,j+1}) \quad (2.10)$$

$$H_{ij}(u) = d(u_{i,j}, u_{i+1,j}) \quad (2.11)$$

and proximal mappings of the form

$$\text{prox}_{\lambda G_{ij}} x = \operatorname{argmin}_{y \in M^{m \times n}} \left( \lambda G_{ij}(y) + \frac{1}{2} d^2(x, y) \right). \quad (2.12)$$

Only the expressions relevant for the implementation and the algorithm itself are presented in the following. For details on derivations and convergence and existence proofs consider [33].

The proximal mappings itself can be computed using unit speed geodesics. Here  $[x, y]_t$  denotes the point reached by following the unit speed geodesic starting at  $x$  in direction  $y$  for a time  $t$ .

$$(\text{prox}_{\lambda G_{ij}} u)_{ij} = [u_{i,j}, u_{i,j+1}]_{t_{TV}} \quad (2.13)$$

$$(\text{prox}_{\lambda H_{ij}} u)_{ij} = [u_{i,j}, u_{i+1,j}]_{t_{TV}} \quad (2.14)$$

$$(\text{prox}_{\lambda F_{ij}} u)_{ij} = [u_{i,j}, (u_0)_{i,j}]_{t_{l2}} \quad (2.15)$$

Lastly, the times in the case of  $G_{ij}$  and  $F_{ij}$  are computed by

$$t_{TV} = \begin{cases} \mu, & \text{if } \mu < d(u_{i,j}, u_{i,j+1}) \\ \mu < d(u_{i,j}, u_{i,j+1}), & \text{else} \end{cases} \quad (2.16)$$

$$t_{l2} = \frac{\mu}{1+\mu} d(u_{i,j}, (u_0)_{i,j}) \quad (2.17)$$

and for  $H_{ij}$  analogously.

In summary, the parallel version of the proximal algorithm now works by computing a proximal mapping for every pixel  $u_{i,j}$ . The relevant geodesics are in direction of its next neighbors on the grid and in direction of the corresponding pixel of the original picture  $u_0$ , i.e.  $[u_{i,j}, v]_t$  with  $v \in \{u_{i-1,j}, u_{i+1,j}, u_{i,j-1}, u_{i,j+1}, (u_0)_{i,j}\}$ . Next, the intrinsic (Karcher) mean [18] of these five mappings is computed and the pixel is updated to a new value  $u'_{i,j}$ .

Finally, the algorithm is stated in Algorithm 2.1.

### 2.2.2 Iteratively reweighted least squares

The IRLS approach to dealing with non-differentiable terms in the functional is by adding additional terms for regularization. In the continuous (and isotropic) case that means

$$TV_\epsilon = \int_{\Omega} \omega_\epsilon |\nabla u|^2 = \int_{\Omega} \frac{|\nabla u|^2}{\sqrt{|\nabla u|^2 + \epsilon^2}} \quad (2.18)$$

for a small  $\epsilon > 0$ . In this form, the functional becomes differentiable but directly minimizing a regularized functional  $J_\epsilon$  will not work either.

The IRLS algorithm, described in more detail in [26], works by alternating between reweighting and minimization steps. First, the weights are computed then the minimization is performed using the regularized functional with the weights considered constant. The steps for the isotropic functional

---

**Algorithm 2.1** Parallel proximal point algorithm

---

**Require:**  $\mu = (\mu_1, \mu_2, \dots) \in l^2 \setminus l^1$

```

 $u \leftarrow u_0$ 
for  $r \leftarrow 1, 2, \dots$  do
  for  $i \leftarrow 1, 2, \dots, m; j \leftarrow 1, 2, \dots, n;$  do
     $t \leftarrow t_{l^2} = \frac{\mu_r}{1+\mu_r} d(u_{i,j}, (u_0)_{i,j})$ 
     $z^{(1)} \leftarrow [u_{i,j}, (u_0)_{i,j}]_t$ 
     $t \leftarrow t_{TV}(\mu_r \lambda, u_{i,j}, u_{i,j+1})$ 
     $z^{(2)} \leftarrow [u_{i,j}, u_{i,j+1}]_t$ 
     $t \leftarrow t_{TV}(\mu_r \lambda, u_{i,j}, u_{i,j-1})$ 
     $z^{(3)} \leftarrow [u_{i,j}, u_{i,j-1}]_t$ 
     $t \leftarrow t_{TV}(\mu_r \lambda, u_{i,j}, u_{i,j+1})$ 
     $z^{(4)} \leftarrow [u_{i,j}, u_{i,j+1}]_t$ 
     $t \leftarrow t_{TV}(\mu_r \lambda, u_{i,j}, u_{i-1,j})$ 
     $z^{(5)} \leftarrow [u_{i,j}, u_{i-1,j}]_t$ 
     $u'_{i,j} \leftarrow \text{karchermean}(z^{(1)}, z^{(2)}, z^{(3)}, z^{(4)}, z^{(5)})$ 
  end for
  for  $i \leftarrow 1, 2, \dots, m; j \leftarrow 1, 2, \dots, n;$  do
     $u_{i,j} \leftarrow u'_{i,j}$ 
  end for
end for

```

---

are as follows

$$w_i^{new} = W_{iso}^\epsilon(u)_i := \left( \sum_{j \in n(i)} d(u_i, u_j) + \epsilon^2 \right)^{-\frac{1}{2}} \quad \forall i \in V \quad (2.19)$$

$$u^{new} = U(w) := \operatorname{argmin}_{u \in \Omega} \sum_{i \in V_k} d^2(u_i, (u_0)_i) + \lambda \sum_{i \in V} w_i \sum_{j \in n(i)} d^2(u_i, u_j). \quad (2.20)$$

The anisotropic steps are

$$w_{i,j}^{new} = W_{aniso}^\epsilon(u)_{i,j} := (d(u_i, u_j) + \epsilon^2)^{-\frac{1}{2}}, \quad \forall (i, j) \in E \quad (2.21)$$

$$u^{new} = U(w) := \operatorname{argmin}_{u \in \Omega} \sum_{i \in V_k} d^2(u_i, (u_0)_i) + \lambda \sum_{(i,j) \in E} w_{i,j} d^2(u_i, u_j). \quad (2.22)$$

Further details on the derivation and proofs on convergence, existence and uniqueness of solutions for different manifold classes, such as Hadamard spaces or the sphere, can be found in [16]. The minimization can in principle be performed using various methods from smooth optimization theory. Due to its quadratic convergence rate, here the Newton method was chosen. The algorithm is stated in Algorithm 2.2.

## 2.3 Riemannian Newton method

In numerical analysis, the Newton method is one of the standard algorithms for finding approximations of roots of real-valued functions. Due to its locally at least quadratic convergence, the algorithm or one of its numerous variants and generalizations is used in many applications. For its application in optimization, the Newton method is applied to the gradient of the objective function which also requires the evaluation of its Hessian. The following section provides a short summary of the generalization of gradient and Hessian to a manifold setting.

### 2.3.1 Gradient

Let  $M$  be a Riemannian manifold and  $T_x M$  the tangent space at  $x \in M$ . Furthermore, let  $f : M \rightarrow \mathbb{R}$  be a smooth function defined on  $M$ . Define the *Riemannian gradient*  $\operatorname{grad} f$  to be the

---

**Algorithm 2.2** IRLS algorithm

---

```

Choose initial value  $u^{(0)}$  by application of smoothing filter on  $u_0$ 
 $i \leftarrow 0$ 
repeat
   $W \leftarrow W^\epsilon(u^{(i)})$ 
   $u^{(i,0)} \leftarrow u^{(i)}$ 
   $k \leftarrow 0$ 
  repeat
     $u^{(i,k+1)} = \text{newtonstep}^{\lambda, u_0, V_k, V, E}(W, u^{(i,k)})$ 
     $k \leftarrow k + 1$ 
  until Stopping criteria (e.g.  $k = 1, J(u^{(i,k+1)}) < J(u^{(i,0)})$ ,  $d(u^{(i,k+1)}, u^{(i,k)})$ )
   $u^{(i+1)} \leftarrow u^{(i,k+1)}$ 
   $i \leftarrow i + 1$ 
until  $d(u^{(i+1)}, u^{(i)}) < tol$ 
return  $u^{(i+1)}$ 

```

---

unique tangent vector  $\xi \in T_x M$  satisfying

$$\langle \text{grad } f(x), \xi \rangle_x = Df(x)[\xi] \quad (2.23)$$

where  $Df(x)[\xi] = \xi[f]$ , when  $\xi : \mathcal{C}^\infty(M) \rightarrow \mathbb{R}$  is interpreted as derivation acting on  $f$ . The Riemannian gradient shares many properties of its Euclidean counterpart, in particular defining the direction of steepest ascent, such that first order methods like gradient descent could already be implemented at this point.

### 2.3.2 Hessian

For second order methods, such as the Newton algorithm, also a corresponding *Riemannian Hessian* is needed. Following again the work of Absil et al [4], the Hessian is realized as linear endomorphism of the tangent space  $T_x M$

$$\text{Hess } f(x)[\xi] = \nabla_\xi \text{grad } f(x), \quad (2.24)$$

where  $\nabla$  denotes the Riemannian connection on  $M$ .

### 2.3.3 Newton equation

Now let  $x \in M$  and  $\gamma : [a, b] \rightarrow M$  be the unique geodesic with  $\gamma(0) = x$  and  $\dot{\gamma}(0) = \nu \in T_x M$  passing through  $y \in M$ . Thus, one can set  $y = \exp_x(\nu)$  and  $\nu = \log_x(y)$  as suggested in 2.1.1. Using the definitions of gradient and Hessian above one can expand  $f$  to second order around  $x$  in the following way

$$\begin{aligned} f(\exp_x(\nu)) &= f_x(\nu) = f(x) + \langle \text{grad } f(x), \nu \rangle_x + \frac{1}{2} \langle \text{Hess } f(x)[\nu], \nu \rangle_x + \mathcal{O}(\|\nu\|_x^3) \quad \Leftrightarrow \quad (2.25) \\ f(y) &= f(x) + \langle \text{grad } f(x), \log_x(y) \rangle_x + \frac{1}{2} \langle \text{Hess } f(x)[\log_x(y)], \log_x(y) \rangle_x + \mathcal{O}(\|\log_x(y)\|_x^3). \end{aligned}$$

The first line of (2.25) suggests that, for given fixed  $x$ ,  $f$  can also be interpreted as a function of  $\nu \in T_x M$  and the optimization of  $f$  can be performed on the tangent space, on which  $\text{grad } f$  and  $\text{Hess } f$  have been defined. This finally leads to the following generalization of the *Newton equation* for the correction term  $\eta_x \in T_x M$ :

$$\text{Hess } f(x)[\eta_x] = -\text{grad } f(x) \quad (2.26)$$

The solution of the Newton equation  $\eta_x$  is a tangent vector of  $T_x M$  and, as (2.25) already implies, can be mapped back to the manifold  $M$  using the exponential map such that  $y' = \exp_x(\eta_x)$ . The whole iterative procedure, based on [4], Algorithm 5, is summarized in the following listing.

---

**Algorithm 2.3** Riemannian Newton method for real-valued functions

---

```

 $x_0 \leftarrow x \in M$  (initial value)
for  $k \leftarrow 0, 1, 2, \dots$  do
    Solve newton equation  $\text{Hess } f(x_k)\eta_k = -\text{grad } f(x_k)$  for  $\eta_k \in T_{x_k} M$ 
     $x_{k+1} \leftarrow \exp_{x_k}(\eta_k)$ 
end for

```

---

### 2.3.4 Newton equation for the TV functional

Next, the general form of the linear system defined by (2.26) in the case of manifold-valued 3D images  $u, u_0 : \Omega \rightarrow M^{Z \times Y \times X}$  where  $\Omega = \{1, \dots, Z\} \times \{1, \dots, Y\} \times \{1, \dots, X\}$  for  $X, Y, Z \in \mathbb{N}$  and a corresponding functional  $J : M^{Z \times Y \times X} \rightarrow \mathbb{R}$  is shown. Furthermore, the forward finite difference scheme described in 1.1.2 is used. To simplify notation, assume the regularization weights obtained from the last IRLS reweighting step to be all equal to 1 and thus consider only the bare  $d^2(\cdot, \cdot)$  terms:

$$J(u_{111}, u_{112}, \dots, u_{ijk}, \dots, u_{ZYX}) = \sum_{ijk} d^2(u_{ijk}, (u_0)_{ijk}) \quad (2.27)$$

$$+ \lambda \sum_{ijk}^{Z-1, Y, X} d^2(u_{ijk}, u_{i+1, j, k}) + \lambda \sum_{ijk}^{Z, Y-1, X} d^2(u_{ijk}, u_{i, j+1, k}) + \lambda \sum_{ijk}^{Z, Y, X-1} d^2(u_{ijk}, u_{i, j, k+1}).$$

The first derivatives are given by the following expressions

$$\begin{aligned} \frac{\partial J}{\partial u_{mnp}} &= d_x^2(u_{mnp}, (u_0)_{mnp}) + \lambda(d_x^2(u_{mnp}, u_{m+1, n, p}) + d_y^2(u_{m-1, n, p}, u_{mnp}) \\ &\quad + d_x^2(u_{mnp}, u_{m, n+1, p}) + d_y^2(u_{m, n-1, p}, u_{mnp}) \\ &\quad + d_x^2(u_{mnp}, u_{m, n, p+1}) + d_y^2(u_{m, n, p-1}, u_{mnp})), \end{aligned} \quad (2.28)$$

where  $d_x^2((u, v)) := \frac{\partial}{\partial x} d^2(x, y) \Big|_{(x, y)=(u, v)}$ .

The second derivatives, considering only the terms in the first line of (2.28) containing the fidelity term and discrete gradient components in  $z$  direction, are then

$$\frac{\partial^2 J}{\partial u_{ijk} \partial u_{mnp}} = \delta_{nj} \delta_{kp} \delta_{mi} d_{xx}^2(u_{ijk}, (u_0)_{ijk}) \quad (2.29)$$

$$+ \lambda \delta_{nj} \delta_{kp} \left[ \delta_{mi} \left( d_{xx}^2(u_{ijk}, u_{i+1, j, k}) + d_{yy}^2(u_{ijk}, u_{i+1, j, k}) \right) \right] \quad (2.30)$$

$$+ \delta_{m-1, i} d_{xy}^2(u_{ijk}, u_{i+1, j, k}) + \delta_{m+1, i} d_{yy}^2(u_{i-1, j, k}, u_{ijk}) \Big]. \quad (2.31)$$

Considering the pattern of the Kronecker deltas and reshaping the tensor of second partial derivatives into a single matrix, one obtains a block-band matrix, where sums of non-mixed second derivatives of the squared distance function are located on the main diagonal, while all mixed derivatives belonging to the same gradient component ( $x, y$  or  $z$ ) populate subdiagonals of equal distance to the main diagonal. In particular, discretizations in  $x$ -direction are on the first, in  $y$ -direction on the  $X$ th and in  $z$ -direction on the  $X \times Y$ th subdiagonals.

To illustrate this, consider the following schematic of the band structure

$$HJ = \begin{pmatrix} D & X & Y & Z & & \\ X & D & X & Y & Z & \\ & X & D & X & Y & \\ Y & X & D & X & Y & \\ & Y & X & D & X & \\ Z & Y & X & D & X & \\ & Z & Y & X & D & \end{pmatrix}, \quad (2.32)$$

where  $D$  denotes a block, consisting of the sum of non-mixed second derivatives, according to the rules defined by the generalization of (2.29) to all discretization directions.

$HJ$  is exactly the matrix representation of the Hessian operator  $\text{Hess } J(u)$ , while the representation  $GJ$  of  $\text{grad } J(u)$  is just the vectorized version of the tensor of first derivatives (2.28). If the embedding space of the manifold is given by  $\mathbb{R}^{n \times p}$  then the matrix  $HJ$  will be an element of  $\mathbb{R}^{\tilde{D} \times \tilde{D}}$  with  $\tilde{D} = npXYZ$ .  $HJ$  is, however, also sparse with approximately  $7\tilde{D}$  non-zero entries. Finally, solving the Newton equation (2.26) corresponds to solving the sparse linear system given by  $HJ$  and  $GJ$ , which is also the most computationally demanding part of the algorithm.

### 2.3.5 Tangent space restriction

Lastly, a basis of the tangent space  $T_x M$  for each  $x \in M$  can be chosen such that the computed gradient and Hessian are restricted to the tangent space by performing a basis transformation. Since  $\dim T_x M = \dim M$ , this means that tangent vectors, such as the gradients of the squared distance function, or tangent space mappings, like the Hessian, can be expressed using only  $\dim M$  coefficients. Now  $D = \dim M(XYZ)$  such that the prefactor is the intrinsic manifold dimension and not the dimension of the embedding space any more.

## 2.4 Manifolds

In this section all relevant quantities to implement the IRLS and proximal point algorithm are presented. These are the distance function and its derivatives, exponential and logarithm mapping and the tangent space basis transformation mapping. For the Grassmann manifold, due to its quotient manifold nature and because it was not covered in the original implementation based on [16] a more general introduction will be given.

### 2.4.1 Euclidean space

The space in question is just  $\mathbb{R}^n$ , hence trivially a manifold and naturally a vector space such that all expressions can be calculated using basic multivariable calculus. The exponential and logarithm mappings are not to be understood in the sense of  $e^x$  but according to 2.1.1 such that they are just addition and subtraction in the vector space.

#### Exponential map

$$\exp_x(r) = x + r \quad (2.33)$$

#### Logarithm map

$$\log_x(y) = y - x \quad (2.34)$$

#### Squared distance function

$$d(x, y) = \|x - y\|^2 = \sum_{i=1}^n (x_i - y_i)^2 \quad (2.35)$$

#### First derivative of the squared distance function

$$\frac{\partial d^2(x, y)}{\partial y} = 2x \quad (2.36)$$

#### Second derivatives of the squared distance function

$$\frac{\partial^2 d^2(x, y)}{\partial x \partial y} = \frac{\partial^2 d^2(x, y)}{\partial x^2} = 2\mathbb{1}_n; \quad (2.37)$$

where here and in all following expression  $\mathbb{1}_n$  denotes the identity matrix.

### Tangent space restriction map

$$T_x = \mathbb{1}_{n^2} \quad (2.38)$$

#### 2.4.2 Sphere $S^n$

Consider the manifold  $S^n := \{x \in \mathbb{R}^{n+1} : \|x\| = 1\} \subset \mathbb{R}^{n+1}$  and express the maps in terms of vectors  $x, y \in \mathbb{R}^{n+1}$  of the Euclidean embedding space.

The tangent space  $T_x S^n$  at  $x \in \mathbb{R}$  is, as basic intuition suggests, given by the tangent hyperplane to the sphere at  $x$  such that

$$T_x S^n := \{y \in \mathbb{R}^{n+1} : x^T y = 0\} \quad (2.39)$$

The standard Euclidean inner product  $\langle r, s \rangle = r^T s$ , restricted to the tangent space, turns  $S^n$  into a Riemannian manifold.

#### Exponential map

$$\exp_x(r) = \cos(\|r\|_2)x + \frac{\sin(\|r\|_2)}{\|r\|_2}r \quad (2.40)$$

#### Logarithm map

$$\log_x(y) = \arccos(x^T y) \frac{y - x^T y x}{\|y - x^T y x\|_2} \quad (2.41)$$

Note that this is only well-defined for non-antipodal points  $x, y \in S^n$ .

#### Squared distance function

$$d(x, y) = \arccos(x^T y) \quad (2.42)$$

#### First derivative of the squared distance function

$$\frac{\partial d^2(x, y)}{\partial x} = \begin{cases} \frac{-2 \arccos(x^T y)}{\sqrt{1-(x^T y)^2}} y, & x^T y \in (-1, 1) \\ -2y, & x^T y = 1 \end{cases} \quad (2.43)$$

#### Second derivatives of the squared distance function

$$\frac{\partial^2 d^2(x, y)}{\partial x^2} = \begin{cases} \left[ \frac{2}{1-(x^T y)^2} - \frac{2 \arccos(x^T y)}{(1-(x^T y)^2)^{\frac{3}{2}}} x^T y \right] yy^T + 2x^T y \mathbb{1}_{n+1}, & x^T y \in (-1, 1) \\ \frac{2}{3} yy^T + 2x^T y \mathbb{1}_{n+1}, & x^T y = 1 \end{cases} \quad (2.44)$$

And the mixed derivative:

$$\frac{\partial^2 d^2(x, y)}{\partial x \partial y} = \begin{cases} \left[ \frac{2}{1-(x^T y)^2} - \frac{2 \arccos(x^T y)}{(1-(x^T y)^2)^{\frac{3}{2}}} x^T y \right] yx^T - \frac{-2 \arccos(x^T y)}{\sqrt{1-(x^T y)^2}} y \mathbb{1}_{n+1}, & x^T y \in (-1, 1) \\ \frac{2}{3} yx^T - 2 \mathbb{1}_{n+1}, & x^T y = 1 \end{cases} \quad (2.45)$$

#### Tangent space restriction map

As implied by (2.39), the tangent space  $T_x S^n$  at  $x \in S^n$  is just the orthogonal complement of  $x$  in  $\mathbb{R}^{n+1}$ . Thus, constructing a basis of the tangent space amounts to constructing an orthonormal basis  $\{b_0, b_1, \dots, b_n\}$  of  $\mathbb{R}^{n+1}$  with  $b_0 = x$ . Then  $\mathcal{B} = \{b_i\}_{i=1}^n$  is the basis of the tangent space. This can be done using the QR algorithm or, in the case of  $S^2 \subset \mathbb{R}^3$ , using the cross product. For the basis transformation mapping this means that

$$T_x : \mathbb{R}^{n+1} \rightarrow \mathbb{R}^n \quad (2.46)$$

$$T_x = (b_1 | b_2 | \dots | b_n). \quad (2.47)$$

### 2.4.3 Special orthogonal group $\text{SO}(n)$

The special orthogonal group, considered as matrix group is defined as follows

$$\text{SO}(n) := \{X \in \mathbb{R}^{n \times n} : X^T X = \mathbb{1}_n, \det(X) = 1\}, \quad (2.48)$$

while its tangent space at  $X \in \text{SO}(n)$  is

$$T_X \text{SO}(n) := \{XS : S^T = -S\} = X[\text{Skew}(n)]. \quad (2.49)$$

Here, the notation  $X[\text{Skew}(n)]$  means the set of all matrices that can be written as a product of  $X$  and a skew-symmetric matrix.

Equipping  $T_X \text{SO}(n)$  with the standard inner product  $\langle R, S \rangle_X = \text{tr } R^T S$  of its embedding space turns  $(\text{SO}(n), \langle \cdot, \cdot \rangle)$  into a Riemannian manifold.

#### Exponential map

$$\exp_X R = X \exp(X^T R) \quad (2.50)$$

Note that the exponential map on the right hand side denotes the matrix exponential. The same holds for the logarithm on the right hand side of the following expression.

#### Logarithm map

$$\log_X(Y) = X \log(X^T Y) \quad (2.51)$$

#### First derivatives of the distance function

For the computation of the derivatives of the squared distance function, there exists a general analytic result by Karcher[18] that simplifies further computations considerably:

**Theorem 2.1** (Karcher). *Let  $M$  be a complete Riemannian manifold and  $x, y \in M$  such that the geodesic connecting  $x$  and  $y$  is unique. Then the squared distance function to  $y$  is differentiable at  $x$  and we have*

$$\frac{\partial d^2(x, y)}{\partial x}[\cdot] = -2 \langle \log_x(y), \cdot \rangle_x \quad (2.52)$$

where  $\langle \cdot, \cdot \rangle$  is the Riemannian metric at  $x \in M$ .

Since with (2.51), there is a closed form expression for  $\log_x(y)$ , the first derivative can be expressed as

$$\frac{\partial d^2(X, Y)}{\partial X} = -2X \log(X^T Y). \quad (2.53)$$

#### Second derivatives of the distance function

For the computation of the second derivatives one can take the expression obtained using the above theorem as a starting point and follow the approach and notation of Magnus [22]. This makes it possible to express the derivatives as combinations of simple Kronecker products of the arguments, which is also very straightforward and compact to implement. The detailed derivations can be found in the Appendix B while here only the final results are shown.

For the second derivative with respect to the first argument one readily arrives at

$$\frac{\partial^2 d^2(X, Y)}{\partial X^2} = -2 \left[ \left( (\log X^T Y)^T \otimes \mathbb{1}_n \right) + (\mathbb{1}_n \otimes X) D \log(X^T Y) (Y^T \otimes \mathbb{1}_n) K_{nn} \right], \quad (2.54)$$

where  $K_{nn}$  denotes the commutator matrix which transforms the column-wise vectorization of a matrix  $A$  to the vectorization of its transpose  $A^T$ .

The mixed derivative is given by

$$\frac{\partial^2 d^2(X, Y)}{\partial X \partial Y} = -2 (\mathbb{1}_n \otimes X) D \log(X^T Y) (\mathbb{1}_n \otimes X^T). \quad (2.55)$$

These expressions are quasi-analytic: Matrix logarithm and the Fréchet derivative of the matrix logarithm need to be evaluated numerically. Details concerning the implementation of the latter are postponed to Section 2.5.

### Tangent space restriction map

The dimension of the tangent space  $T_X SO(n)$  at  $X \in SO(n)$  is  $d = \frac{n(n-1)}{2}$ . Define a basis for the space of skew-symmetric matrices  $\text{Skew}(n)$  in the following way. Let  $K = \{(i, j) \in \mathbb{N}^2 : 1 \leq i < d, i < j \leq d\}$  and note that  $|K| = d$ . For all  $k = (k_1, k_2) \in K$  define the basis vector  $B^{(k)}$  by

$$B_{ij}^{(k)} = \begin{cases} \frac{1}{\sqrt{2}}, & i = k_1 \text{ and } j = k_2 \\ -\frac{1}{\sqrt{2}}, & i = k_2 \text{ and } j = k_1 \\ 0, & \text{else} \end{cases} \quad (2.56)$$

The basis of the tangent space is then  $\mathcal{B}_{T_X SO(n)} = \{T^{(k)} = XB^{(k)}\}_{k \in K}$  and to obtain the basis transformation map vectorize each basis matrix and define a matrix  $T_X \in \mathbb{R}^{n^2 \times d}$  whose columns are given by the vectorized basis matrices.

$$T_X : \mathbb{R}^{n^2} \rightarrow \mathbb{R}^d \quad (2.57)$$

$$T_X = (\vec{T}^{(1)} | \vec{T}^{(2)} | \cdots | \vec{T}^{(d)}) \quad (2.58)$$

### 2.4.4 Symmetric positive definite matrices $SPD(n)$

The cone of symmetric, positive definite matrices is defined as

$$SPD(n) := \{X \in \mathbb{R}^{n \times n} : X^T = X, y^T X y > 0 \forall y \in \mathbb{R}^n \setminus \{0\}\}. \quad (2.59)$$

For  $X \in SPD(n)$  the tangent space at  $X$  is isomorphic to the set of symmetric matrices

$$T_X SPD(n) := X[\text{Sym}(n)]. \quad (2.60)$$

The Riemannian metric defined on  $T_X SPD(n)$  is given by

$$\langle R, S \rangle_X := \text{tr}(X^{-1}RX^{-1}S). \quad (2.61)$$

#### Exponential map

$$\exp_X(R) = X^{\frac{1}{2}} \exp\left(X^{-\frac{1}{2}}RX^{-\frac{1}{2}}\right) X^{\frac{1}{2}} \quad (2.62)$$

#### Logarithm map

$$\log_X(Y) = X^{\frac{1}{2}} \log\left(X^{-\frac{1}{2}}YX^{-\frac{1}{2}}\right) X^{\frac{1}{2}} \quad (2.63)$$

#### Squared distance function

As in the case of the special orthogonal group, the Riemannian metric (2.61) induces the distance function on  $SPD(n)$  such that

$$d^2(X, Y) = \|\log\left(X^{-\frac{1}{2}}YX^{-\frac{1}{2}}\right)\|_F^2 \quad (2.64)$$

where  $\|\cdot\|_F$  denotes the Frobenius norm on  $\mathbb{R}^{n \times n}$ .

#### First derivatives of the squared distance function

For the first derivatives one can apply theorem 2.1 again but some care must be taken in the computation this time since the Riemannian metric on  $SPD(n)$  depends also on the base point  $X$

of its tangent space  $T_X SPD(n)$ .

$$\frac{\partial d^2(X, Y)}{\partial X} = -2 \langle \log_X(Y), \cdot \rangle_X \quad (2.65)$$

$$= -2 \left\langle X^{\frac{1}{2}} \log \left( X^{-\frac{1}{2}} Y X^{-\frac{1}{2}} \right) X^{\frac{1}{2}}, \cdot \right\rangle_X \quad (2.66)$$

$$= -2 \left\langle X^{-1} X^{\frac{1}{2}} \log \left( X^{-\frac{1}{2}} Y X^{-\frac{1}{2}} \right) X^{\frac{1}{2}} X^{-1}, \cdot \right\rangle_{\mathbb{1}_n} \quad (2.67)$$

$$= -2 \left\langle X^{-\frac{1}{2}} \log \left( X^{-\frac{1}{2}} Y X^{-\frac{1}{2}} \right) X^{-\frac{1}{2}}, \cdot \right\rangle_{\mathbb{1}_n} \quad (2.68)$$

### Second derivatives of the distance function

For the SPD matrices one can proceed in the same way as for the orthogonal group and obtain

$$\begin{aligned} \frac{\partial^2 d^2(X, Y)}{\partial X^2} &= 2 \left[ \left( X^{-\frac{1}{2}} \log \left( X^{-\frac{1}{2}} Y X^{-\frac{1}{2}} \right)^T \otimes \mathbb{1}_n \right) + \left( \mathbb{1}_n \otimes X^{-\frac{1}{2}} \log \left( X^{-\frac{1}{2}} Y X^{-\frac{1}{2}} \right) \right) \right. \\ &\quad \left. + \left( X^{-\frac{1}{2}} \otimes X^{-\frac{1}{2}} \right) D \log \left( X^{-\frac{1}{2}} Y X^{-\frac{1}{2}} \right) \left( \left( X^{-\frac{1}{2}} Y \otimes \mathbb{1}_n \right) + \left( \mathbb{1}_n \otimes X^{-\frac{1}{2}} Y \right) \right) \right] \times \dots \\ &\quad \dots \times \left( X^{-\frac{1}{2}} \otimes X^{-\frac{1}{2}} \right) D \left( X^{\frac{1}{2}} \right) \end{aligned} \quad (2.69)$$

for the non-mixed derivatives and

$$\frac{\partial^2 d^2(X, Y)}{\partial X \partial Y} = -2 \left( X^{-\frac{1}{2}} \otimes X^{-\frac{1}{2}} \right) D \log \left( X^{-\frac{1}{2}} Y X^{-\frac{1}{2}} \right) \left( X^{-\frac{1}{2}} \otimes X^{-\frac{1}{2}} \right) \quad (2.70)$$

for the mixed ones.

### Tangent space restriction map

For  $SPD(n)$  it holds that  $d := \dim = \frac{n(n+1)}{2}$ . In analogy to the previous manifold, define a basis for the space of symmetric matrices  $\text{Sym}(n)$ . In this case,  $K = K_1 \cup K_2 = \{(i, i) \in \mathbb{N}^2 : 1 \leq i \leq n\} \cup \{(i, j) \in \mathbb{N}^2 : 1 \leq i < j, i < j \leq d\}$  such that again  $|K| = d$ . For all  $k \in K$  define the basis vector  $B^{(k)}$  by

$$B_{ij}^{(k)} = \begin{cases} 1, & i = k_1 \text{ and } j = k_2 \\ 1, & i = k_2 \text{ and } j = k_1 \\ 0, & \text{else} \end{cases} \quad (2.71)$$

For  $k \in K_1$ , these are single-entry diagonal matrices. The basis of the tangent space is then  $\mathcal{B}_{T_X SPD(n)} = \{T^{(k)} = X^{\frac{1}{2}} B^{(k)} X^{\frac{1}{2}}\}_{k \in K}$  and the restriction map is defined completely analogous to the  $SO(n)$  case.

### 2.4.5 Grassmannian $Gr(n, p)$

The Grassmann manifold is special among the manifolds so far considered due to the fact that it is a quotient manifold. As such, there are different possibilities for choosing equivalence classes and representatives thereof.

For positive integers  $n$  and  $p \leq n$  the Grassmann manifold is defined as the set of  $p$ -dimensional linear subspaces of  $\mathbb{R}^n$ . Since a linear subspace  $\mathcal{Y} \in Gr(n, p)$  can be specified using a basis, one can arrange its basis vectors as columns of a matrix  $Y \in \mathbb{R}^{n \times p}$  such that its column space spans  $\mathcal{Y}$ . The rank of  $Y$  must necessarily be full and equal to  $p$  because of the linear independence of its columns. Hence, elements of  $Gr(n, p)$  can be represented using elements of the *non-compact Stiefel manifold*

$$\tilde{St}(n, p) := \{Y \in \mathbb{R}^{n \times p} : \text{rank } Y = p\}. \quad (2.72)$$

## Quotient representations

Observing now that post-multiplication by any invertible  $G \in Gl(p)$  does not change the span of  $Y$ , one can form the equivalence classes

$$Y GL(p) := \{YG : G \in Gl(p)\} \quad (2.73)$$

consisting of all matrices having the same span as  $Y$ . These equivalence classes can be thought of as the distinct elements of the Grassmannian which leads to the following quotient manifold representation.

$$\tilde{Gr}(n, p) := \tilde{St}(n, p)/Gl(p) \quad (2.74)$$

This representation, used by Absil et al [3], is very general because only the rank is specified.

The next steps of presenting the relevant quantities for the algorithm will follow Absil's derivation and notation but uses the quotient representation used by Edelman et al [14], which is based on the orthogonal group. This will simplify most expressions and is also desirable from an algorithmic point of view as it removes more degrees of freedom in the choice of possibly unique representatives.

For the sake of completeness, there is also a completely different approach by Sato and Iwai [28] who choose  $\mathbb{R}^{n \times n}$  as embedding space where elements of  $Gr(n, p)$  are given by rank  $p$  orthogonal projection matrices. The presented applications are, however, mostly eigenvalue problems while in the case of image denoising the increased memory requirements are disadvantageous.

Denote by

$$St(n, p) = \{Y \in \mathbb{R}^{n \times p} : Y^T Y = \mathbb{1}_p\} \quad (2.75)$$

the *compact* Stiefel manifold.

The orthogonal group quotient representation of the Grassmann manifold, which is of course isomorphic to the previous representation, is given by

$$Gr(n, p) = St(n, p)/O(p) \quad (2.76)$$

The additional requirement is now that the basis spanning the subspace  $\mathcal{Y}$  must be orthonormal.

Finally, the canonical projection map to the quotient is given by

$$\pi : St(n, p) \ni Y \mapsto \text{span } Y = \mathcal{Y} \in Gr(n, p). \quad (2.77)$$

## Locally unique representatives

From an algorithmic point of view it is desirable to work with representatives as unique as possible for two reasons. Firstly, it provides the means to give well-defined expressions for the computation of various quantities using arbitrary representatives and secondly, it makes it possible to find a parametrization of  $Gr(n, p)$  in terms of  $\mathbb{R}^{(n-p) \times p}$  matrices. This is necessary to construct a local basis of the tangent base and make the dimension of the sparse linear system a function of the intrinsic manifold dimension  $(n - p)p$  instead of the embedding dimension  $np$ .

It is indeed possible to obtain a set of locally unique representatives by picking some other element  $U \in St(n, p)$  and choose as representatives those elements who lie in the intersection of their equivalence classes and an affine cross section orthogonal to the equivalence class of  $U$ : Let  $U \in St(n, p)$  and  $\mathcal{U} := \text{span}(U) \in Gr(n, p)$  and define the local affine cross section through  $U$  and orthogonal to the fiber  $U[O(p)] = \pi^{-1}(\mathcal{U}) \subset St(n, p)$  by

$$S_U := \{V \in St(n, p) : U^T(V - U) = 0\} \subset St(n, p). \quad (2.78)$$

The equivalence class of  $V \in St(n, p)$  is equal to  $\pi^{-1}(\pi(V)) = V[O(p)]$  and to calculate its intersection with  $S_U$  choose  $R \in O(p)$  such that  $VR \in V[O(p)]$  and obtain

$$VR \in S_U \Leftrightarrow U^T(VR - U) = 0 \Leftrightarrow R = (U^T V)^{-1} \quad (2.79)$$

which leads to the intersection

$$S_U \cap V[O(p)] = \{VR = V(U^T V)^{-1}\}. \quad (2.80)$$

The intersection is empty if  $U^T V$  is not invertible. Finally, define a *cross-section mapping*  $\sigma_U$  restricted to the set

$$\mathcal{U}_U := \{\mathcal{V} = \text{span } V : U^T V \in GL(p)\} \quad (2.81)$$

by

$$\sigma_U : Gr(n, p) \supset \mathcal{U}_U \ni \mathcal{V} = \text{span } V \mapsto V(U^T V)^{-1} \in S_U \subset St(n, p) \subset \mathbb{R}^{n \times p}. \quad (2.82)$$

$\sigma_U$  is also a diffeomorphism providing the differentiable structure. The cross section map is illustrated in Figure 2.1.

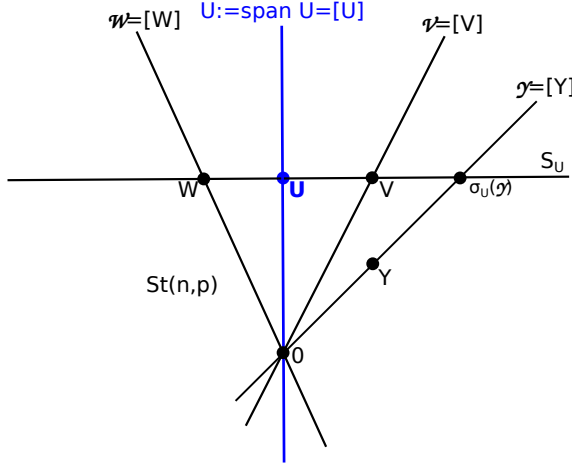


Figure 2.1: The cross section mapping is illustrated for the special case of  $St(2, 1) \subset \mathbb{R}^2$ . Equivalence classes are all lines passing through the origin. Pick a  $U \in St(2, 1)$ , then the cross section is given by all  $V \in St(2, 1)$  for which  $U - V$  is orthogonal to  $U$ . This is true for the points  $V$  and  $W$ , representing  $\mathcal{V}$  and  $\mathcal{W}$ , respectively, but not for the representative  $Y$  of  $\mathcal{Y}$ . The cross section mapping can be used to obtain a representative  $\sigma_U(Y)$  of  $\mathcal{Y}$  which lies again on the cross section. Hence, the cross section is a tool for obtaining a set of locally unique representatives.

As an example for the application of the cross section map, consider the calculation of averages on the Grassmann manifold.

**Example 2.1** (Average). *For the case of an average, take representatives  $Y_1, \dots, Y_n \in St(n, p)$  for  $\mathcal{Y}_1, \dots, \mathcal{Y}_n \in Gr(n, p)$  and find a  $U \in St(n, p)$  such that  $S_U$  has non-zero intersection with all the  $Y_i$ 's equivalence classes, which is equivalent to  $U^T Y_i \in Gl(p)$ . The average  $\mathcal{A}$  can then be written as*

$$\mathcal{A} := \pi \left( \sum_{i=1}^n \sigma_U(Y_i) \right) = \pi \left( \sum_{i=1}^n Y_i (U^T Y_i)^{-1} \right). \quad (2.83)$$

### Tangent space

The quotient structure makes it necessary to work with representatives such that the usual method for finding the tangent space by differentiating curves on the manifold cannot be applied. Instead one has to start with the "numerator" of the quotient  $St(n, p)$ . For the Grassmann manifold only tangent vectors of a special subspace of  $T_Y St(n, p)$ , the horizontal space, can modify the span of a

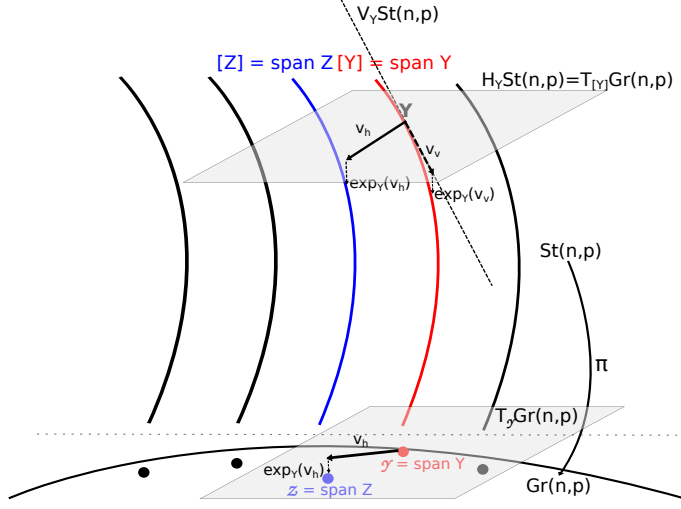


Figure 2.2: The tangent space  $T_Y St(n,p)$  at  $Y$  can be decomposed into two parts: The vertical space  $V_Y St(n,p)$ , defined as the tangent space to the equivalence class (fiber)  $[y] = \pi^{-1}(\pi(Y))$ , and the horizontal space  $H_Y St(n,p)$  as its orthogonal complement. Only tangent vectors of the horizontal space modify the span, in the sense that their retraction (in this case using the exponential map) lies in a different equivalence class. Those are the tangent vectors of  $T_Y Gr(n,p)$ .

subspace and exactly those belong to the tangent space of  $Gr(n,p)$ . The notion of modifying and non-modifying tangent vectors can be best understood with the help of Figure 2.2.

Let  $Y \in St(n,p) \subset \mathbb{R}^{n \times p}$ . Then the tangent space at  $Y$  ([4] for details of the derivation) to the compact Stiefel manifold is given by

$$\begin{aligned} T_Y St(n,p) &= \{Z \in \mathbb{R}^{n \times p} : Y^T Z + Z^T Y = 0\} \\ &= \{Y\Omega + Y_\perp K : \Omega \in \text{Skew}(p), K \in \mathbb{R}^{(n-p) \times p}\} \end{aligned} \quad (2.84)$$

where  $Y_\perp \in \mathbb{R}^{n \times (n-p)}$  is chosen such that  $[Y, Y_\perp] \in O(n)$ . The second representation of (2.84) already implies the decomposition into vertical and horizontal spaces performed in the next steps.

The vertical space at  $Y$  is by definition the tangent space to the fiber  $\pi^{-1}(\pi(Y))$

$$V_Y = T_Y \pi^{-1}(\pi(Y)) = T_Y Y[O(p)] = Y[\text{Skew}(p)], \quad (2.85)$$

while the horizontal space is defined as its orthogonal complement with respect to (2.84)

$$H_Y = V_Y^\perp = \{H \in T_Y St(n,p) : Y^T H = 0\} \simeq Y_\perp [\mathbb{R}^{(n-p) \times p}]. \quad (2.86)$$

Using this, the tangent space to  $Gr(n,p)$  at  $\pi(Y) = \mathcal{Y}$ , along with its projector, is given by

$$T_{\mathcal{Y}} Gr(n,p) \simeq H_Y St(n,p) \simeq Y_\perp [\mathbb{R}^{(n-p) \times p}] \quad (2.87)$$

$$\pi_{Y_\perp} := \mathbb{1}_n - YY^T. \quad (2.88)$$

The problem that remains is to pick a unique representative for a tangent vector  $\xi \in T_{\mathcal{Y}} Gr(n,p)$ . This is resolved by demanding that the unique representative  $\xi_{\diamond Y}$  should project to  $\xi$  via

$$d\pi(Y)\xi_{\diamond Y} = \xi \quad (2.89)$$

where  $\pi : St(n,p) \rightarrow Gr(n,p)$  is the canonical quotient projection, such that  $d\pi$  is a map between their tangent spaces. Using the cross section mapping (2.82),  $\xi_{\diamond Y}$  can be computed by

$$\xi_{\diamond Y} = d\sigma_Y(\mathcal{Y})\xi. \quad (2.90)$$

$\xi_{\diamond Y}$  is called the *horizontal lift* of  $\xi \in T_Y Gr(n, p)$  at  $Y \in St(n, p)$ .

Finally, to obtain a basis for the tangent space, choose  $\{E_{ij}\}_{i=1, j=1}^{n-p, p}$ , with the (i,j)th entry set to one and the rest zero, as a basis of  $\mathbb{R}^{(n-p) \times p}$  and compute  $Y_\perp$  using a QR decomposition of  $Y$ . The orthogonal complement  $Y_\perp$  is then just given by  $Q_2 \in \mathbb{R}^{n \times (n-p)}$  which is part of the decomposition of the orthogonal matrix  $Q = [Q_1, Q_2] \in \mathbb{R}^{n \times n}$ .

For the basis of the tangent space one obtains

$$\{B_{ij}\} = \{Y_\perp E_{ij}\}. \quad (2.91)$$

The Riemannian metric for the Grassmann manifold, defined on the tangent space  $T_X Gr(n, p)$ , is given by

$$\langle R, S \rangle_{\mathcal{X}} = \text{Tr} R^T S, \quad (2.92)$$

which is just the inner product of its embedding space restricted to the manifold.

### Exponential map

Let  $X, R$  span  $\mathcal{X}, \mathcal{R}$ , respectively and let  $U\Sigma V^T$  denote the thin singular value decomposition of  $R$  with  $U \in \mathbb{R}^{n \times p}$ ,  $\Sigma \in \mathbb{R}^{p \times p}$  and  $V \in \mathbb{R}^{p \times p}$ . Then

$$\exp_{\mathcal{X}}(\mathcal{R}) = \text{span}(XV \cos \Sigma V^T + U \sin \Sigma V^T). \quad (2.93)$$

### Logarithm map

Let  $X, Y$  span  $\mathcal{X}, \mathcal{Y}$ , respectively and let  $U\Sigma V^T$  denote the thin singular value decomposition of  $Z = \pi_{X_\perp} \sigma_X(Y) = (\mathbb{1}_n - XX^T)Y(X^TY)^{-1}$ . This can be interpreted as choosing a locally unique representative of  $Y$  with respect to the affine cross section defined by  $X$  and subsequently projecting it back to the tangent space  $T_X Gr(n, p)$  at  $\mathcal{X}$ . The map is given by

$$\log_X(Y) = U \arctan \Sigma V^T. \quad (2.94)$$

### Distance function

Using the exponential map, one can easily define a geodesic distance function on the Grassmann manifold which is induced by its Riemannian metric 2.92. The distance function is given by the principal angles  $\theta_i$  between the subspaces

$$d_g^2(X, Y) = \|\theta\|_2^2 = \sum_{i=1}^p \theta_i^2, \quad (2.95)$$

where the the principal angles can be obtained by computing the singular value decomposition of  $X^TY$ .

$$X^TY = U\Sigma V^T = U \cos \Theta V^T \quad (2.96)$$

$$\Sigma = \text{diag}(\sigma_1, \dots, \sigma_p) \quad (2.97)$$

$$\Theta = \text{diag}(\theta_1, \dots, \theta_p) = \text{diag}(\arccos \sigma_1, \dots, \arccos \sigma_p). \quad (2.98)$$

The distance function (2.95) has the disadvantage that due to the occurrence of the arccosine and the singular value decomposition, analytic expression are much harder to obtain.

To avoid this problem, following Absil's [3] approach, an equivalent norm can be chosen, the so-called projection Frobenius norm, given by

$$d_P^2(X, Y) = \frac{1}{2} \|XX^T - YY^T\|_F^2 = \sum_{i=1}^p \sin^2 \theta_i. \quad (2.99)$$

**First derivatives of the distance function**

$$\frac{\partial d^2(X, Y)}{\partial X} = 2(XX^T - YY^T)X. \quad (2.100)$$

**Second derivatives of the distance function**

$$\frac{\partial^2 d^2(X, Y)}{\partial X \partial X} = 2[(X^T X \otimes \mathbb{1}_n) + (\mathbb{1}_p \otimes (XX^T - YY^T)) + (X^T \otimes X) K_{np}]. \quad (2.101)$$

The mixed derivative is given by

$$\frac{\partial^2 d^2(X, Y)}{\partial X \partial Y} = -2[(X^T Y \otimes \mathbb{1}_n) + (X^T \otimes Y) K_{np}]. \quad (2.102)$$

## 2.5 Fréchet derivatives of matrix logarithm and square root

To use the derivative expressions computed above, one needs the so-called Kronecker form of the Fréchet derivative. The Fréchet derivative of a matrix valued function  $f : \mathbb{R}^{n \times n} \rightarrow \mathbb{R}^{n \times n}$  at a point  $X \in \mathbb{R}^{n \times n}$  is a linear function mapping  $E \in \mathbb{R}^{n \times n}$  to  $L_f(X, E) \in \mathbb{R}^{n \times n}$  such that

$$f(X + E) - f(X) - L_f(X, E) = o(\|E\|). \quad (2.103)$$

Chain rule and inverse function theorem also hold for the Fréchet derivative:

$$L_{f \circ g}(X, E) = L_f(g(X)), L_g(X, E)) \quad (2.104)$$

$$L_f(X, L_{f^{-1}}(f(X), E)) = E. \quad (2.105)$$

As the formulation of the derivatives of the distance function, the Fréchet derivative can also be brought in the Kronecker form in which it is represented as map  $K_f : \mathbb{R}^{n^2} \rightarrow \mathbb{R}^{n^2}$ , such that  $K_f(X) \in \mathbb{R}^{n^2 \times n^2}$  is defined by

$$\text{vec}(L_f(X, E)) = K_f(X) \text{vec}(E). \quad (2.106)$$

Here  $\text{vec} : \mathbb{R}^{n \times n} \rightarrow \mathbb{R}^{n^2}$  denotes the column-wise vectorization operator.

### 2.5.1 Derivative of the matrix square root

Start by considering the Fréchet derivative of  $f(X) = X^2$ , which is given by

$$L_{X^2}(X, E) = XE + EX. \quad (2.107)$$

Applying the inverse function theorem consequently leads to

$$L_{X^2}(X^{\frac{1}{2}}, L_{X^{\frac{1}{2}}}(X, E)) = X^{\frac{1}{2}}L_{X^{\frac{1}{2}}}(X, E) + L_{X^{\frac{1}{2}}}(X, E)X^{\frac{1}{2}} = E, \quad (2.108)$$

where the last equality shows that the Fréchet derivative of the matrix square root  $L_{X^{\frac{1}{2}}}(X, E)$  satisfies the Sylvester equation

$$X^{\frac{1}{2}}L + LX^{\frac{1}{2}} = E, \quad L := L_{X^{\frac{1}{2}}}(X, E). \quad (2.109)$$

The Kronecker representation  $K_{X^{\frac{1}{2}}}(X)$  can now be obtained by using the vectorization operator on both sides of the equation and rearrange the term to the form (2.106) which leads to

$$K_{X^{\frac{1}{2}}}(X) = \left[ \left( \mathbb{1} \otimes X^{\frac{1}{2}} \right) + \left( X^{\frac{1}{2}T} \otimes \mathbb{1} \right) \right]^{-1}. \quad (2.110)$$

Since the main application of this computation will be for the case  $n = 3$ , (2.110) can be directly implemented by explicitly calculating the inverse of the  $9 \times 9$  matrix  $(\mathbb{1} \otimes X^{\frac{1}{2}}) + (X^{\frac{1}{2}T} \otimes \mathbb{1})$ .

For general applications with much larger  $n$ , however, this approach has the disadvantage that the inverse of a  $n^2 \times n^2$  matrix needs to be computed, which has computational complexity  $\mathcal{O}((n^2)^3) = \mathcal{O}(n^6)$ . In that case, it might be favorable to choose a basis for  $\mathbb{R}^{n \times n}$  and solve the Sylvester equation (2.109) for each of the  $n^2$  basis matrix elements individually. This is shown for the Kronecker representation of the matrix logarithm in the next section.

### 2.5.2 Derivative of the matrix logarithm

For the logarithm, the implementation follows the approach described by Al-Mohy et al [5] which is based on the differentiation of the Padé approximant to  $\log(1 + X)$ . Since the application is only valid if the spectral radius of  $X$  is sufficiently small, the use of an inverse scaling and squaring technique based on the relation

$$\log(X) = 2 \log(X^{\frac{1}{2}}) \quad (2.111)$$

is necessary.

Application of the chain rule leads to

$$L_{\log}(X, E_0) = 2 \log\left(X^{\frac{1}{2}}, L_{X^{\frac{1}{2}}}(X, E_0)\right). \quad (2.112)$$

The second argument on the right hand side can again be written as solution  $E_1 := L_{X^{\frac{1}{2}}}(A, E_0)$  of an Sylvester-type equation

$$X^{\frac{1}{2}} E_1 + E_1 X^{\frac{1}{2}} = E_0. \quad (2.113)$$

Repeating the procedure  $s$  times results in

$$L_{\log}(X, E_0) = 2^s L_{\log}\left(X^{\frac{1}{2^s}}, E_s\right) \quad (2.114)$$

$$X^{\frac{1}{2^i}} E_i + E_i X^{\frac{1}{2^i}} = E_{i-1}, \quad i = 1, \dots, s \quad (2.115)$$

where  $E_s$  is obtained by successively solving the set of Sylvester equations defined in the second line.

Finally, the Padé approximant of order  $m$  in its partial fraction form [17] is given by

$$r_m(X) = \sum_{j=1}^m \alpha_j^{(m)} (\mathbb{1} + \beta_j^{(m)} X)^{-1} X \quad (2.116)$$

where  $\alpha_j^{(m)}, \beta_j^{(m)} \in (0, 1)$  are the  $m$ -point Gauss-Legendre quadrature weights and nodes.

The derivative of (2.116) is then easily computed as

$$L_{r_m}(X, E) = \sum_{j=1}^m \alpha_j^{(m)} (\mathbb{1} + \beta_j^{(m)} X)^{-1} E (\mathbb{1} + \beta_j^{(m)} X)^{-1} \quad (2.117)$$

which leads to the final approximation of the matrix logarithm derivative,

$$L_{\log}(X, E) \approx 2^s L_{r_m}\left(X^{\frac{1}{2^s}} - \mathbb{1}, E_s\right). \quad (2.118)$$

For the implementation of (2.118), algorithm 5.1 from [5] with fixed  $m = 7$  is used.

Choose  $E^{ij}$ , the single-entry matrices having 1 at  $(i, j)$  and zero everywhere else, as a basis for  $\mathbb{R}^{n \times n}$  and compute the Fréchet derivative for every  $E^{ij}$ . Then, by constructing its rows from the vectorized, transposed Fréchet derivatives, the final Kronecker form of the derivative can be obtained by

$$(K_{\log X})_{in+j,\cdot} = \text{vec}(L_{\log}(X, E^{ij})^T). \quad (2.119)$$

# Chapter 3

## The Manifold Total Variation Minimization Template Library

The manifold total variation minimization template library (MTVMTL), which was developed in the course of this thesis is an easy-to-use, fast C++14 template library for TV minimization of manifold-valued two- or three-dimensional images.

The following chapter summarizes the capabilities of the library and introduces into its architecture from a software engineering as well as high performance computing point of view. The last part, describing the components in more detail, can also be understood as a high level documentation of the library and includes some basic tutorial on its usage.

### 3.1 Capabilities

The following list provides a first overview of the implemented features. More detailed information are found in the description of the components in Section 3.3 and the examples in Section 3.4.4.

#### Manifolds

- Real Euclidean space  $\mathbb{R}^n$
- Sphere  $S^n = \{x \in \mathbb{R}^{n+1} : \|x\| = 1\}$
- Special orthogonal group  $SO(n) = \{Q \in \mathbb{R}^{n \times n} : QQ^T = \mathbb{1}, \det(Q) = 1\}$
- Symmetric positive definite matrices  $SPD(n) = \{S \in \mathbb{R}^{n \times n} : S = S^T, x^T S x > 0 \forall x \in \mathbb{R}^n \setminus \{0\}\}$
- Grassmann manifold  $Gr(n, p) = St(n, p)/O(p)$

#### Data

- 2D and 3D images
- Input/Output via OpenCV integration supporting all common 2D image formats
- CSV input for matrix valued data
- Input methods for raw volume image data as well as the NIfTI [24] format for DT-MRI images
- Various methods to identify damaged areas for inpainting

## Functionals

- isotropic (only possible for IRLS) or anisotropic TV functionals
- first order TV term
- weighting and inpainting possible

## Minimizer

- Iteratively reweighted least squares using Riemannian Newton method
- Proximal point

## Visualizations

- OpenGL rotated cubes visualization for SO(3) images
- OpenGL ellipsoid visualization for SPD(3) images
- OpenGL volume renderer for 3D volume images

## 3.2 Design concepts

The next sections give more insights in the implementation details of the algorithms introduced in the last chapter. The first part discusses the performance relevant changes in data representation and computation with respect to the Matlab prototype, which is followed by a discussion of structural changes to make MTVMTL as modular and extendable as possible.

The next part is then dedicated especially to the question where and how parallelization is used in the implementation. A related question is also the use of new language features of the C++11 and C++14 language standards which allow for a real compact formulation of the parallel code segments. The section closes with a short description of those features.

### 3.2.1 Goals

Traditionally, there has always been a trade-off between performance and usability requirements such as maintainability or extendability. A good example for that is the Basic Linear Algebra Subprograms (BLAS) library, written in Fortran, and still considered one of the fastest libraries in existence. For supercomputers, even versions with hand-optimized assembly code are used, nevertheless calling the library directly from another high level language like C or C++ is quite cumbersome. The code becomes larger and much harder to read.

Languages like C++, on the other hand, offer a lot of expressive power and make it possible, through object oriented generic programming, to write compact, reusable and even fast, though not as fast as Fortran, code. Nevertheless, with the development of template metaprogramming techniques C++ is able to avoid the performance-usability trade-off to a certain degree, using very elaborate compile time optimizations. Classical examples for these techniques are expression templates [30], also used by the Eigen linear algebra library, and specifically variadic templates, as used by MTVMTL. C++ was consequently the ideal choice for achieving high performance and the usability requirements.

### Performance

Since the core parts of the implementation are originally based on a Matlab prototype by Sprecher [16], [10] and [23], one of the most important goals was a faster implementation with a smaller memory footprint. On the test platform with two hyper-threaded 2.8GHz cores (Intel i5-2520) with

AVX vector extensions, the Matlab implementation froze for images larger than one Megapixel(MP).

Hence, the C++ implementation should enable the algorithm to be tested in a much broader scope which is also closer to common picture sizes in image processing, especially since even smart phones today easily produce pictures in the Megapixel range. In addition to that, also other factors affecting the performance of the algorithm, such as cache locality and memory speed, can be investigated.

The main performance driver for this library is the multilevel-parallelization. Evidently, this does not include the formulation of the IRLS minimization algorithm itself, due to the fact that it is naturally an iterative method, but rather any possible subtask such as computation of the functional values, gradient and Hessian, for example. On top of that, it was tried to maximize cache locality on the loop level and free memory as soon as possible. On the other hand, data that is used very often and requires costly recomputation, like the IRLS weights, are kept in memory.

In contrast to the original Matlab implementation, the computation of various quantities such as weights, first and second derivatives is not realized with tensor products any more. For Matlab, due to the low speed of its internal loop constructs, the approach is justified but in a pure C++ implementation other factors are more important. One reason for the change is improved readability and maintainability of the code, since tensor products usually tend to become very convoluted, especially for the manifolds with matrix representations. Also the modularization of the manifold class is not straightforward any more, because the tensor products cannot be expressed as binary operation depending on two manifold data points.

From a performance and parallelization perspective, contractions of tensor products are similar to matrix products and usually require some sort of blocking scheme for parallelization. In addition to that, because certain reshapes of the image container prior to the computation are necessary, the dimensions to be summed over are not necessarily contiguous in memory. A high cache utilization is consequently more difficult to achieve.

Finally, in order to formulate certain operations as tensor products, temporary tensors of the correct dimensionality need to be created, which increases the memory consumption.

Another measure that significantly reduces the memory footprint for the IRLS minimizer, especially for manifolds with matrix representations, is to only save gradient and Hessian in their local tangent space basis representation, such that the degrees of freedom correspond the intrinsic manifold dimension and not the dimension of the embedding space. This also reduces the time to solve the sparse linear system.

## Modularization and Extendability

In principle the programming paradigm in Matlab is still procedural resulting in a hierarchy of functions for the various tasks. Handling different types of manifolds then usually requires `switch` expressions in all functions that use manifold-specific functionality. Adding support for a new manifold to the algorithm or modifying existing manifold functionality makes a modification of all `switch` cases necessary. There is no single point of change but many source files need to be edited.

For the MTVMT Library an object oriented and generic programming approach was chosen, which tries to model each variable component of the algorithm in a separate class, as independent of the other components as possible. For general information on C++ design paradigm see, for example, [2] or [6]. Differences in each class are represented by specializations of their primary class template. The best example for that is the manifold class which has a specialization for every supported manifold type and due to the fact that the functions implemented in those class specializations are generally just functions of one or two elements of the manifold, they could also be used in other projects which require the same functionality.

Interfaces between classes are provided by giving classes higher in the hierarchy template parameters

corresponding to lower classes: The class modelling the functional, for instance, has a manifold type template parameter, as described in more detail in Section 3.3. Like all other component classes, also the functional class can be extended by adding further specializations for other types of functionals, that include for example higher order terms or have different fidelity terms [32].

Those specializations also have the advantage that the code is just in one file - a single point of change - to increase readability and maintainability.

### 3.2.2 Levels of parallelization

Parallelization takes place on two levels. The first one is shared memory multi-threading implemented with the OpenMP (OMP) language extensions. In most cases this is realized using the so-called *pixel-wise kernels* of the Video++ (VPP) library, which makes it possible to map an arbitrary function on all pixels of a set of image containers: The function is called for each tuple of pixels having the same coordinates in their respective image. For the parallel execution each processor is assigned a batch of image rows. If the pixel-wise kernels are not applicable, for example if the needed subdomain of the image is too complicated, manual OpenMP loop parallelization is used. Due to the fact that the 3D pixel-wise constructs are not implemented in the current version of VPP, also an own 3D version of the pixel-wise kernels was implemented using OpenMP and variadic templates to keep the code compact.

The alternative to the tensor product implementation is to use pixel-wise kernels to parallelize any operation that requires iteration over an image container. For most computations, take for instance the case of computing derivatives, only the pixel and its next neighbor in a given dimension are needed. For calculating the forward derivatives one just has to call the pixel-wise kernel with two subimages of the current working image: One with the last slice (of the given dimension) missing and one with the first slice missing. At this point it must be noted that the concept of subimages does not involve any copies but just works by using different addressing schemes for the same data in the memory. The pixel-wise constructs are demonstrated in the following short Listing 3.1 and further illustrated in Figure 3.1:

---

**Listing 3.1** Pixel-wise forward derivative computation

---

```

1 auto calc_first_arg_deriv = [&] (value_type& x, const weights_type& w, const <
2   value_type& i, const value_type& n) { MANIFOLD::deriv1x_dist_squared(i, n, x); x *= <
3   w; };
4
5 img_type YD1 = img_type(without_last_row);
6 vpp::pixel_wise(YD1, weightsY_.without_last_row, data_.img_ | without_last_row, <
7   data_.img_ | without_first_row) | calc_first_arg_deriv;

```

---

The advantage is that even though some function is evaluated for a pair of neighboring pixels which are not adjacent in memory, the parallel processing is still always row-wise. Since rows in row-major languages like C++ are contiguous in memory, one can avoid frequent memory access on distant locations and consequently avoid cache thrashing to a certain degree.

The second level of parallelization is instruction level parallelism, also known as *Single Instruction Multiple Data* (SIMD), which uses the processor's vector extensions (e.g. SSE, AVX, NEON). The CPU provides some additional, special SIMD registers with increased size of usually 128 bits to 512 bits such that multiple integer or floating point variables fit inside. Then an arithmetic operation is simultaneously applied to all variables in the register (see Figure 3.2) such that theoretically the amount of floating point operations is multiplied by the number of variables fitting in the register.

In order to achieve this speedup the data must be aligned in memory, which means the addresses of pixels in memory must always be a multiple of the SIMD register size. Fortunately, that issue is handled by the VPP and Eigen libraries enabling the compiler to perform the necessary vectorization optimizations.

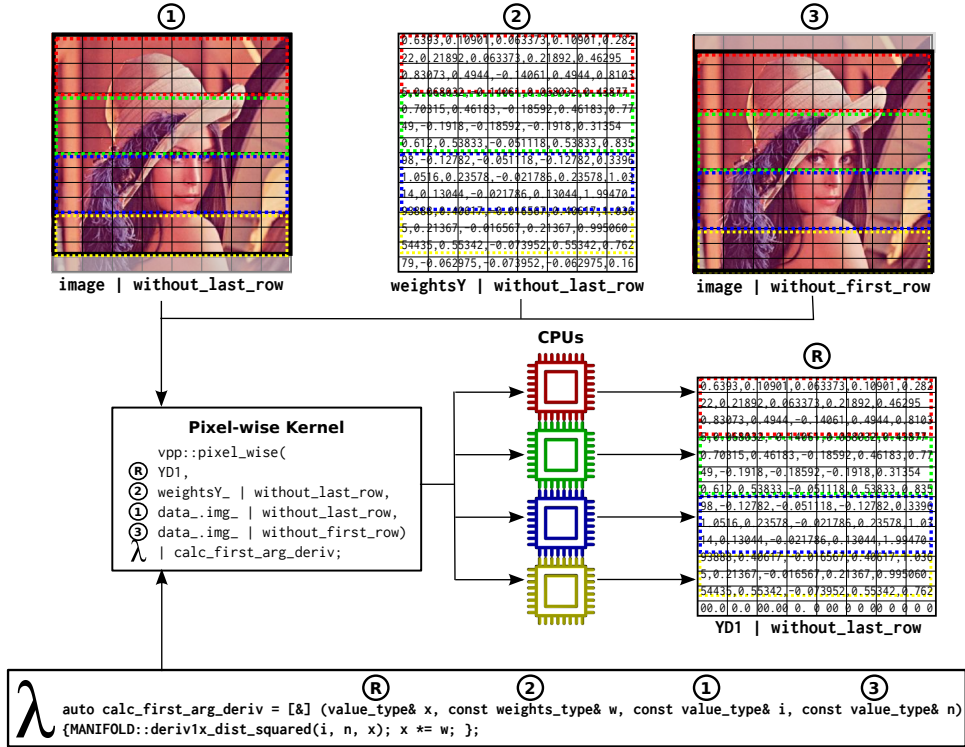


Figure 3.1: Parallel calculation of derivatives in  $y$ -direction and weighting using pixel-wise kernels. For each pixel position  $(i, j)$  in the three input pictures, ①, ② and ③, as well as in the output picture ④, the pixel-wise kernel creates a tuple  $(R_{ij}, 2_{ij}, 1_{ij}, 3_{ij}) = (\text{YD1}_{i,j}, \text{weightY}_{i,j}, \text{Image}_{i,j}, \text{Image}_{i+1,j})$  which is then used to call the specified lambda function. Depending on the row number of the pixel, the calls are executed by different CPU cores.

### (a) 4 Scalar Operations

(b) 1 SIMD Operation

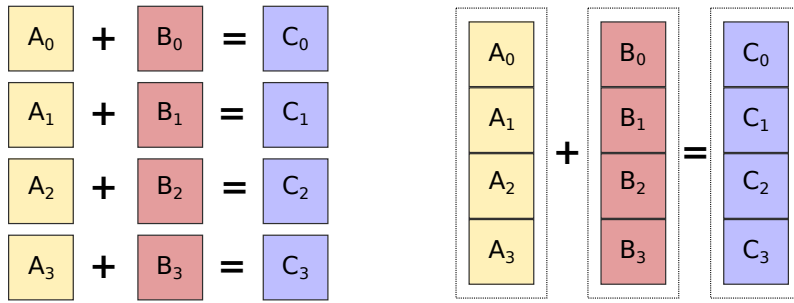


Figure 3.2: Instruction level parallelism using SIMD registers.

### 3.2.3 C++ techniques

The MTVMT Library tries to take advantage of new C++11 and C++14 language features in order to speed up computations via compile-time optimizations and also make the code more compact and readable. The most important tools in that regard are lambda functions and variadic templates which are shortly described in the following section. For more details check, for example [20].

## Lambda functions

A lambda function is basically a locally defined function object, which is able to capture variables from the surrounding scope. The function can but needs not to be named. The corresponding Matlab language construct is an anonymous function or function handle, usually defined using the @ operator. The following listing shows the basic definitions and use cases of lambda functions:

---

**Listing 3.2 Lambda functions**

---

```
1 int init = 5;
2 std::vector<int> v {1, 2, 3, 4};
3
4 // C++11 lambda function for adding integers
5 // init is captured by reference
6 auto f = [&] (int a, int b) {return a + b + init;};
7
8 // C++14 generic argument lambda function
9 // init is captured by value
10 auto g = [=] (auto a, auto b) {return a + b + init;};
11
12 // Call named lambda functions
13 int d = f(8, 3);
14 double e = g(1.0f, 5);
15
16 // or directly pass anonymous lambda function as argument
17 std::transform(v.begin(), v.end(), v.begin(), [] (auto x) { ++x; });
```

---

In the MTVMT library, lambda functions provide the connection between the static manifold methods and the pixel-wise kernels which apply them to the image containers. A typical case can be seen in the already introduced listing 3.1. Since lambda functions are only locally defined, in the scope where they are actually needed, one can avoid making the method list of the classes unnecessary long.

## Variadic templates

With variadic templates it is possible to define functions which take a variable number of arguments. Obviously, this is also possible in other languages like Matlab or C with the most prominent example being the function `printf`. However, this is usually implemented using some list type (in C: `va_list`), which adds additional overhead, whereas in C++ it is realized via a special kind of template metaprogramming technique, which is recursive in nature. The recursion, in turn, is resolved at compile-time and leads to code that is actually equivalent to manually defining a function with the desired number of arguments, and consequently there is no additional runtime effort.

---

**Listing 3.3 Variadic template example**

---

```
1 // Recursion base case
2 template<typename T>
3 T sum(T v) {
4     return v;
5 }
6
7 // Recursive template
8 template<typename T, typename... Args>
9 T sum(T first, Args... args) {
10     return first + sum(args...);
11 }
```

---

The main application for this constructs in MTVMTL is the implementation of the Karcher mean, needed for the proximal point implementation, and MTVMTL's own version of the 3D pixel-wise kernels.

## 3.3 Components

In the following section the different components of the library are discussed. For the manifold class, this will be done in more detail to enable users to use new or customized manifold classes. A general overview of all the components is provided in Figure 3.3.

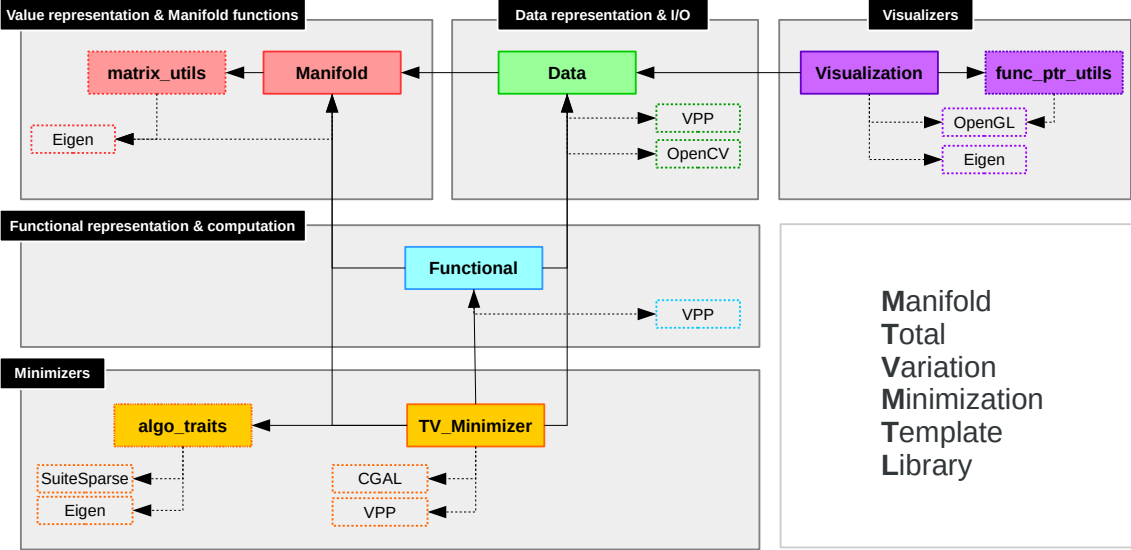


Figure 3.3: Overview of the class hierarchy and dependencies between the library components and also third party libraries

### 3.3.1 Manifold class

The manifold template class encapsulates all information and methods related to the differential geometric structure of the data. This enables the generic implementation of the functionality higher in the class hierarchy such as functional evaluations or minimizers. The primary template has the following parameters

---

```

1 // Primary Template
2 template <enum MANIFOLD_TYPE MF, int N, int P=0>
3 struct Manifold {
4 };

```

---

where **MF** is an enumeration constant to specify the type of the manifold, **N** denotes the dimension of the representation space and **P** the dimension of subspaces, as in the case of Grassmann manifolds. In order to add a new manifold one just has to implement a specialization of this primary template.

So far, the manifold class contains functionality necessary for TV minimization using either the IRLS or proximal point algorithm and furthermore some additional operations that are needed for supporting tasks like interpolation and smoothing. The class specializations are implemented using only static constants and methods: At no time it is necessary or desired to actually instantiate the class. The methods itself are usually unary or binary functions, with parameters and result all passed by reference to avoid copies. Since these methods are called very often, basically for every pair of neighboring pixels, they are all declared **inline** in order to support the compiler during the code optimization.

It is also possible to use these class specializations in other projects requiring similar functionality, like for instance when implementing a geodesic finite element solver.

In the following, excerpts of the SPD implementation are shown to illustrate which information and functionality a new manifold class needs to provide and to give an overview of the available functions.

#### Static constants

---

```

1 static const MANIFOLD_TYPE MyType;           // SPD
2 static const int manifold_dim;               // N*(N+1)/2
3 static const int value_dim;                  // N*N
4

```

---

```
5 static const bool non_isometric_embedding;
```

The first constant just stores the manifold template parameter introduced above, while `manifold_dim` and `value_dim` are the intrinsic dimensions of the manifold and of its embedding space, respectively. Finally, the Boolean constant is just a flag which tells the algorithm that special pre- and post-processing for interpolation is necessary.

## Type definitions

To allow the generic formulation of the algorithms, the manifold class provides a mapping between the types of their values, derivatives, tangent bases and underlying scalar type and their actual representation as matrix and vector data types of the Eigen linear algebra library. Examples can be seen in the following listing:

```
1 // Scalar and value typedefs
2 typedef double scalar_type;
3 typedef double dist_type;
4 typedef Eigen::Matrix<scalar_type, N, N> value_type;
5 // ...
6
7 // Tangent space typedefs
8 typedef Eigen::Matrix<scalar_type, N*N, N*(N+1)/2> tm_base_type;
9 // ...
10
11 // Derivative Typedefs
12 typedef value_type deriv1_type;
13 typedef Eigen::sMatrix<scalar_type, N*N, N*N> deriv2_type;
14 typedef Eigen::Matrix<scalar_type, N*(N+1)/2, N*(N+1)/2> restricted_deriv2_type;
15 // ...
```

## Static methods

Finally, the following methods are implemented for the manifold classes.

### Riemannian distance function and its derivatives

```
1 inline static dist_type dist_squared(cref_type x, cref_type y);
2 // First derivatives
3 inline static void deriv1x_dist_squared(cref_type x, cref_type y, deriv1_ref_type result);
4 inline static void deriv1y_dist_squared(cref_type x, cref_type y, deriv1_ref_type result);
5 // Second derivatives
6 inline static void deriv2xx_dist_squared(cref_type x, cref_type y, deriv2_ref_type result);
7 inline static void deriv2xy_dist_squared(cref_type x, cref_type y, deriv2_ref_type result);
8 inline static void deriv2yy_dist_squared(cref_type x, cref_type y, deriv2_ref_type result);
```

### Exponential and Logarithm map

```
1 template <typename DerivedX, typename DerivedY>
2 inline static void exp(const Eigen::MatrixBase<DerivedX>& x, const Eigen::MatrixBase<DerivedY>& y, const Eigen::MatrixBase<DerivedX>& result);
3 inline static void log(cref_type x, cref_type y, ref_type result);
4
5 inline static void convex_combination(cref_type x, cref_type y, double t, ref_type result);
```

The parameters of the exponential here are not the manifolds own `typedefs` but the base class of all Eigen matrix data types. The reason for using this construction is that the function can also be called with composite expressions (e.g.  $XY + Z$ ) without a temporary copy. Most of the other functions are usually called with atomic expressions only, hence there is no need to use this more complicated construction on a general basis.

The `convex_combinations` method computes the point  $z$  on the manifold reached by following a unit speed geodesic connecting the points  $x$  and  $y$  for a time  $t$ .

## Karcher mean

```
1 inline static void karcher_mean(ref_type x, const value_list& v, double tol=1e-10, int maxit=15);
2 inline static void weighted_karcher_mean(ref_type x, const weight_list& w, const value_list& v, double tol=1e-10, int maxit=15);
3
4 // Variadic templated version
5 template <typename V, class ... Args>
6 inline static void karcher_mean(V& x, const Args&... args);
```

Implementations for finding the Karcher mean of an arbitrary number of points. The first version requires the points to be stored in a `std::vector` container while the second version is based on variadic templates and expects the arguments just as a comma separated list after the first argument, where the final result will be stored. Creating the list for the first version eventually requires copying and is consequently slower but has an overloaded version which allows to compute a weighted Karcher mean

## Tangent plane basis, projector and interpolation

```
1 // Basis transformation for restriction to tangent space
2 inline static void tangent_plane_base( cref_type x,  tm_base_ref_type result);
3 // Projection
4 inline static void projector(ref_type x);
5 // Interpolation pre- and postprocessing
6 inline static void interpolation_preprocessing(ref_type x);
7 inline static void interpolation_postprocessing(ref_type x);
```

The first function computes a basis of the tangent space at the point  $x$  and stores it in `result`, as columns of a matrix.

The projector, if defined for the given manifold, will project a point of the ambient embedding spacing onto the manifold. This might either be an actual projector in the mathematical sense or, as in the Euclidean case, a cutoff function which maps the data back into the desired value range ( $[0, 1]^n$  in the Euclidean case).

Interpolation pre- and postprocessing is necessary for instance for the SPD manifold. Other manifolds must just provide an empty implementation.

### 3.3.2 Data class

The data class handles anything related to storage, input and output of two- or three-dimensional image data, as well as some support functions for detecting edges and damaged areas in a picture. In contrast to the manifold class, the data class needs to be instantiated such that a reference to the data object can be passed to any class which needs data access. In addition to the dimension of the picture, the data class takes a fully specialized manifold class type as a template parameter:

```
1 // Primary Template
2 template <typename MANIFOLD, int DIM >
3 class Data {
4};
```

There are basically four multi-dimensional arrays stored in the data class: The original noisy image, the current working image and, if applicable, arrays storing the inpainting and edge weight information. For storage, the n-dimensional VPP [15] image container is used.

This image container class works very well together with the Eigen vector and matrix data types, provides a variety of expressive loop- and iterator constructs and also takes care of the alignment of the image data in memory, which is a prerequisite for the *Single Instruction Multiple Data* (SIMD) optimization and vectorization by the compiler. Since the memory management of the container is based on `std::shared_ptr`, it is also very easy to efficiently access subimages or slices of an image without any copies.

The most common input methods for 2D and 3D are summarized in the following code snippet:

---

```

1 // 2D Input functions
2 void rgb_imread(std::string filename); // for R^3
3 void rgb_readBrightness(std::string filename); // for R
4 void rgb_readChromaticity(std::string filename); // for S^2
5 void readMatrixDataFromCSV(std::string filename, const int nx, const int ny);
6
7 // Synthetic SO/SPD picture
8 void create_nonsmooth_son(const int ny, const int nx);
9 void create_nonsmooth_spd(const int ny, const int nx);
10
11 //3D Input functions
12 void rgb_slice_reader(std::string filename, int num_slides);
13 void readMatrixDataFromCSV(std::string filename, const int nz, const int ny, const int nx);
14 void readRawVolumeData(std::string filename, const int nz, const int ny, const int nx);
15
16 // Output Functions
17 void rgb_saveimage(std::string fname); // save image
18 void rgb_show(); //open images viewer
19
20 void output_matval_img(std::string filename) const; // save in CSV format

```

---

The purpose and usage of most of these methods is self-explanatory. The CSV readers expect the data to be a linear list of pixels, where the components of each pixel are comma-separated and row-wise flattened, such that each line of the input file contains exactly one pixel. The order of the list is row-wise for 2D or slice-wise, then row-wise for 3D images, respectively.

The slice reader reads a series of images, following the filename scheme `filenameX.ext`, where X is the number of the slice to be read into an image cube at z-coordinate X.

### 3.3.3 Functional class

In addition to fully specialized Manifold and Data class types (third and fourth template parameters), there are three further template parameters that must be specified by the library user. The first one is the order of the functional which refers to the order of the highest differential operator in the TV term of the functional. So far, only first order functionals are implemented which corresponds to setting `ord=FIRSTORDER` in the primary template shown below.

---

```

1 //Primary Template
2 template <enum FUNCTIONAL_ORDER ord, enum FUNCTIONAL_DISC disc, class MANIFOLD, class DATA, int DIM=2>
3 class Functional{
4 };

```

---

The second template parameter `disc` determines whether the isotropic or the anisotropic version is to be used. Please note that for the proximal point algorithm only anisotropic is available. Finally, the last parameter specifies the dimensionality of the data.

The main purpose of the functional class is to provide methods for the computation of all functional-related quantities, such as evaluation of the functional, its gradient, Hessian and construction of a local basis of the tangent spaces. That also means that in the IRLS case the functional class stores the sparse linear system that needs to be solved in each Newton step.

For users of the library, the most important methods are those for setting the  $\lambda$  and  $\epsilon^2$  parameters.

---

```

1 inline param_type getlambda() const { return lambda_; }
2 inline void setlambda(param_type lam) { lambda_=lam; }
3 inline param_type geteps2() const { return eps2_; }
4 inline void seteps2(param_type eps) { eps2_=eps; }

```

---

Should it be necessary, it is also possible to access some of the stored quantities directly using

---

```

1 // Evaluation functions
2 result_type evaluateJ();
3 void evaluateDJ();
4 void evaluateHJ();
5
6 void updateTMBase();
7
8 inline const gradient_type& getDJ() const { return DJ_; }
9 inline const sparse_hessian_type& getHJ() const { return HJ_; }
10 inline const tm_base_mat_type& getT() const { return T_; }

```

---

The functions in lines 3, 4 and 6 merely trigger a recomputation while the last three functions return references to these quantities. `evaluateJ()` returns the functional value and triggers the recomputation of the weights.

### 3.3.4 TV minimizer class

For the TV minimizer class it makes sense to consider the IRLS and proximal point implementation separately. The primary template is shown in the following code snippet.

---

```

1 // Primary Template
2 template <enum ALGORITHM AL, class FUNCTIONAL, class MANIFOLD, class DATA, enum \
3   PARALLEL PAR=OMP, int DIM=2>
4 class TV_Minimizer{
5 };

```

---

As in the previous cases one has to provide fully specialized manifold, data and also functional types. Again, the last parameter specifies the dimension of the data. Of the remaining two parameters, `PAR` has the default value `OMP`, which specifies the method of parallelization, in this case the OpenMP language extensions. Other methods, including just serial execution, could be added later. The remaining template parameter, `AL` specifies the minimizer to be used and can take the values `IRLS` or `PRPT` (Proximal point).

For IRLS, the public class interface looks like

---

```

1 void first_guess();           // First guess for inpainting
2 void smoothening(int smooth_steps); // Simple averaging box filter
3 void newton_error_type newton_step(); // perform one newton step
4 void minimize();             // full minimization
5
6 // Getters and Setters for parameters
7 void setMax_runtime(int t) { max_runtime_ = t; }
8 void setMax_irls_steps(int n) { max_irls_steps_ = n; }
9 void setMax_newton_steps(int n) { max_newton_steps_ = n; }
10 void setTolerance(double t) { tolerance_ = t; }
11
12 int max_runtime(int t) const { return max_runtime_; }
13 int max_irls_steps(int n) const { return max_irls_steps_; }
14 int max_newton_steps(int n) const { return max_newton_steps_; }
15 int tolerance(double t) const { return tolerance_; }

```

---

and for proximal point it is

---

```

1 use_approximate_mean(bool u) { use_approximate_mean_ = u; } // turn mean approximation \
2   on/off
3 void first_guess();                                // First guess for \
4   inpainting
5
6 void updateFidelity(double muk);                // Update Fidelity part
7 void updateTV(double muk, int dim, const weights_mat& W); // Update TV part
8
9 void geod_mean();                  // Calculate geodesic mean
10 void approx_mean();                // approximate mean using convex combinations
11
12 void prpt_step(double muk); // perform one proximal point step
13 void minimize();                 // full minimization
14
15 // Getters and Setters for parameters
16 void setMax_runtime(int t) { max_runtime_ = t; }
17 void setMax_prpt_steps(int n) { max_prpt_steps_ = n; }
18
19 int max_runtime(int t) const { return max_runtime_; }
20 int max_prpt_steps(int n) const { return max_prpt_steps_; }

```

---

### 3.3.5 Visualization class

This class provides visualizations of 3D volume data and so far  $\text{SO}(3)$  and  $\text{SPD}(3)$  visualizations by cubes and ellipsoids. If these are to be used in user code it is necessary to link against OpenGL, GLUT and GLEW libraries, which is explained in more detail in section 3.4.3. The visualization class has the following primary template.

---

```

1 // Primary Template
2 template <enum MANIFOLD_TYPE MF, int N, class DATA, int dim=2>
3 class Visualization{
4 };

```

---

The class methods that are relevant to users of the library are summarized here:

---

```

1 void saveImage( std::string filename );
2 void GLInit( const char* windowname );
3
4 void paint_inpainted_pixel( bool setFlag );

```

---

The important function here is `GLInit` which initializes the rendering of the data. If one intends to also save the image, one has to specify a filename using `saveImage` before calling `GLInit`. Finally, `paint_inpainted_pixel` just sets a flag which decides whether inpainted pixels are not painted at all (`setFlag = false`, default value) or if they are visualized with the value they have at the time of rendering. Usually one wants to set this to true after the minimization to show the results.

A complete example is presented in section 3.4.4

### SO(3) visualization

For the visualization of SO(3) data a unit volume cube centered at the origin of  $\mathbb{R}^3$  with its front face normal vector parallel to the y-axis is created. Then the rotation matrix representing the SO(3) element is applied to the cube.



Figure 3.4: SO(3) Visualization as oriented, colored cubes

### SPD(3) visualization

For SPD(3) matrices, there are six degrees of freedom, which in the case of DT-MRI pictures correspond to the diffusion coefficients in different directions. Those can be visualized by ellipsoids using three degrees of freedom for their orientation in space and the remaining three for the lengths of their semi-axis.

Starting with the unit sphere centered at the origin, eigenvectors and eigenvalues are computed for every SPD matrix. Due to the SPD property a full basis of eigenvectors with positive eigenvalues always exists. The diagonal matrix formed by the vector of eigenvalues is applied as a scaling transformation of the coordinate axis. The matrix whose columns are the computed eigenvectors can then be interpreted as a rotation (or principal axis transformation of the ellipsoid).

To avoid large size difference and overlaps between the ellipsoids one should also normalize the eigenvalues using the mean diffusivity  $\mu$  defined by

$$\mu = \frac{1}{3} \sum_{i=1}^3 \lambda_i. \quad (3.1)$$

Finally, the color is defined by normalizing the largest eigenvector, called the principal direction, and mapping its coordinates to the RGB color space, such that clusters of similar orientations can be more easily visually distinguished.

In the case of 3D SPD images the rendering window also provides some controls over the view. The up and down arrow keys can be used to zoom in and out of the picture, left and right keys pivot the camera and with the `s` key, the image is saved using the filename specified before.

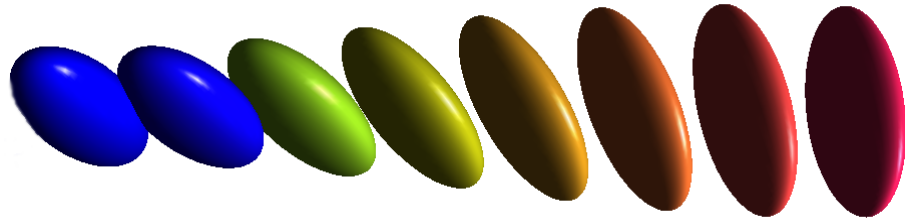


Figure 3.5:  $\text{SPD}(3)$  Visualization as oriented, colored ellipsoids

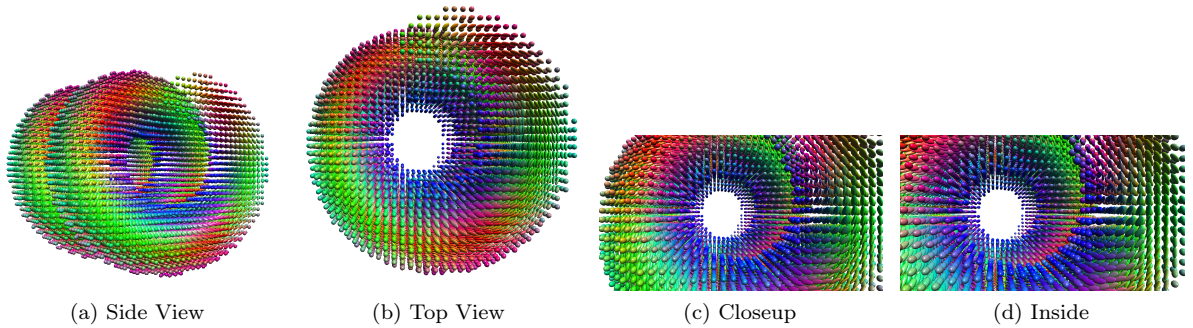


Figure 3.6: Example of the 3D data Visualization of  $\text{SPD}(3)$  images from different viewpoints. The 'helix' synthetic tensor data set, produced with the `tend` program in the Teem toolkit[29]

### 3D volume image rendering

The volume image renderer just transforms the data to a 3D texture which is then mapped onto a cube rotating about the z-axis. Plasticity is created by setting the alpha channel of each displayed voxel to the intensity value of the corresponding data voxel, such that dark areas are more transparent. The following Figure 3.7 shows the rendered volume from different angles.

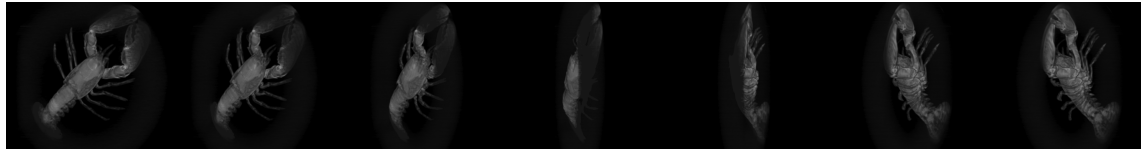


Figure 3.7: 3D Volume image using texture based rendering.

### 3.3.6 Utility functions

#### Algorithm traits

The algorithm traits class contains standard values for the IRLS algorithm, like the number of IRLS iterations, number of Newton iterations and maximal runtime. It also contains the standard solver for the linear system. If the solver needs to be switched it must be changed in this file. All other parameters can be changed using the methods provided by the TV minimizer class.

#### Matrix functions

In the file `matrix_utils.hpp` additional matrix functions not included in the Eigen library are implemented. So far, these are only the methods for the computation of the Fréchet derivatives of matrix square root and logarithm, as well as their Kronecker representations.

## Function pointers utilities

Located in the file `func_ptr_utils.hpp`, there are some auxiliary functions needed to transform pointers to class member functions to plain C function pointers. The latter are required by the OpenGL and GLUT library API.

## 3D pixel-wise kernels

The 3D version of the pixel-wise kernels along with useful tools based on them, for copying or filling 3D images.

## 3.4 Using MTVMTL

The following section serves as tutorial and illustrates the steps that must be taken from the installation to the first compiled code using the library. In the first part mandatory and optional requirements are listed, then installation of the library and the compilation process are explained. Finally, three use cases are illustrated with code examples.

### 3.4.1 Prerequisites

The main dependencies of MTVMTL are the *Eigen* C++ template library for linear algebra and the *Video++* video and image processing library. Those libraries, as well as MTVMTL's core functionality are provided as header-only libraries. There are, however, some additional static libraries that are recommended to speed up the computation, enable easy I/O or which are needed for visualization of the results. To administer all these different parts, and because the header-only libraries require additional compiler flags for the code optimization, MTVMTL also relies on the *CMake* installation tool for installation and compilation of user code using MTVMTL.

The following list shows the needed packages for the usage of MTVMTL:

- CMake ( $\geq 2.8.0$ )
- gcc ( $\geq 4.9.1$ ), any C++14 compatible compiler should also be possible but is untested.
- Eigen ( $\geq 3.2.5$ )
- Video++ (a version will be provided with the MTVMTL, otherwise consider [15] )
- Boost ( $\geq 1.56$ ) (also needed for CGAL)

Recommended are also the following packages. They are needed if any of the described extended functionality needs to be used.

- OpenCV ( $\geq 2.4.9$ ), for image input and output, edge detection for inpainting
- CGAL ( $\geq 4.3$ ), for first guess interpolation during inpainting
- OpenGL ( $\geq 3.0$ ), GLEW( $\geq 1.10$ ) and freeGLUT( $\geq 2.8.1$ ), for visualizations of SPD, SO and any 3D data
- SuiteSparse ( $\geq 4.2.1$ ), faster parallel sparse solver for the linear system in the IRLS algorithm
- SuperLU ( $\geq 4.3$ ), faster parallel sparse solver for the linear system in the IRLS algorithm

Some care must be taken with the version recommendations. Usually there are no compatibility issues if only the minor software version changes but for major version updates it must be checked whether the new version's API is still backwards compatible.

### 3.4.2 Installation

Using CMake, the installation of the library is very easy. The procedure is described for a Linux system here. Since CMake is a platform-independent tool, the installation consists of two steps: First, creating the installation files for a platform-*dependent* make-system, in this case the Unix tool `make`, using CMake and second, the actual installation using `make`.

Once the library is downloaded, change into the directory of the library containing the `mtvmtl` folder and the `CMakeLists.txt` file. Next, create the installation files in the current directory or in a newly created one. The latter is done by

```
1 mkdir build
2 cd build
3 cmake ..
```

The last command will prepare the installation at the standard location of libraries on the system, which is usually `/usr/include` or `/usr/local/include`. If this location is not desired or possible, due to access restrictions on the system, an alternative installation path has to be provided as additional parameter:

```
1 cmake .. -DCMAKE_INSTALL_PREFIX=/path/to/desired/location/
```

Finally, start the installation by typing

```
1 make install
```

which will perform not only the installation of MTVMT library but also of the VPP library and its dependencies. Note that all other libraries utilized by MTVMT need to be installed manually. This is, however, not a problem since they are usually included in the package manager of every major Linux distribution.

### 3.4.3 Compilation of own projects using CMake

For the compilation of user code using CMake a file with the name `CMakeLists.txt` must be provided in the same directory as the user code. Note that this file is used to compile code using the library and is different from the `CMakeLists.txt` file provided for the library installation. This file contains all the information about the locations of header files and external library code as well as compiler optimization flags.

In Listing 3.4 an example is provided for the compilation of a user application `my_executable` with a single source file `mysource.cpp`. The example is minimal in the sense that it is only for the compilation of a single executable and maximal in the sense that it links the executable against any possible external library used by MTVMTL.

The most important lines for the user are the last two. In the first of these lines, an executable is added by providing its name (`my_executable`) and the source file(s) (`mysource.cpp`) it depends on. Next, one must specify the external libraries the executable is linked against using the `target_link_libraries()` command. It expects the executable as the first parameter and then a space-separated list of all target libraries.

**Listing 3.4** Example `CMakeLists.txt`

```
1 cmake_minimum_required(VERSION 2.8)
2
3 list(APPEND CMAKE_MODULE_PATH "/FULL/PATH/TO/MTVMTL/INSTALLATION/LOCATION/include/\
... mtvmtl/SparseSuiteSupport")
4
5 find_package(OpenGL REQUIRED)
6 find_package(GLUT REQUIRED)
7 find_package(GLEW REQUIRED)
8 include_directories( ${OPENGL_INCLUDE_DIRS} ${GLUT_INCLUDE_DIRS} )
9
10 find_package(OpenCV REQUIRED)
11 find_package(CGAL REQUIRED)
```

```

12 include(${CGAL_USE_FILE})
13
14 find_package(Cholmod REQUIRED)
15 find_package(SuperLU REQUIRED)
16
17 include_directories(${CMAKE_CURRENT_SOURCE_DIR} /... /usr/include/superlu /usr/include/ \
18   eigen3
19 /FULL/PATH/TO/MTVMIL/INSTALLATION/LOCATION/)
20 add_definitions(-std=c++14 -g -fopenmp)
21 add_definitions(-Ofast -march=native)
22 add_definitions(-DNDEBUG)
23
24 add_executable(my_executable mysource.cpp)
25 target_link_libraries(my_executable gomp ${OpenCV_LIBS} ${CGAL_LIBRARIES} ${\
26   CHOLMOD_LIBRARIES} ${SUPERLU_LIBRARIES} ${OPENGL_LIBRARIES} ${GLUT_LIBRARY} ${\
27   GLEW_LIBRARIES})

```

---

In the following steps it will be assumed that the library was installed to `/usr/include`. Furthermore, the current working directory is `/home/username/myMTVMproject`, which contains some code the user has written using MTVMIL, namely `mysource.cpp`. Thus, the `CMakeLists.txt` should be created in the same directory and the placeholders in lines 3 and 18 of Listing 3.4 should be modified to `/usr/include/mtvmtl/SparseSuiteSupport` and `/usr/include`, respectively.

For the actual compilation, create a separate directory called `project_build` and change to this directory.

```

1 mkdir project_build
2 cd project_build

```

---

Next, call `cmake` providing the source directory which contains your `CMakeLists.txt` file as argument.

```

1 cmake ../src/

```

---

If everything was configured correctly, the output should look similar to the following.

```

1 --- The C compiler identification is GNU 4.9.2
2 --- The CXX compiler identification is GNU 4.9.2
3 --- Check for working C compiler: /usr/bin/cc
4 --- Check for working C compiler: /usr/bin/cc -- works
5 --- Detecting C compiler ABI info
6 --- Detecting C compiler ABI info - done
7 --- Detecting C compile features
8 --- Detecting C compile features - done
9 --- Check for working CXX compiler: /usr/bin/c++
10 --- Check for working CXX compiler: /usr/bin/c++ -- works
11 --- Detecting CXX compiler ABI info
12 --- Detecting CXX compiler ABI info - done
13 --- Detecting CXX compile features
14 --- Detecting CXX compile features - done
15 --- Found OpenGL: /usr/lib64/libGL.so
16 --- Found GLUT: /usr/lib64/libglut.so
17 --- Found GLEW: /usr/include
18 --- Build type: Release
19 --- USING CXXFLAGS = '-march=corei7 -mtune=native -O2 -pipe -msse3 -msse4 -mcx16 -msahf \
20   -mpopcnt -frounding-math -O3 -DNDEBUG'
21 --- USING EXEFLAGS = '-Wl,-O1 -Wl,--as-needed '
22 --- Targetting Unix Makefiles
23 --- Using /usr/bin/c++ compiler.
24 --- Requested component: MPFR
25 --- Requested component: GMPXX
26 --- Requested component: GMP
27 --- Found CHOLMOD: /usr/include
28 --- Found SUPERLU: /usr/include/superlu
29 --- Configuring done
30 --- Generating done
30 --- Build files have been written to: [path-to-build-folder]/project_build

```

---

Finally, type

```

1 make my_executable

```

---

to build the program resulting in the creation of the final executable program `my_executable` in the folder `/home/username/myMTVMproject/project_build/`.

### 3.4.4 Tutorial and typical use cases

The basic process of using the library is to explicitly specify the necessary template parameters for all needed components. For the sake of compactness and readability this should be done using `typedefs`. In the next step one can then instantiate the classes and start implementing.

#### Image denoising, vectorial color model

As a first example, denoising of a simple color picture using the IRLS minimizer is demonstrated. In a first step the necessary classes need to be included. For the sake of shortening the code the namespace `tvmtl` of the library is used.

---

**Listing 3.5** Inclusion of library headers

---

```
1 #include <tvmtl/core/algo_traits.hpp>
2 #include <tvmtl/core/tvmin.hpp>
3
4 using namespace tvmtl;
```

---

Next, specify the manifold type and data type, in this case Euclidean  $\mathbb{R}^3$  and a corresponding 2D image container

---

**Listing 3.6** Specification of manifold and data type

---

```
1 typedef Manifold< EUCLIDIAN, 3 > mf_t;
2 typedef Data< mf_t, 2 > data_t;
```

---

Note that the data type must be specified using the *fully* specialized manifold class type defined in the line before.

The data type is now ready for work such that the input data can be read in the next few lines.

---

**Listing 3.7** Initialization and input of image data

---

```
1 data_t myData=data_t();           // Creating the data object
2 myData.rgb_imread(filename);     // Reading an image file, filename is a const char*
```

---

After the data object is ready one must specify the functional, in this example first order TV, isotropic and 2D. Again, also the fully specialized manifold and data class types need to be given as template parameters. The last template parameter, the dimension of the data, has default value 2 and can also be omitted in this case.

---

**Listing 3.8** Defining the functional and setting parameters

---

```
1 typedef Functional<FIRSTORDER, ISO, mf_t, data_t, 2> func_t;
2 func_t myFunc(lambda, myData);    // Creation of the functional object
3 myFunc.seteps2(1e-10);           // Specify the epsilon parameter
```

---

For the instantiation of the functional you need to pass the  $\lambda$  for your functional as well as your newly created data object. The `seteps2` method sets the value of  $\epsilon^2$  for the reweighting computation. In case of the proximal point algorithm it should be set to zero.

---

**Listing 3.9** Choosing the minimizer, smoothing and minimization

---

```
1 typedef TV_Minimizer<IRLS, func_t, mf_t, data_t, OMP, 2> tvmin_t;
2 tvmin_t myTVMMin(myFunc, myData); // Creation of minimizer object
3
4 myTVMMin.smoothening(5);          // smoothing to obtain better starting value
5 myTVMMin.minimize();              // Starts the minimization
```

---

Finally, choose the minimizer, in this case IRLS, and pass functional, manifold and data types as template parameters. The OMP parameter is not fully implemented yet and is supposed to provide choice between different parallelization schemes or also completely serial computation. The last parameter again has default value 2 and describes the dimension of the data.

The complete listing of this example can be found in Appendix A.

### Colorization using color inpainting

In the following a more complicated example is shown: Recolorization of an image where most ( $\approx 99\%$ ) *color* information has been removed. This means that this problem is defined on the product manifold  $S^2 \times \mathbb{R}$ . Optimization, however, will only take place on  $S^2$  while the  $\mathbb{R}$  data part is only needed to obtain edge information. Also three auxiliary functions (`removeColor`, `DisplayImage`, `recombineAndShow`) are used here that are not shown in the code snippets but will be included in the full listing in Appendix A. This time, also some of the minimization parameters are obtained from the command line:

---

**Listing 3.10** Include library files and read parameters from standard input

---

```

1 #include <iostream>
2 #include <string>
3 #include <cmath>
4
5 #include <opencv2/highgui/highgui.hpp>
6 #include <mtvmtl/core/algo_traits.hpp>
7 #include <mtvmtl/core/data.hpp>
8 #include <mtvmtl/core/functional.hpp>
9 #include <mtvmtl/core/tvmin.hpp>
10
11 #include <vpp/vpp.hh>
12 #include <vpp/utils/opencv_bridge.hh>
13
14 using namespace tvmtl;
15
16 int main(int argc, const char *argv[])
17 {
18     if (argc < 3){
19         std::cerr << "Usage : " << argv[0] << " image [lambda] [threshold]" << std::endl;
20         return 1;
21     }
22
23     double lam=0.01;
24     double threshold=0.01;
25
26     if(argc == 4){
27         lam=atof(argv[2]);
28         threshold=atof(argv[3]);
29     }
30
31     std::string fname(argv[1]);
32
33     //...
34
35 }
```

---

Here `threshold` defines the percentage of color information that remains in the picture.

In the next step, make the necessary type definitions for manifold and data classes and create the data objects.

---

**Listing 3.11** Manifold and Data class type definitions and instantiation

---

```

1 // typedefs
2 typedef Manifold< SPHERE, 3 > spheremf_t;    // S^2
3 typedef Manifold< EUCLIDIAN, 1 > eucmf_t;      // R
4
5 typedef Data< spheremf_t, 2> chroma_t;        // Chromaticity part
6 typedef Data< eucmf_t, 2> bright_t;           // Brightness part
7
8 // Instantiation
9 chroma_t myChroma=chroma_t();
10 bright_t myBright=bright_t();
```

---

When the data containers are ready, one needs to read the input picture, extract color and brightness information and store it in the respective objects. This problem is basically a color inpainting problem but the reconstructed color should not blur across edges in the picture. This can be solved by making use of the edge weights array that is stored together with the image. Edges can be detected in the brightness part of the picture and used in the chromaticity denoising procedure. Finally, the color is removed in the following way: Create a random inpainting matrix where the probability a certain pixel is set to false is given by the `threshold` variable and then replace every RGB pixel by the mean of its three color components (those pixels are basically grayscale then).

The necessary steps are shown in the next listing

---

**Listing 3.12 Color and brightness input, edge detection and color removal**

```

1 myBright.rgb_readBrightness(argv[1]);      // Extract brightness from filename argv[1]
2 myBright.findEdgeWeights();                // Detect edges and store in matrix
3
4 myChroma.rgb_readChromaticity(argv[1]);    // Extract chromaticity from filename argv[1]
5 myChroma.inpaint_=true;                   // Turn inpainting on
6 myChroma.setEdgeWeights(myBright.edge_weights_); // Initiliazie chromaticity part edges with brightness part edges
7 myChroma.createRandInpWeights(threshold); // Create random inpainting matrix
8 removeColor(myChroma, myBright);          // Remove color
9
10 // Recombine chromaticity and brightness and show the colorless image
11 recombineAndShow(myChroma, myBright, "colorless_" + fname, "Colors removed Picture");

```

---

The next part works almost exactly as in the last example. Define functional, set its parameters, then define the minimizer. The only difference is that one has to run `first_guess` before the minimization.

---

**Listing 3.13 Functional and minimizer definition, first guess and minimization**

```

1 typedef Functional<FIRSTORDER, ISO, spheremf_t, chroma_t> cfunc_t;
2 typedef TV_Minimizer<IRLS, cfunc_t, spheremf_t, chroma_t, OMP> ctvmin_t;
3
4 cfunc_t cFunc(lam, myChroma);           // create functional object
5 cFunc.seteps2(1e-10);                  // set eps^2 parameter
6
7 ctvmin_t cTVMMin(cFunc, myChroma);     // create minimizer object
8 cTVMMin.first_guess();                 // first guess
9
10 std::cout << "Start TV minimization..." << std::endl;
11 cTVMMin.minimize();
12
13 // Recombine Brightness and Chromaticity parts of recolored Picture
14 recombineAndShow(myChroma, myBright, "recolored_" + fname, "Recolored Picture");

```

---

Some visual results of the above code are also shown in Section 4.1.4.

### 3D DT-MRI data denoising and visualization

As a final example, a more complicated manifold,  $SPD(3)$  in this case, is chosen, as well as 3D data to demonstrate the use of the visualization classes. Moreover, the proximal point algorithm will be used in this example. The CSV reader just reads a list of pixels where the numerical values comprising the pixel are stored comma-separated, one pixel per line. The CSV file has no header such that the dimensions must be provided as command line parameters.

---

**Listing 3.14 Initialization**

```

1 #include <iostream>
2 #include <cstdlib>
3 #include <string>
4 #include <sstream>
5
6 #include <mtvmtl/core/algo_traits.hpp>
7 #include <mtvmtl/core/data.hpp>
8 #include <mtvmtl/core/functional.hpp>
9 #include <mtvmtl/core/tvmin.hpp>
10 #include <mtvmtl/core/visualization.hpp>
11
12 int main(int argc, const char *argv[])
13 {
14     int nz, ny, nx;
15     nz = std::atoi(argv[2]);
16     ny = std::atoi(argv[3]);

```

```

17     nx = std::atoi(argv[4]);
18
19     std::stringstream fname;
20     std::string nfname;
21     fname << "dt13d" << nz << "x" << ny << "x" << ny << ".png";
22     nfname = "noisy_" + fname.str();
23
24     // ...
25
26     return 0;
27 }
```

---

Since the meaning of the individual components should be clear by now, all the necessary type definitions are made at once in the next listing

**Listing 3.15** Type definitions, Visualization type

```

1 using namespace tvmtl;
2
3 typedef Manifold< SPD, 3 > mf_t;
4 typedef Data< mf_t, 3> data_t;
5 typedef Functional<FIRSTORDER, ANISO, mf_t, data_t, 3> func_t;
6 typedef TV_Minimizer< PRPT, func_t, mf_t, data_t, OMP, 3 > tvmin_t;
7 typedef Visualization<SPD, 3, data_t, 3> visual_t;
```

---

The only innovation is the aforementioned Visualization class. The first 3 in its template parameter list is the embedding dimension of the manifold and the last 3 denotes the dimension of the data. Note this time it was necessary to specify it for the functional and minimizer classes, as well, because the default value is 2. The remaining parameters specify the manifold type via an enumeration constant (in the same way one specifies it for the Manifold class) and the data type via a fully specialized data class type.

Prior to the minimization, one usually wants to display the original noisy data and eventually save it to a file. The necessary steps are as follows:

**Listing 3.16** Data input and displaying the noisy data

```

1 data_t myData = data_t(); // Create data object
2 myData.readMatrixDataFromCSV(argv[1], nz, ny, nx); // Read from CSV file
3
4 visual_t myVisual(myData); // Create visualization object
5 myVisual.saveImage(nfname); // Specify file name to save a screenshot
6
7 std::cout << "Starting OpenGL-Renderer..." << std::endl;
8 myVisual.GLInit("SPD(3) Ellipsoid Visualization"); // Start the Rendering
```

---

In the last step, create functional and minimizer class, perform the minimization and display the denoised data again.

**Listing 3.17** Minimization and final rendering

```

1 double lam=0.7;
2 func_t myFunc(lam, myData); // Functional object
3 myFunc.seteps2(0); // eps^2 should be 0 for PRPT
4
5 tvmin_t myTVMIn(myFunc, myData); // Minimizer object
6
7 std::cout << "Start TV minimization..." << std::endl;
8 myTVMIn.minimize();
9
10 std::string dfname = "denoised(prpt)_" + fname.str();
11 myVisual.saveImage(dfname); // Specify name for denoised image
12
13 std::cout << "Starting OpenGL-Renderer..." << std::endl;
14 myVisual.GLInit("SPD(3) Ellipsoid Visualization"); // Render
```

---

The resulting picture for this example is shown in 4.3.3.

# Chapter 4

## Applications and Numerical Experiments

In the first part of the chapter the algorithms are applied to a variety of problems in image processing, computer vision, medical imaging and related fields. The second part will be dedicated to a performance analysis of the IRLS algorithm, a comparison to the proximal point minimizer and will close with a numerical experiment investigating the dependence of the solution on changes in the noisy picture. This is a first step in extending the IRLS algorithm towards recursive splitting into subdomain.

The test platform is a Linux machine with two hyper-threaded 2.8GHz cores Intel i5-2520 (thus a total of four hardware threads) with AVX vector extensions and 8 GB RAM.

### 4.1 Image denoising

The most basic application of the algorithm is denoising of a common 2D grayscale or color pictures. For grayscale pictures the TV minimization is performed over the Euclidean manifold  $M = \mathbb{R}$ , while for color pictures there is either  $M = \mathbb{R}^3$  for the linear-vectorial model or  $M = S^2 \times \mathbb{R}$  for the non-linear chromaticity-brightness model.

#### 4.1.1 Grayscale

As introductory example and for the sake of completeness, Figure 4.1 shows results from denoising a grayscale image.

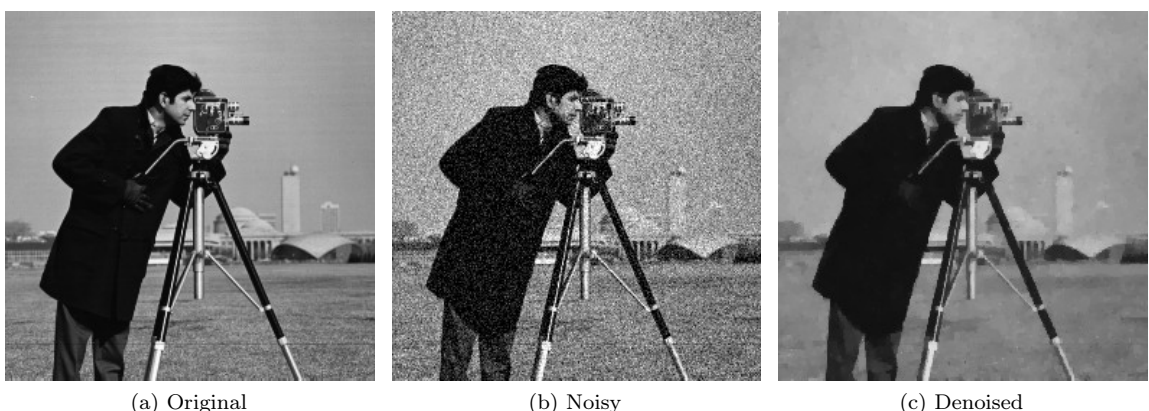


Figure 4.1: Denoising of a grayscale image taking values in the manifold  $\mathbb{R}$  (a) Original image "Cameraman.bmp", 256 × 256 px, 8 bit depth (b) Component-wise Gaussian noise  $\mu = 0$ ,  $\sigma = 0.01$  added (c) Denoised, IRLS with  $\lambda = 0.09$ , 5 IRLS steps, 1 Newton step per IRLS step

### 4.1.2 Color

In this example TV minimization of color images using the two different color models is performed. In Figure 4.2 results are shown for the among the image processing community well-known *Lena* picture, which is rather small in size. Minimization in the linear-vectorial color model using 5 IRLS iterations with one Newton step per reweighting is completed within 9.2 seconds.

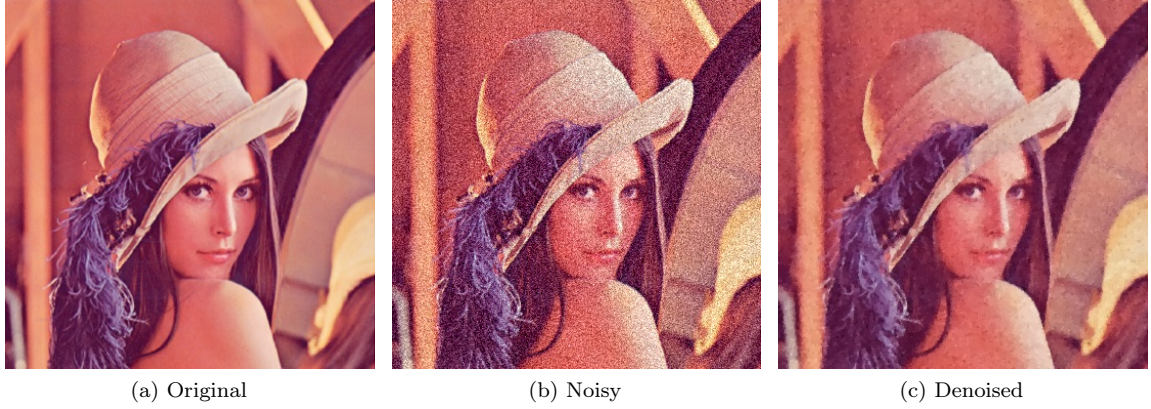


Figure 4.2: Denoising of a color image using the linear vectorial color model which corresponds to the manifold  $\mathbb{R}^3$  (a) Original image "Lena.jpg",  $361 \times 361$  px, 8 bit color depth (b) Component-wise Gaussian noise  $\mu = 0$ ,  $\sigma = 0.1$  added (c) Denoised, IRLS with  $\lambda = 0.1$ , 5 IRLS steps, 1 Newton step per IRLS step

Next, using the same model and parameters a different image with a size already in the megapixel range is denoised. The needed time, however, is with 272.6 seconds quite high. The result can be seen in Figure 4.3.

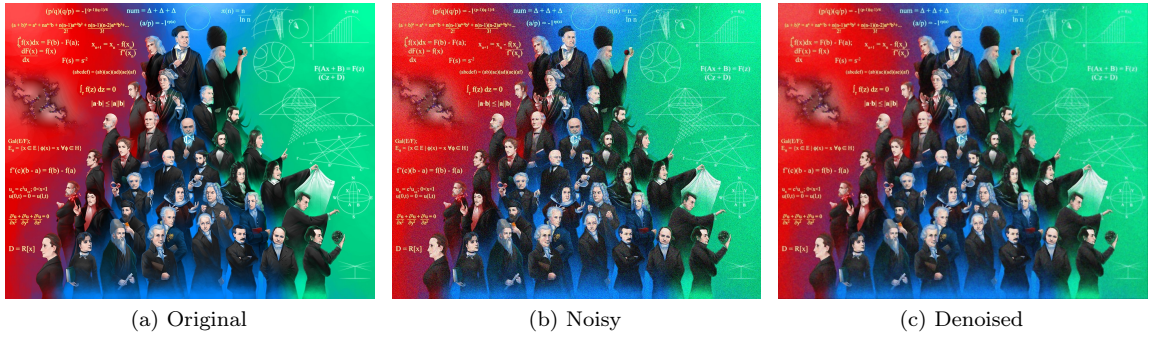


Figure 4.3: Denoising of color images using the linear vectorial color model which corresponds to the manifold  $\mathbb{R}^3$  (a) Original image "mathematicians.jpg",  $1280 \times 1024$  px, 8 bit color depth (b) Component-wise Gaussian noise  $\mu = 0$ ,  $\sigma = 0.1$  added (c) Denoised, IRLS with  $\lambda = 0.1$ , 5 IRLS steps, 1 Newton step per IRLS step

Finally, in Figure 4.4 a third picture is denoised using the chromaticity-brightness model. Here minimization over the product manifold  $S^2 \times \mathbb{R}$  is performed by denoising the chromaticity( $S^2$ ) and the brightness( $\mathbb{R}$ ) separately, which has the added advantage of more fine-grained control over the process because two  $\lambda$  parameters can be chosen separately for each part, too.

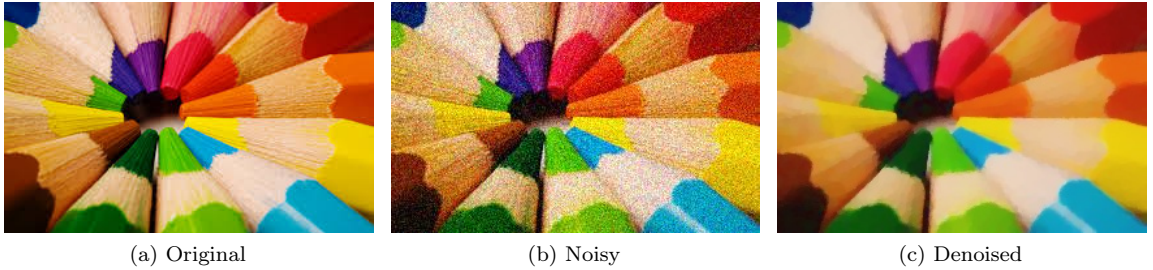


Figure 4.4: Denoising of a color image using the CBR color model over the manifold  $S^2 \times \mathbb{R}$  (a) Original image "crayons.jpg",  $284 \times 177$  px, 8 bit color depth (b) Component-wise Gaussian noise  $\mu = 0$ ,  $\sigma = 0.1$  added (c) Denoised, IRLS with  $\lambda_{S^2} = \lambda_{\mathbb{R}} = 0.1$ , 5 IRLS steps, 1 Newton step per IRLS step

#### 4.1.3 Inpainting

The next example is a damaged picture where a considerable part has been overpainted with blue color. In the first step the damaged region is detected which in this case is done via a simple color selector (e.g. all pixels with a blue value larger than 0.95). In principle many other selection methods known from common raster graphic editors could be implemented here as well.

Next, a first guess is calculated using scattered linear interpolation and lastly the TV minimization itself is performed. The process is summarized in Figure 4.5.

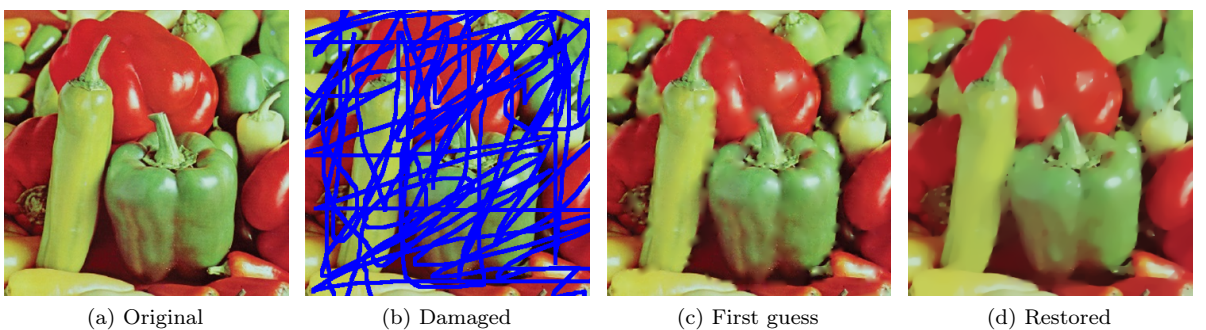


Figure 4.5: Inpainting of a color image using the linear vectorial color model which corresponds to the manifold  $\mathbb{R}^3$  (a) Original image "Pepper.png",  $359 \times 361$  px, 8 bit color depth (b) Damaged by overpainting with blue color (c) First guess via component-wise scattered interpolation (d) Restored, IRLS with  $\lambda = 0.12$ , 5 IRLS steps, 1 Newton step per IRLS step

#### 4.1.4 Recolorization

Colorization, also known as color inpainting, because it is basically just a special case of inpainting, is performed in the next example. Here the picture is not necessarily noisy but it is assumed that only the brightness of each pixel is known, while the chromaticity is known only for a low ratio  $r = 0.01$  of all pixels. Note that this splitting implies that inpainting and TV minimization takes place only on  $S^2$ .

As in the previous example, one first has to detect all damaged, i.e. non-colored, pixels to inpaint. Again scattered interpolation is used to obtain a first guess which is depicted in Figure 4.6c. One can observe that red color runs into green regions. To avoid this, the edges need to be detected in the brightness part using the Canny edge detector [9], for example. This can be used then to set the edge weights for the chromaticity part accordingly. As a result, one indeed obtains sharp and clear edges in the final result 4.6d.

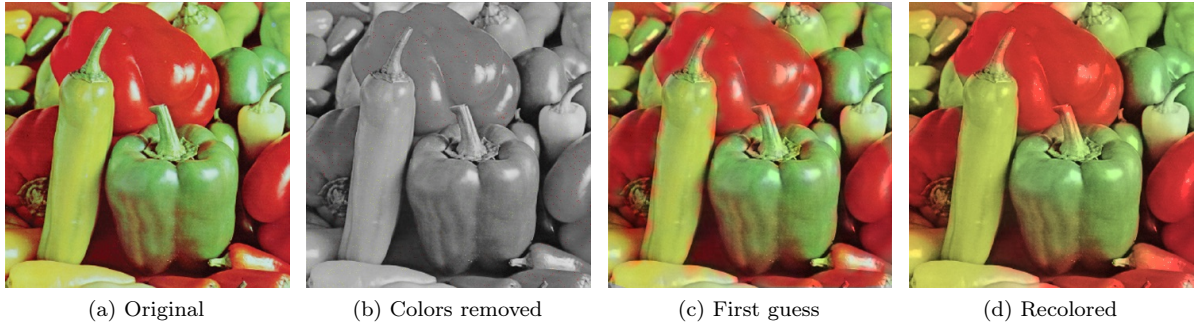


Figure 4.6: Recolorization using color inpainting in the Chromaticity-Brightness color model, corresponding to  $S^2 \times \mathbb{R}$  (a) Original image "Pepper.jpg",  $359 \times 361$  px, 8 bit color depth (b) Image with a ratio of approximately 0.01 remaining colored pixels (c) First guess via component-wise scattered interpolation (d) Recolored, IRLS with  $\lambda = 0.01$ , 5 IRLS steps, 1 Newton step per IRLS step

#### 4.1.5 Volume images

The picture section concludes with an example of a 3D volume image as they might occur in medical imaging from magnetic resonance imaging (MRI) or computed tomography. In this demonstration, however, the so-called *Boston teapot* is chosen, taken from a volume image library [31] and component-wise Gaussian noise is added. The image represents only intensity values, hence minimization is performed over  $\mathbb{R}$ . The results are shown in Figure 4.7.

For this picture the proximal point algorithm is used, because the memory and computational requirements of the IRLS for a picture of this size are very high: In section 2.3.4 it was shown that the dimension of the sparse linear system is  $\dim(M)XYZ$  which in this case amounts to  $1.1 \times 10^7$ , which is the length of the gradient while the Hessian will contain  $7.7 \times 10^7$  non-zero-entries. The solution of a sparse linear system of that size is computationally very demanding while in comparison the geodesic averaging and Karcher mean calculations simplify to mostly vectorized addition and subtraction operations on a simple manifold like  $\mathbb{R}$ .

As a result, the IRLS minimization of the  $64 \times 64 \times 64$  volume image in 4.8, which shows the simulation of fuel injection into a combustion chamber, already takes 1100 seconds on the test platform, compared to only 109 seconds for the proximal point minimization of the much larger teapot image.

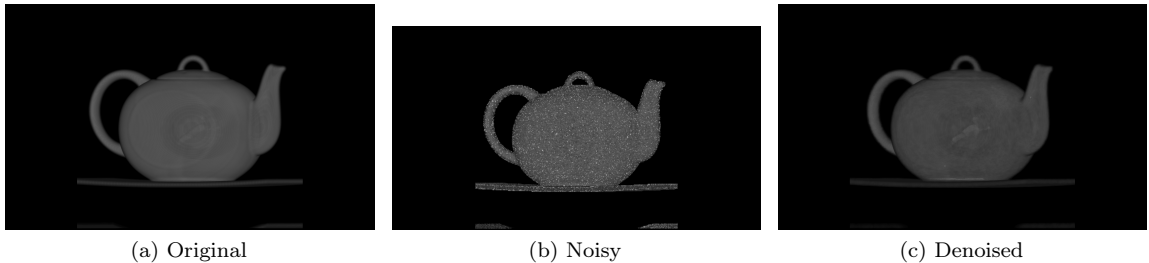


Figure 4.7: Denoising a 3D grayscale volume image (a) Original image "BostonTeapot.raw",  $256 \times 256 \times 178$  px, 8 bit color depth (b) Component-wise Gaussian noise  $\mu = 0$ ,  $\sigma = 0.1$  added (c) Denoised, proximal point with  $\lambda = 0.1$ , 50 PRPT steps

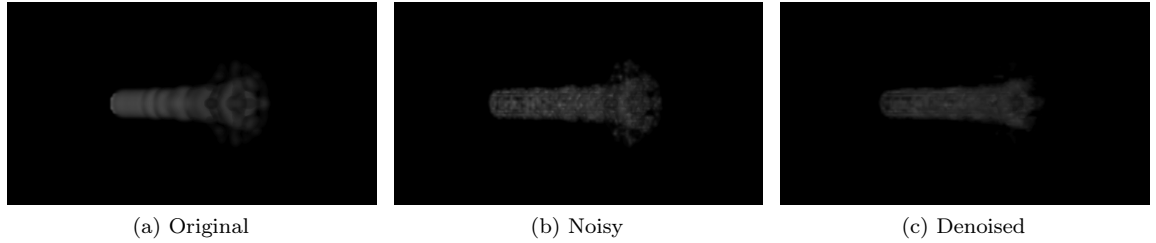


Figure 4.8: Denoising a 3D grayscale volume image (a) Original image "FuelInjection.raw",  $64 \times 64 \times 64$  px, 8 bit color depth (b) Component-wise Gaussian noise  $\mu = 0, \sigma = 0.1$  added (c) Denoised, IRLS with  $\lambda = 0.2$ , 5 IRLS steps with 1 Newton step per reweighting

## 4.2 SO(2) and SO(3) image data

For the  $SO(n)$  test, firstly, non-smooth synthetic data is created. It consists of four regions in each of which orientations vary rather smoothly. Sudden jumps in orientation occur when moving across the region boundaries. This is what can be considered an edge in  $SPD$ -valued data. Secondly, the algorithm is applied to two real data examples based on fingerprint matching and video motion analysis.

### 4.2.1 Synthetic data

The following synthetic  $SO(3)$  image is constructed in the following way. Let  $\Omega = \{1, \dots, 30\}^2$  and define for every  $(i, j) \in \Omega$  a rotation axis

$$v = \begin{cases} (2x, y, 0)^T, & x > 0.5 \\ (0, 2x, 0.5)^T, & \text{else} \end{cases}, \quad (4.1)$$

where  $x = \frac{j}{30}, y = \frac{i}{30}$  and a rotation angle

$$\alpha = \begin{cases} x + y, & x > y \\ \frac{\pi}{2} + x - y, & \text{else} \end{cases}. \quad (4.2)$$

Then assign the corresponding  $SO(3)$  element representing a rotation by  $\alpha$  and about  $v$ . Noise is added componentwise and the noisy matrix is then projected back to  $SO(3)$  using the projector  $P_{SO(n)}(A) = UV^T$  where  $A = U\Sigma V^T$  is the singular value decomposition of  $A$ .

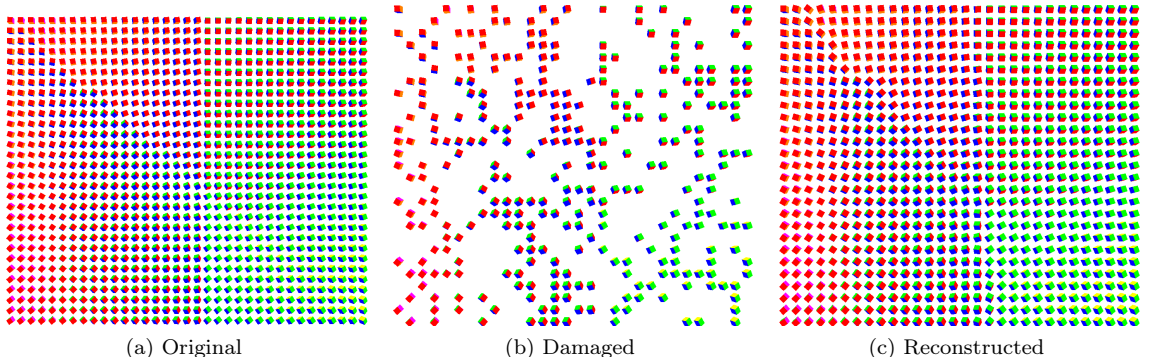


Figure 4.9: Inpainting of synthetic  $SO(3)$  picture (a) Original image: Synthetic, non-smooth  $SO(3)$ ,  $30 \times 30$  px (b) Threshold  $p = 0.4$  (c) Denoised, IRLS with  $\lambda = 0.1$ , 5 IRLS steps, 1 Newton step per IRLS

### 4.2.2 Fingerprint orientation data

Fingerprint matching is based on extracting a set of particular features, called *minutiae*, which uniquely define the fingerprint. These features are usually ridge endpoints or ridge bifurcation points that are saved along with their position and orientation. This means that prior to minutiae detection and extraction, the calculation of an orientation field is necessary.

For pictures of fingerprints this is just a special form of edge detection which can be done by calculating discrete derivatives for every pixel using a Sobel or Scharr operator. The ridges in the original fingerprint, however, are usually too thick, resulting in gradient values close to zero within the ridge and consequently ill-defined orientations. For that reason, firstly Zhang-Suen thinning algorithm [34] is used to obtain only the ridge skeleton for which the derivatives are then computed.

Depending on the quality and noise level of the picture, the computed orientation field can be very noisy itself, which is another application for the TV minimization. An example is provided in Figure 4.10.

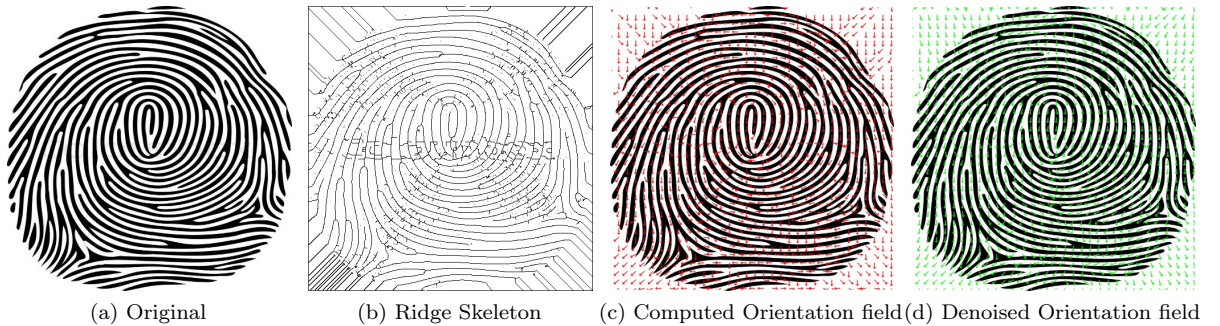


Figure 4.10: Denoising a orientation field from a fingerprint, orientations represented by  $\text{SO}(2)$  elements  
(a) Original fingerprint (a) Ridge skeleton computed using a thinning algorithm (c)  
Orientation field computed using Scharr derivatives (d) Denoised, IRLS with  $\lambda = 2.1$ , 5 IRLS steps,  
1 Newton steps per IRLS step

### 4.2.3 Reconstruction of a dense optical flow field

An optical flow is the pattern of apparent motion between two consecutive frames of a video sequence. This may be the result of either an actual movement of the depicted object or the result of a moving camera. Important applications are for example (abnormal) motion detection, crowd behavior analysis, surveillance, video compression or image segmentation.

A *dense* optical flow field can be interpreted as a vector field where each vector describes the displacement of a point from one frame to the next. If the set of points is restricted to only a few points of interest, a sparse feature set, it is called a *sparse* optical flow.

In the following example, a sparse feature set is used for tracking and flow computation in a short video sequence. The traffic scene was taken from a crowds/high density moving object data set provided by [7]. At first, the sparse optical flow is computed using the Lucas-Kanade algorithm [21] implemented in the OpenCV library.

For the set of tracked features  $\mathcal{F}_1 := \{F_i^{(1)}\}_{i=1}^{400} \subset \Omega \subset \mathbb{R}^2$  in the first frame, the algorithm tries to identify each feature in the second frame resulting in a set of identified features  $\mathcal{F}_2 := \{F_i^{(2)}\}_{i=1}^{N < 400} \subset \Omega \subset \mathbb{R}^2$  and corresponding displacement vectors  $\mathcal{V}_{12} := \{V_i \mid V_i = F_i^{(2)} - F_i^{(1)}\}_{i=1}^N$ .

To each pixel in the data an  $\text{SO}(2)$  element (of course the optimization could have also been

performed on  $S^1$ ) is assigned in the following way

$$\alpha_i = \arctan\left(\frac{V_i^y}{V_i^x}\right) \quad (4.3)$$

$$I(i, j) = \begin{cases} \begin{pmatrix} \cos \alpha_i & -\sin \alpha_i \\ \sin \alpha_i & \cos \alpha_i \end{pmatrix} & (i, j) \in \mathcal{F}_2 \\ 0 & \text{otherwise} \end{cases}. \quad (4.4)$$

Since reconstruction of the dense optical flow is the goal, this is an inpainting problem and scattered interpolation must be performed before running the algorithm. The result can be seen in Figure 4.11.

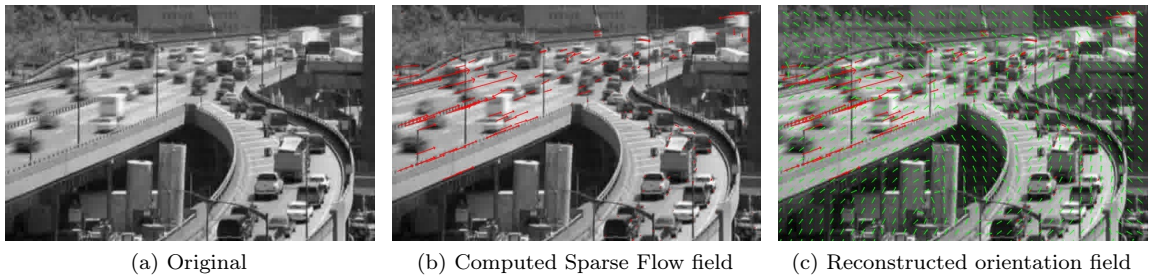


Figure 4.11: Reconstructing a dense flow from sparse feature tracking, orientations represented by  $SO(2)$  elements (a) Frame of original video scene (b) Sparse features tracked using Lucas-Kanade (c) Reconstructed, IRLS with  $\lambda = 0.05$ , 5 IRLS steps, 1 Newton step per IRLS step

There is also a more direct, variational approach for the calculation of the flow field which is also based on TV minimization but has a different fidelity term. This is one possibility for further extension of the library and is discussed in more detail in Section 5.2

### 4.3 SPD(3) image data

As in the case of  $SO(3)$ , the algorithms are first applied to synthetic data. It consists of approximately five homogeneous regions with large changes in the principal direction when moving from one region to another. These changes are the edges in the  $SPD(3)$  case. Second, and more challenging due to the large differences in mean diffusivity, the algorithms are applied to real 2D and 3D DT-MRI pictures.

#### 4.3.1 Synthetic data

For the construction of the synthetic  $SPD(3)$  image in Figure 4.12, let  $\Omega = \{1, \dots, n\}^2$  and define for every  $(i, j) \in \Omega$  a rotation axis

$$v = \begin{cases} (x, y, 2)^T, & x + y < 1 \\ (y, -x, 1)^T, & \text{else} \end{cases}, \quad (4.5)$$

where  $x = \frac{j}{n}$ ,  $y = \frac{i}{n}$  and a rotation angle

$$\alpha = \begin{cases} x + 2y, & x + y < 1 \\ y + 2x, & \text{else} \end{cases}. \quad (4.6)$$

Let  $R$  be the corresponding  $SO(3)$  element representing a rotation by  $\alpha$  and about  $v$ . Then define a diagonal matrix  $D = \text{diag}(x + 0.2, y + 0.2, 0.5)$  and assign the matrix  $A = R^T D R$  to the pixel. Noise is then added by taking the matrix logarithm of every pixel, adding Gaussian componentwise noise and applying the matrix exponential again.

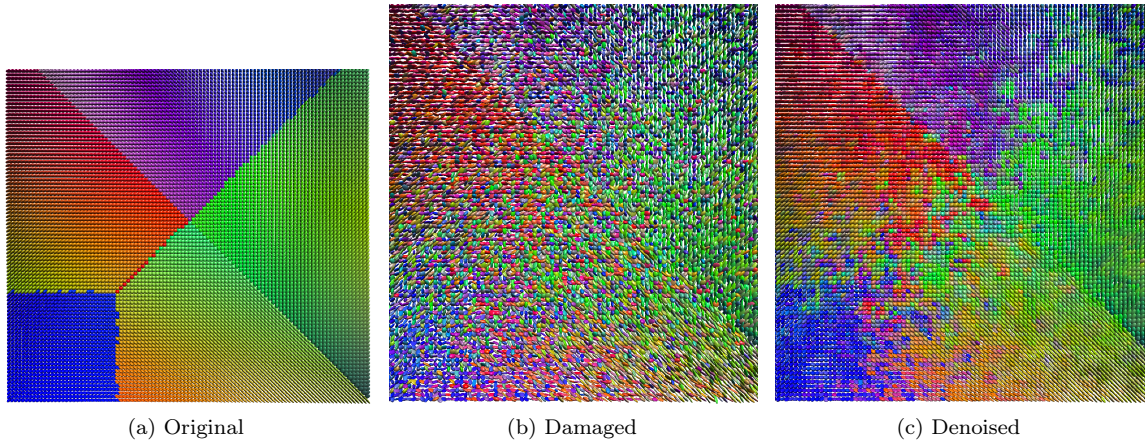


Figure 4.12: Denoising of synthetic SPD(3) picture (a) Original image: Synthetic, non-smooth SPD(3),  $100 \times 100$  px (b) Componentwise Gaussian noise with  $\mu = 0$  and  $\sigma = 0.2$  (c) Denoised, IRLS with  $\lambda = 0.7$ , 5 IRLS steps, 1 Newton step per IRLS

### 4.3.2 Diffusion Tensor Magnetic Resonance Imaging

Diffusion Tensor Magnetic Resonance Imaging (DT-MRI) is a medical imaging method which is able to non-invasively measure diffusion coefficients of water molecules in living biological tissues. DT-MRI goes beyond CT or normal MR imaging methods which are only able to provide a single intensity value per voxel. Since water molecules can move easier along, for example axons, connecting the neurons in the brain, than they can move across it, the resulting anisotropic diffusion pattern can provide a lot of information about the structure of the brain.

DTI data sets are usually calculated from a set of diffusion weighted magnetic resonance imaging (DW-MRI) pictures. The basic magnetic resonance imaging works by applying an external magnetic field along the  $z$ -axis such that the proton spins in the tissue align either parallel or anti-parallel to it while still precessing around the  $z$ -axis with the so-called Lamor frequency. An electromagnetic wave packet (HF-pulse) with that exact frequency leads to a collective state transition such that spin moments will be phase-synchronous before relaxing back to their original orientation with respect to the external field. The magnetic field created by having synchronized moments can be measured by a coil where an electric potential will be created. From the different relaxation times of different materials conclusions can be made about the structure of the tissue.

By applying an additional magnetic gradient field, the Lamor frequency of different layers of the probe can be modified such that only one layer of the material will resonate to the pulse. This provides an additional positional resolution of the imaging process.

The DTI image is finally computed using the *Stejskal-Tanner-equation* given by

$$A(\mathbf{g}) = A(0) \exp(-b\mathbf{g}^T \mathbf{D}\mathbf{g}) \quad (4.7)$$

where  $\mathbf{g}$  denotes the magnetic gradient field,  $A(\mathbf{g})$  the signal strength, and  $b$  some measurement related parameters. Solving this equation for  $\mathbf{D}$  finally leads to the desired  $SPD(3)$  matrix describing the diffusion coefficients and directions.

In Figure 4.13 the IRLS minimizer is applied to DTI data set provided by Barmpoutis [1]. In the picture, regions of high anisotropy, where the molecules are forced to diffuse in one preferred direction, can be clearly identified. The areas dominated mainly by green spheres correspond to approximately isotropic diffusion which means that there are no obstacles, like axons in the brain, in the immediate proximity of the water molecules.

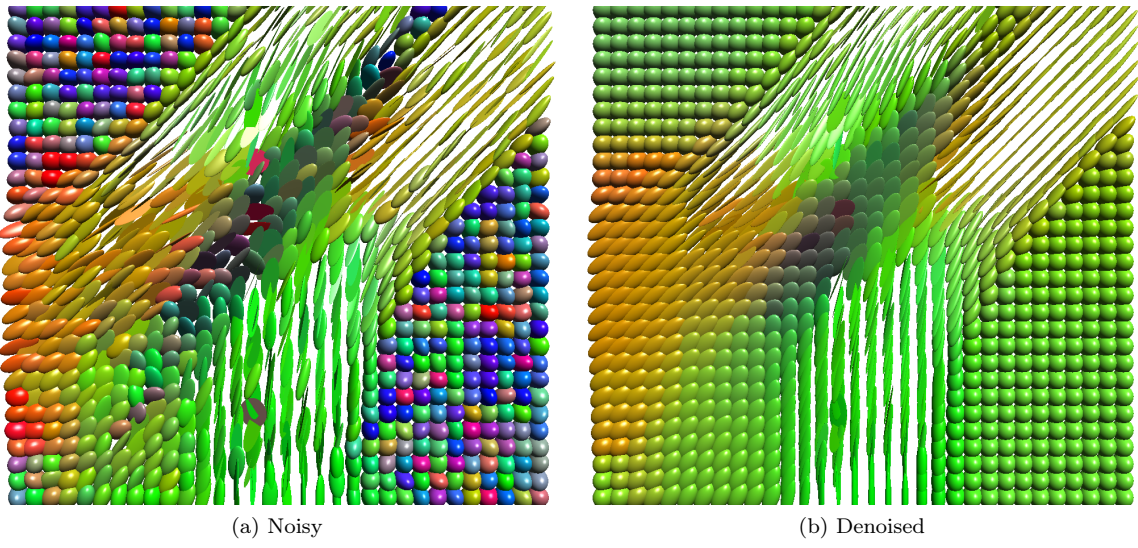


Figure 4.13: Denoising a DT-MRI image with pixel in SPD(3) **(a)** Original DTI data, 32x32 pixel  
**(b)** Denoised, IRLS with  $\lambda = 0.7$ , 5 IRLS steps, 1 newton steps per IRLS step

### 4.3.3 3D DT MRI data

Finally, in Figure 4.14 a 3D DTI image is depicted. Shown is a  $16 \times 16 \times 16$  cube from a human brain scan. The proximal point algorithm was used for denoising. The brain data set is a courtesy of Gordon Kindlmann at the Scientific Computing and Imaging Institute, University of Utah, and Andrew Alexander, W. M. Keck Laboratory for Functional Brain Imaging and Behavior, University of Wisconsin-Madison.

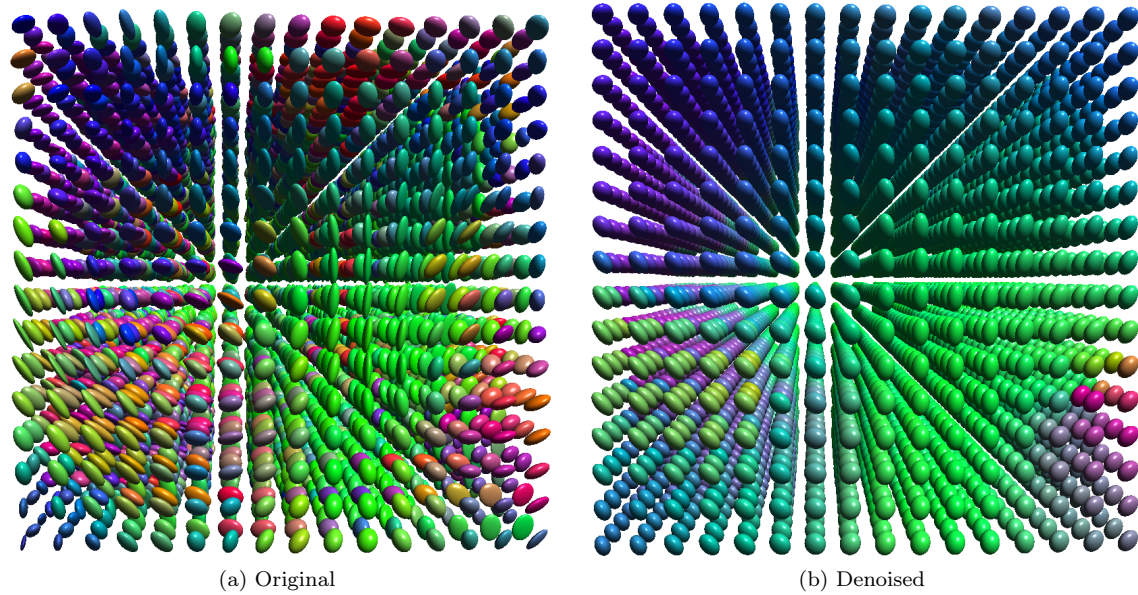


Figure 4.14: Denoising a 3D DT-MRI image with pixel in  $\text{SPD}(3)$  (a) Original,  $16 \times 16 \times 16$  pixel  
(b) Denoised, Proximal point with  $\lambda = 0.7$ , 50 PRPT steps

## 4.4 $Gr(3,1)$ image data

Grassmann manifold-valued data has a large number of applications, especially in the field of machine learning for tasks like face and shape recognition. This data can also be subject to noise which makes an application of TV minimization useful. Since example code comparing recognition rates for noisy and denoised data is beyond the scope of this thesis, a much simpler and more illustrative example was chosen.

Due to the fact that  $Gr(3,1) \simeq S^2$ , TV minimization over the Grassmann manifold can also be used to remove chromatic noise from pictures, completely analogous to the denoising over  $S^2$  considered earlier.

### 4.4.1 Chromaticity denoising

In the first example, shown in Figure 4.15, only the color part of the image will be denoised. Then, Figure 4.16 shows the minimization over the product manifold  $Gr(3,1) \times \mathbb{R}$ , using the same picture as in example 4.4.

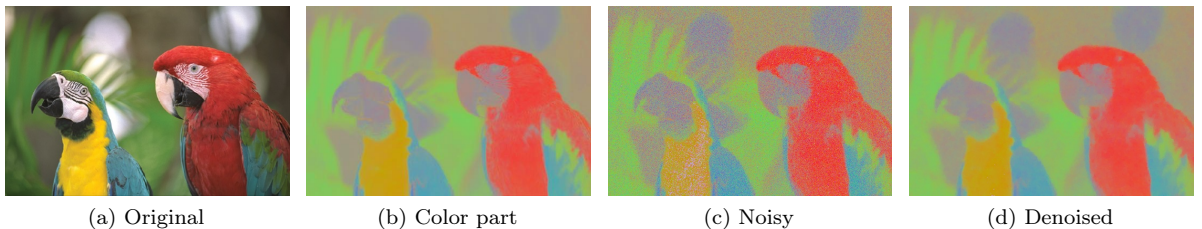


Figure 4.15: Denoising the color part of an image over the Grassmannian  $Gr(3,1)$  (a) Original image "Parrot.jpg",  $541 \times 361$  px, 8 bit color depth (b) Color part of image (c) Component-wise Gaussian noise  $\mu = 0$ ,  $\sigma = 0.1$  added (d) Denoised, IRLS with  $\lambda = 0.4$ , 5 IRLS steps, 1 newton steps per IRLS step

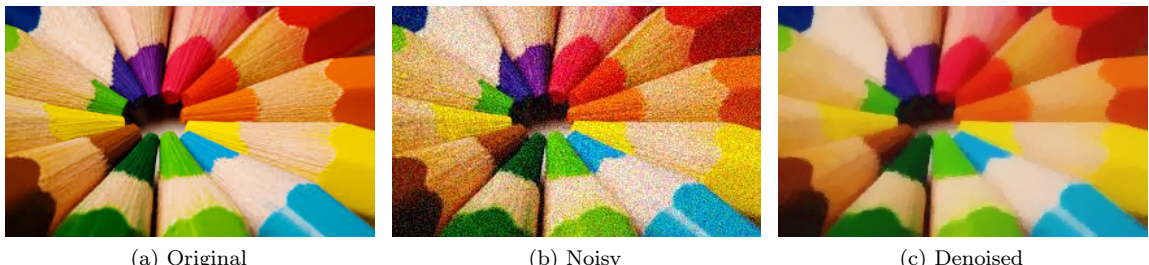


Figure 4.16: Denoising of a color image using the CBR color model over the manifold  $Gr(3,1) \times \mathbb{R}$  (a) Original image "Crayons.jpg",  $284 \times 177$  px, 8 bit color depth (b) Component-wise Gaussian noise  $\mu = 0$ ,  $\sigma = 0.1$  added (c) Denoised, IRLS with  $\lambda_{Gr(3,1)} = \lambda_{\mathbb{R}} = 0.1$ , 5 IRLS steps, 1 newton steps per IRLS step

## 4.5 Performance analysis of the library

In this section the performance hotspots of the library are analysed for the case of the IRLS minimizer. This is done using the Linux tool *perf* which monitors a variety of different performance metrics during the execution of a program, like CPU cycles, cache or branch misses. To identify the hotspots, where most of the computation is spent, the number of CPU cycles is usually the

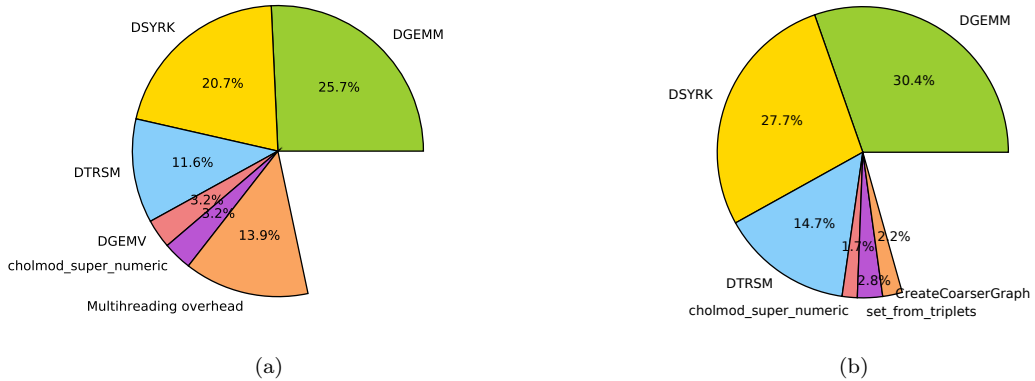
most suitable metric. In the last part also the time complexity of the algorithm is measured.

Concerning the computational complexity of operations performed on single pixels, the Euclidean manifold is certainly the least demanding, because exponential and logarithm map are addition and subtraction and the second derivative of the distance function is just two times the identity matrix. At the other end of the spectrum is the *SPD* manifold where computations usually involve multiple matrix multiplications, exponentials, logarithms and derivatives thereof. For the analysis, metrics and running times for these two representatives are compared for different image sizes.

#### 4.5.1 Profiling

For the Euclidean manifold the "Lena" and "Mathematicians" pictures, already considered in the example above, are used. Minimization in the first case takes approximately 9 seconds and 270 seconds in the second case. The data is shown in Table 4.1 where the first column denotes the percentage of CPU cycles spent in the routine specified in the second column while the last column denotes the (external) library to which it belongs. Only the top six routines are shown since the individual share of the others was in most cases less than 1 %.

In both cases computation is dominated by the Basic Linear Algebra Subprograms (BLAS) Library. Those in turn are called by the CHOLMOD library which solves the sparse linear system using Cholesky factorization. The only contribution that does not belong to the linear system is the multi-threading overhead from the OpenMP (OMP) library in the smaller picture. For the increased system size, however, the overhead becomes negligibly small such that for both problem sizes more than two thirds of the total computation time is used for solving the linear system. For the larger picture this share even grows to more than 75% and can be expected to do so for yet larger images.



Share	Routine	Library	Share	Routine	Library
25.73	DGEMM(matrix matrix multiply)	BLAS	30.37	DGEMM(matrix matrix multiply)	BLAS
20.71	DSYRK(symmetric rank-k update)	BLAS	27.70	DSYRK(symmetric rank-k update)	BLAS
13.86	Multithreading overhead	OMP	14.65	DTRSM(solve triangular system)	BLAS
11.57	DTRSM(solve triangular system)	BLAS	2.79	set_rom_triplets(sparse initialization)	Eigen
3.23	DGEMV(matrix vector multiply)	BLAS	2.18	CreateCoarserGraph	METIS
3.22	cholmod_super_numeric	CHOLMOD	1.68	cholmod_super_numeric	CHOLMOD

(a) 361 × 361

(b) 1280 × 1024

Table 4.1: Share of total CPU cycles for IRLS minimization over  $M = \mathbb{R}^3$  (a)"Lena.jpg", 361 × 361 pixel (b)"Mathematicians.jpg", 1280 × 1024 pixel

For the *SPD*( $n$ ) manifold the situation, shown in Table 4.2 and Table 4.3, looks a bit different at

first. For the smallest problem size of  $30 \times 30$  pixels, there are no dominating parts. The largest contribution is from multi-threading, which is to be expected for such a small picture and which consequently vanishes for larger images. The next important routine is MTVMTL's implementation of the matrix logarithm Fréchet derivative, while the remaining Eigen routines in the list are auxiliary functions for solving triangular matrix functions. These are needed for the computation of matrix square roots, logarithms and of course also their Fréchet derivatives. With increasing problem size, the BLAS routines seem to move to the top of the list, even though their share only amounts to a fifth of all CPU cycles for the  $300 \times 300$  pixel image.

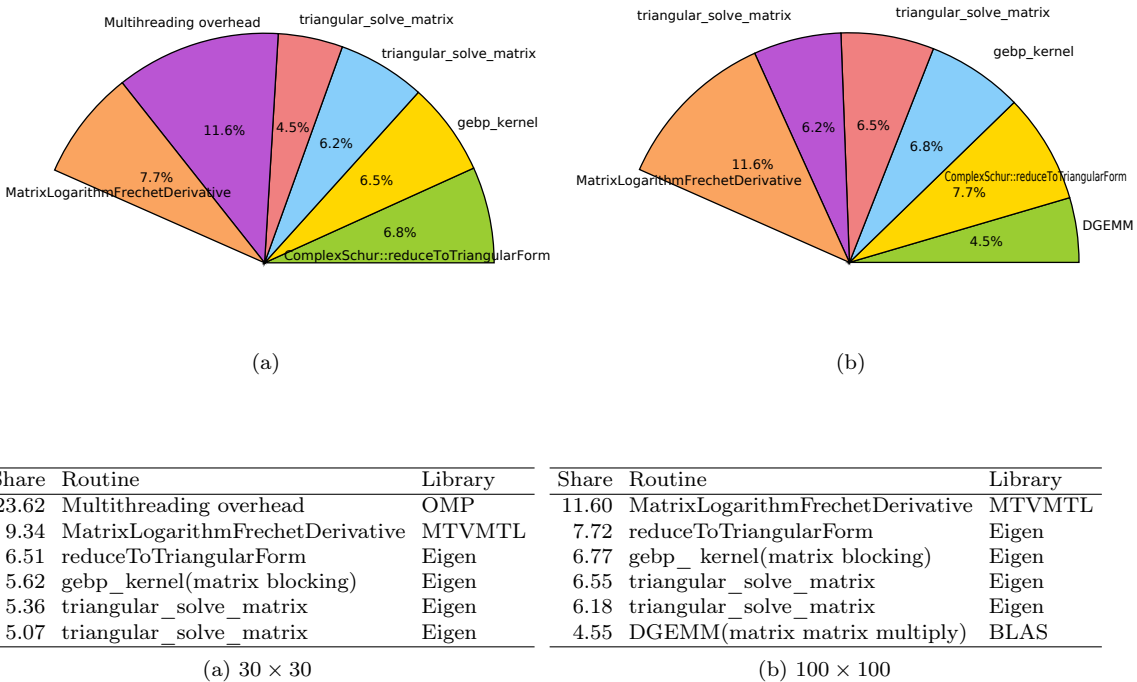


Table 4.2: Share of total CPU cycles for IRLS minimization over  $M = SPD(3)$  (a) Synthetic  $SPD(3)$ ,  $30 \times 30$  (b) Synthetic  $SPD(3)$ ,  $100 \times 100$

It can be concluded that solving the linear system is the most performance relevant aspect of the IRLS minimizer. The share is even higher for  $SO(n)$  and  $S^n$ , where the SuperLU library is used, since the corresponding sparse Hessian is not positive definite, resulting in a further increased operations count. If a good preconditioner is found, iterative solvers might speed up the computation, the standard diagonal and incomplete LU preconditioner provided by the Eigen library, however, performed worse than the direct solvers from the SparseSuite library collection. Finally, for the matrix-valued manifolds, the implementation of the Fréchet derivative could potentially be improved.

#### 4.5.2 Time complexity

Next, the measurements of the time complexity obtained for the Euclidean  $\mathbb{R}^3$  and  $SPD(3)$  need to be discussed. For both cases subquadratic time complexities can be observed over the considered input size range, which was limited only due to the available RAM on the test platform. This deviation from the theoretical expected (quasi-)linearity can eventually be explained by memory access costs.

Handling large amounts of data, which in the above tests are in the GB range, naturally leads to additional cost for memory access. Memory is hierarchically structured with the CPU caches having the lowest access time but also the smallest size, whereas the RAM is comparably huge but

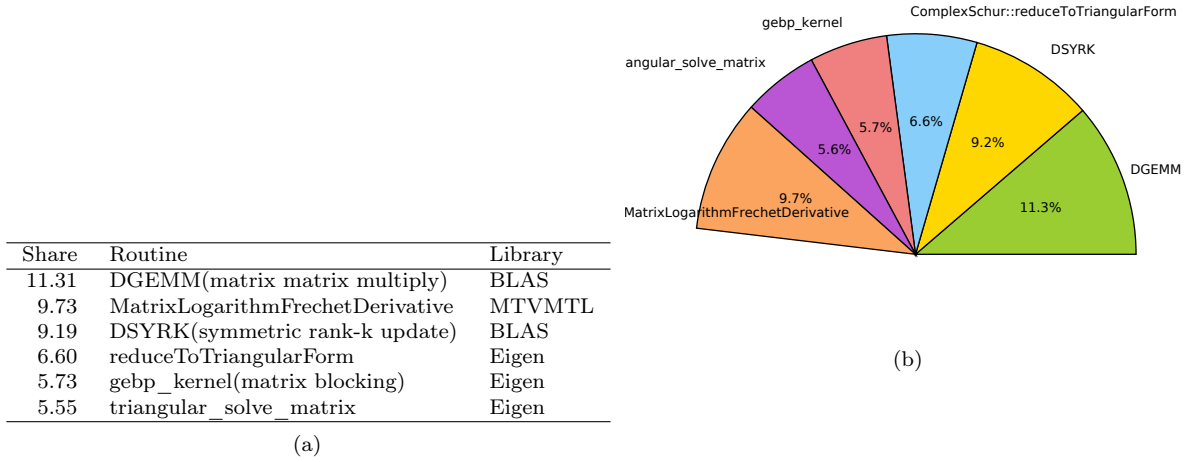


Table 4.3: Share of total CPU cycles for IRLS minimization of synthetic  $SPD(3)$ ,  $300 \times 300$  pixel,  $M = SPD(3)$

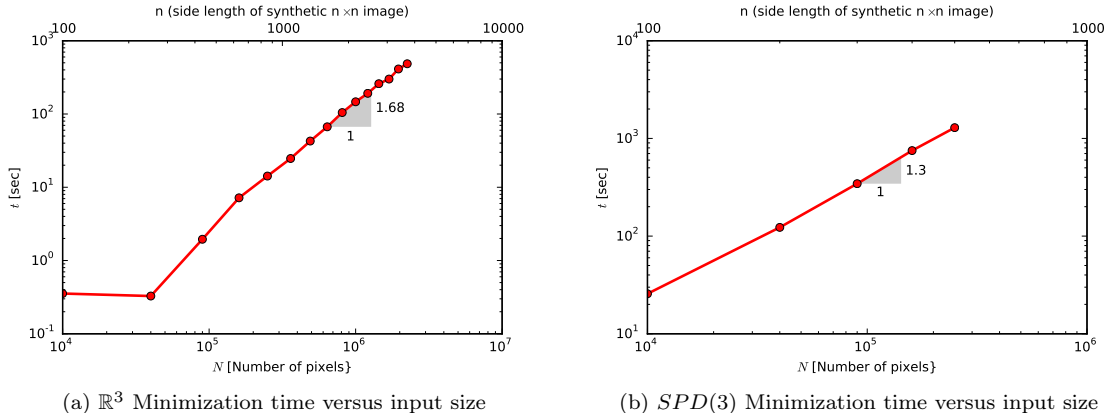


Figure 4.17: Time complexity for the IRLS  $\mathbb{R}^3$  and  $SPD(3)$ . In both cases, minimization was performed using 5 IRLS steps and 1 Newton step per reweighting (a) Denoising of a synthetic RGB picture of size  $n \times n$  with  $n = 100, 200, \dots, 1500$  (b) Denoising of a synthetic  $SPD(3)$  picture of size  $n \times n$  with  $n = 100, 200, \dots, 500$

has a much larger access time. At the bottom of the hierarchy is swap space on the hard drive. The cost of a so-called page-fault, which happens when a program tries to access a memory location that is not loaded into the main memory, can amount to more than 1000 CPU cycles. Since with increasing memory utilization the probability for page faults may also increase, performance will consequently decrease.

It is remarkable, however, that the complexity for the SPD manifold is lower than for Euclidean space. Taking into account the analysis of the previous section, where it was illustrated that most time is spent solving the linear system, a possible explanation might be that for the SPD manifold the share of computational effort of solving the linear system is smaller relative to the remaining operations, like calculation of the derivatives for example. Assuming that the latter perform indeed quasi-linear, this would suggest that, on the other hand, solving the system must have a complexity larger than  $\mathcal{O}(\text{NNZ}(HJ)) = \mathcal{O}(N)$ .

Considering above remarks on the effects of memory access speed, this claim can be further

supported by looking at other performance metrics like cache-misses and page-faults, where the BLAS routines are again at the top of the listings. The measurement results for this metrics can be found in Appendix C.

## 4.6 Comparison IRLS and Proximal Point minimizers

To make a comparison with the tests performed in [16], using the original Matlab implementation, to a certain degree possible, the same set of test images (Figure 4.18) was chosen but additionally also some larger versions of the pictures for the more interesting case of the matrix manifolds  $SO(3)$  and  $SPD(3)$ . For the Grassmannian  $Gr(3, 1)$  the same picture as for  $S^2$  is used. Both, the IRLS and the proximal point minimizers are implemented using the same manifold classes and both utilize the same pixel-wise parallelization techniques such that there is no obvious bias in this comparison.

The synthetic images are created using the formulas already described in the examples above. To each picture component-wise Gaussian noise with zero mean and standard deviation of  $\sigma = 0.2$  is added. With that noise level no smoothing is needed for the IRLS algorithm to converge. For each picture the value of the functional after each iteration and the error relative to an approximate minimizer  $u^*$  is computed. The minimizer is obtained using the IRLS algorithm with  $\lambda = 0.2$ , 20 IRLS steps and one newton step per reweighting. This error is defined as

$$e^{(k)} = \sum_{i,j} d^2(u_{ij}^{(k)}, u_{ij}^*) \quad (4.8)$$

where  $d^2(\cdot, \cdot)$  denotes the squared Riemannian distance function of the appropriate manifold. For the iterations itself 15 iterations for IRLS and 500(250 for  $Gr(3, 1)$ ) for proximal point with the sequence  $\mu_k = 3k^{-0.95}$  (see [33] for details on this sequence) are used for all experiments.

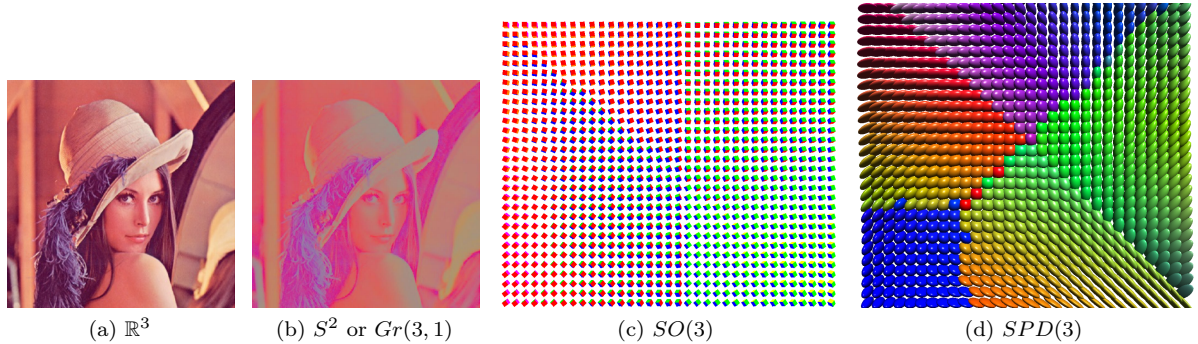


Figure 4.18: Test images for the IRLS & PRPT comparison (a) "Lena.jpg",  $361 \times 361$  px,  $\mathbb{R}^3$ -valued (b) Chromaticity part of "Lena.jpg",  $S^2/Gr(3, 1)$ -valued (c) Synthetic  $30 \times 30$  and  $100 \times 100$  image,  $SO(3)$ -valued (d) Synthetic  $30 \times 30$  and  $100 \times 100$  image,  $SPD(3)$ -valued

Figure 4.19 shows the results for Euclidean space  $\mathbb{R}^3$  and the sphere  $S^2$ . IRLS needs only five iterations where proximal point needs more than 200 but nevertheless proximal wins in terms of speed. This result can be interpreted with respect to the performance analysis conducted in the previous section. Most manifold quantities can be computed using only addition and subtraction. This includes the geodesic interpolation that proximal point has to perform in every direction as well as the computation of derivatives for IRLS. The effort of doing these two task seems intuitively to be similar. At the end of that process, however, proximal point only has to compute simple arithmetic means while IRLS has to solve the sparse system which was shown to be the dominant part of the computation and is thus probably more time consuming than the averaging procedure. For  $S^2$ , in comparison, one can already see IRLS catching up.

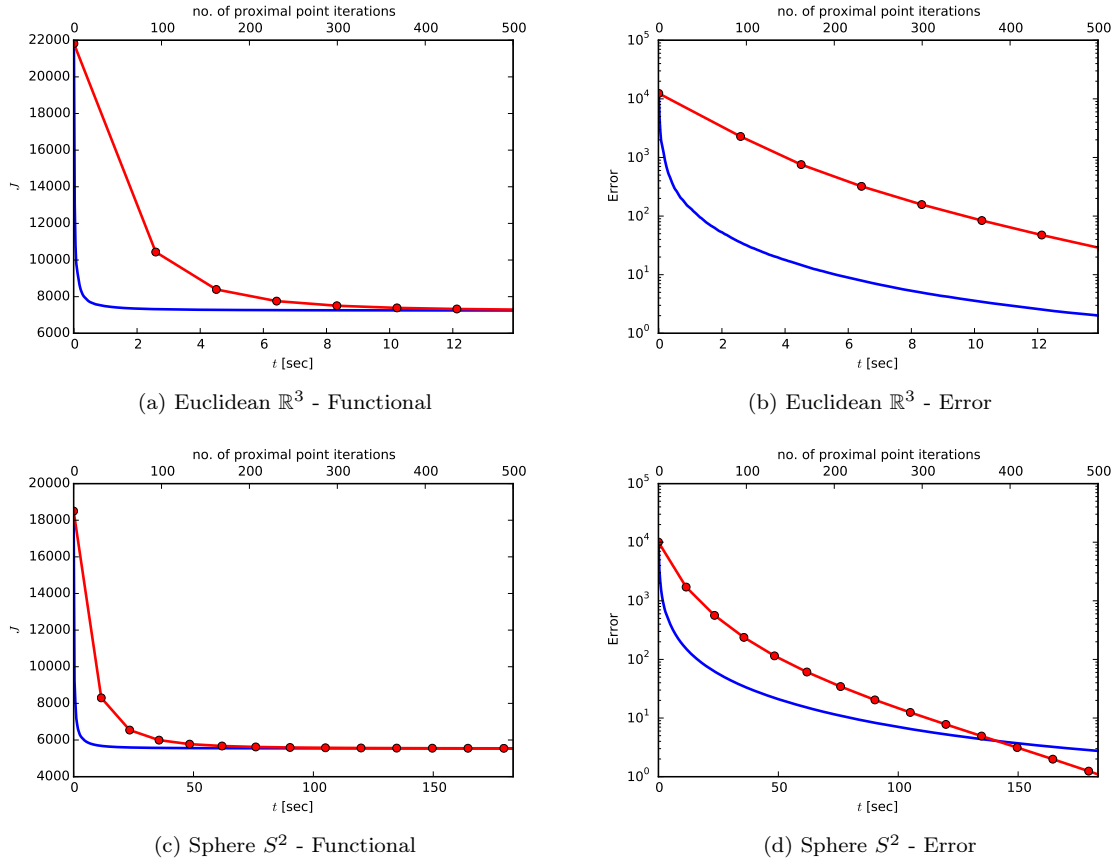


Figure 4.19: Comparison of functional values and errors for IRLS and PRPT minimizers. The red circles correspond to IRLS iterations while the line without any markers belongs to the proximal point iterations. (a) Functional values for "Lena" minimized over  $\mathbb{R}^3$  (b) Errors relative to minimizer for "Lena" (c) Functional values for color part of "Lena" minimized over  $S^2$  (d) Errors relative to minimizer for color part "Lena"

For  $SO(3)$ , shown in 4.20, the difference again becomes much smaller, with both plots being very close and coinciding already after the second iteration. In terms of the error IRLS even surpasses proximal point after 4 iterations.

Next, in the case of  $SPD(3)$ , shown in 4.21, except for the error, IRLS falls back to the niveau of  $S^2$ . One reason for that might be the particularly complicated form of the second derivative of the squared distance function. This could be eventually optimized by improving the implementation of the Fréchet derivative. At this time it is based on the computation of a complex Schur decomposition which then, in turn, needs complex arithmetic. Switching to a block-based, but real Schur decomposition might provide an additional speed-up.

Finally, Figure 4.22 shows the results for the Grassmannian manifold  $Gr(3,1)$ . Here IRLS performs considerably faster than the proximal point algorithm. While for all the previous manifolds computation of the exponential and logarithm map was very easy, in the case of the Grassmannian, a singular value decomposition must be performed for every evaluation and the logarithm even requires the solution of a small linear system before the decomposition. Computation of the derivatives for IRLS, on the other hand is comparably easy, with only matrix-matrix multiplications and Kronecker products involved. Since the proximal point algorithm is mainly based on exponential and logarithm map evaluations, solving the sparse linear system is faster here.

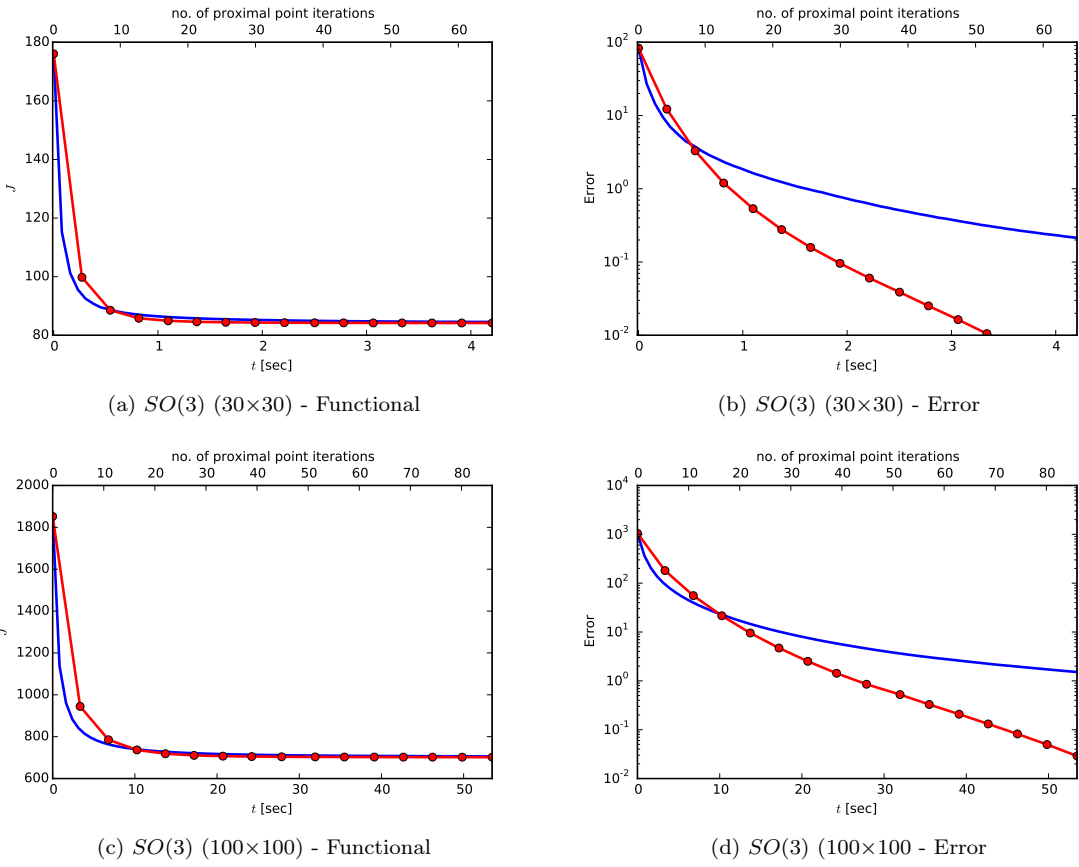


Figure 4.20:  $SO(3)$ : Comparison of functional value and errors for IRLS and PRPT minimizers. The red circles correspond to IRLS iterations while the line without any markers belongs to the proximal point iterations. (a) Functional values for synthetic  $30 \times 30$   $SO(3)$  (b) Errors relative to minimizer for synthetic  $30 \times 30$   $SO(3)$  (c) Functional values for synthetic  $100 \times 100$   $SO(3)$  (d) Errors relative to minimizer synthetic  $100 \times 100$   $SO(3)$

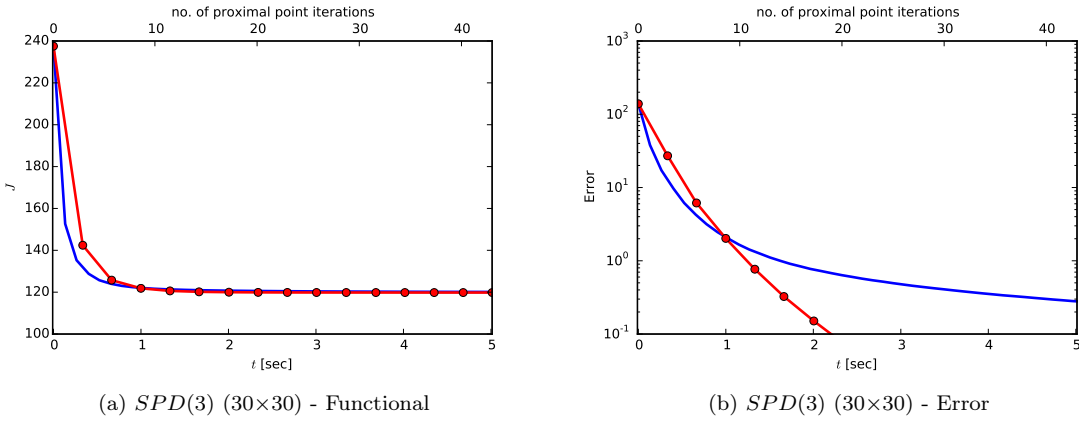


Figure 4.21:  $SPD(3)$ : Comparison of functional value and errors for IRLS and PRPT minimizers. The red circles correspond to IRLS iterations while the line without any markers belongs to the proximal point iterations. (a) Functional values for synthetic  $30 \times 30$   $SPD(3)$  image (b) Error relative to minimizer for synthetic  $30 \times 30$   $SPD(3)$  image

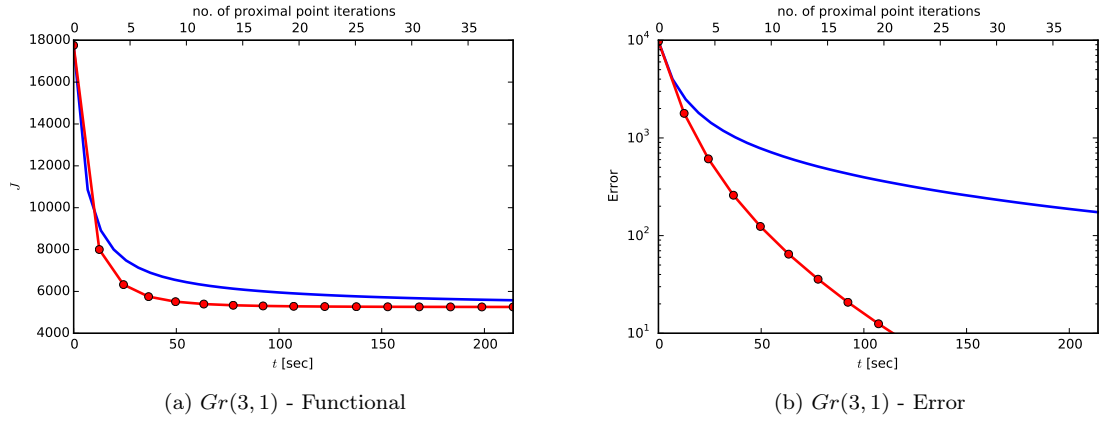


Figure 4.22:  $Gr(3,1)$ : Comparison of functional value and errors for IRLS and PRPT minimizers. The red circles correspond to IRLS iterations while the line without any markers belongs to the proximal point iterations. (a) Functional values for color part of "Lena" minimized over  $Gr(3,1)$  (b) Errors relative to minimizer for color part "Lena"

## 4.7 Sensitivity to variations of the original data

In this section a numerical experiment is performed to see how changes of the noisy original picture influence the global solution of TV minimization. For that purpose only the brightness part of the Lena picture is considered. In this grayscale image a single non-zero pixel is chosen, far enough in the inside of the picture. This pixel is set to zero, i.e. black color. This leads to two different original pictures

$$u_0, \hat{u}_0 : \Omega \rightarrow \mathbb{R} \quad (4.9)$$

$$(\hat{u}_0)_{ij} = \begin{cases} 0, & \text{if } i = i_0 := 100, j = j_0 := 100 \\ (u_0)_{ij}, & \text{else} \end{cases}. \quad (4.10)$$

Then, for the original  $u_0$  and the modified image  $\hat{u}_0$  an IRLS minimization with  $\lambda = 0.1$ , 5 iterations and one Newton step per reweighting is performed to compare the two the solutions  $u$  and  $\hat{u}$ . Taking the absolute differences  $e_{ij} = |u_{ij} - \hat{u}_{ij}|$  between the solutions leads to the error cone shown in Figure 4.23a. This already suggests that the error caused by changing the original data decays exponentially with distance  $r = \sqrt{(i - i_0)^2 + (j - j_0)^2}$ .

After fitting a cone to the data, which is shown in 4.23b one finds that the aperture half-angle corresponds to a slope of  $c = 1.075$  such that the error will decay as

$$e_{ij} \propto e^{-cr}. \quad (4.11)$$

The most important conclusion is that a pixel in the global minimizer depends practically only on a local neighborhood of that pixel in the original picture, not on pixels far away from that neighborhood. Possible applications of this are discussed in Section 5.3.

Of course these findings should be verified analytically by providing sufficiently precise error bounds, which is, however, unfortunately out of the scope of this thesis.

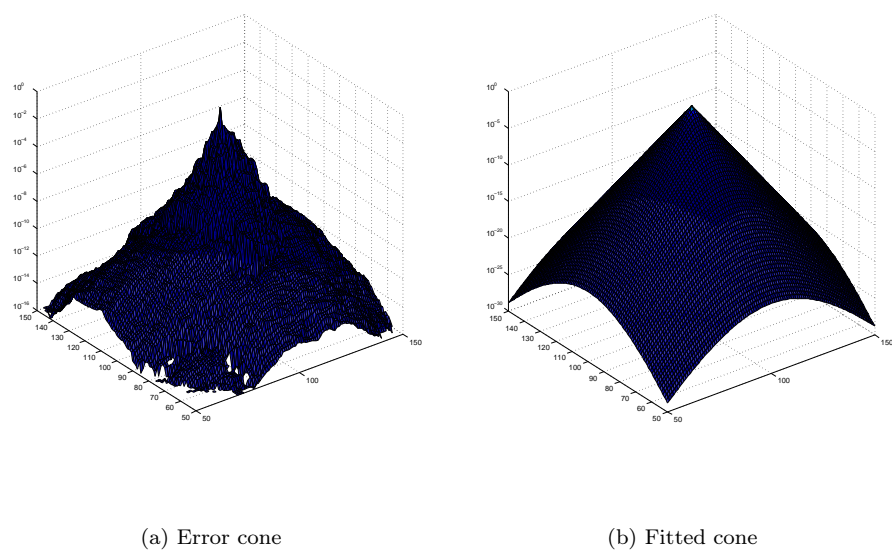


Figure 4.23: Sensitivity to change in original data (a) Logarithmic plot of absolute differences  $e_{ij} = |u_{ij} - \hat{u}_{ij}|$  (b) Cone fitted to the data, resulting in aperture half-angle of  $\alpha = 0.8213$

# Chapter 5

## Conclusion and Outlook

### 5.1 Summary

In this thesis a very versatile, multi-threaded C++ template library for TV minimization of manifold-valued data is introduced, which extends the original Matlab prototype in a variety of directions. This includes shared memory and SIMD parallelization for IRLS and proximal point algorithms, 3D images, the Grassmann manifold as well as supporting methods for numerical matrix function derivative computations and OpenGL visualization methods.

The theoretical background provides some semi-analytic expressions for the derivatives of the squared distance functions using Kronecker products, which allows a compact and readable implementation. Furthermore, a short overview about the relevant Grassmann manifold theory is given.

The third chapter is a high level documentation of the library and its structure and underlying concepts. It gives more insights on the software engineering and high performance computing point of view on this thesis and also contains some basic tutorials on how to use or even extend the library.

Finally, the library's capabilities are demonstrated on many different applications like standard grayscale and color images, medical DT-MRI data, synthetic  $SPD(3)$  and  $SO(3)$  data but also examples based on real applications like image orientation maps and optical flow computation. Aside from these more colorful demonstrations also a performance analysis of the library is done to investigate performance bottlenecks of the IRLS minimizer. As main result from this analysis the solution of the sparse linear system is identified as the most performance relevant component in the process. This suggests that the sparse solver do not scale (quasi-)linearly. But also the implementation of the Matrix logarithm Fréchet derivative has some influence and has potential for further optimization.

It is consequently found that IRLS performs slower for Euclidean space and the sphere and comparable for  $SO(3)$  and  $SPD(3)$ , compared to an also parallelized proximal point algorithm. IRLS is faster for the case of the Grassmannian, due the proximal point algorithms intensive use of computationally expensive exponential and logarithm maps. Lastly, in the course of identifying optimization opportunities, the sensitivity of the computed solution with respect to variations of the original data is investigated. It can be concluded that the resulting error in the solution is locally confined to a neighborhood around the varied pixel in the original and decays exponentially with the distance from the varied pixel. A possibility for an extension of the library exploiting this locality of the error is discussed in the last Section 5.3.

## 5.2 Extensions and improvements

At last, some suggestions for the extension and optimization of the library are presented. The first part is concerned with performance-relevant changes while the second and third parts focus on new features.

### 5.2.1 Performance

Since the solution of the sparse linear system is the most performance critical component of the algorithm, new solution methods should be tested. In particular, iterative methods could perform better if a good preconditioner can be found.

By making use of the special block-band structure of the Hessian, the MTVMTL implementation avoids the temporary block diagonal matrix, containing the tangent space basis transformation, that was used in the Matlab prototype. The tangent space transformations can instead be applied directly to the pixels of the derivative containers. In a similar manner, it might also be possible to make the algorithm completely matrix-free by implementing a matrix-vector multiplication function for the Hessian matrix, that can be used by an iterative solver. This might save a lot of memory as well as computation time and bring the algorithm closer to the linear complexity regime.

### 5.2.2 Manifolds and minimizers

The first thing that can easily be extended is the support for additional manifolds. Possibilities are, for instance, the Stiefel manifold that was briefly introduced in section 2.4.5 or an alternative implementation of the  $SPD(n)$  manifold using the Log-Euclidean metric based on [8].

Also new minimizers could be added. It would be straightforward to utilize the gradient evaluation function already implemented in the functional to add some gradient descent based algorithm and compare again with IRLS-Newton and proximal point. For new functionals a more detailed suggestion is provided in the next Section.

### 5.2.3 Functionals

So far isotropic and anisotropic first order TV functionals are implemented in the library. Extensions can be made with respect to the TV part or the fidelity part of the functional. For the TV part this means to also include a second order TV term  $\mu \int_{\omega} |\nabla^2 u| dx$  in the functional. This prevents the formation of numerical artifacts like the so-called staircasing effects, that might occur in first order TV. Of course also higher orders than second can be added to the functional. As long as also methods for the evaluation of the functionals gradient and Hessian are provided, the IRLS minimizer class will work without any changes.

The second possibility is the addition of new or different fidelity terms. The purpose of the fidelity term during the minimization is to penalize a TV regularization that moves too far away from the original picture. However, one can also utilize it for a direct calculation of a dense optical flow field, for example. This was also done in the application shown in 4.2.3 but it must be noted that the procedure in the example to computation of the dense flow was rather complicated and indirect.

For the direct TV approach, as presented in [32], consider a 2D video sequence  $I : \Omega \times [0, T] \rightarrow \mathbb{R}$ . Let now  $u : \Omega \rightarrow \mathbb{R}^2$  denote the displacement vector of the pixel  $x \in \Omega$ . The functional is then given by

$$J(u) = \int_{\Omega} \left| \frac{\partial I}{\partial t} + \nabla I \cdot u \right| dx + \lambda TV(u), \quad (5.1)$$

where the first term is the new data term, which implements the so-called optical flow constraint that could be interpreted as a continuity equation for pixels. Finally, as Lefevre and Baillet show in [19], the functional can be generalized also to flows on some classes of manifolds.

### 5.3 Recursive computation on subdomains

From the numerical experiment in Section 4.7 it can be concluded that a local neighborhood of the original picture only affects the form of the minimizer in its immediate neighborhood. The magnitude of the variation in the minimizer due to the variation of a single pixel in the original data seems to decay exponentially with the distance from that pixel.

This could in principle be exploited by dividing the image into subdomains with a specific small overlap, determined by the error boundaries, and solve each of the smaller subproblems individually. Depending on the size of the necessary overlap this could also be employed recursively until a minimal subimage size is reached. Then, after all subproblems are solved the subpictures are recombined just by cropping all overlapping regions to arrive at the global solution. As a final example, an extended version of the Lena picture is split in the middle with 50px overlap, as shown in Figure 5.1.

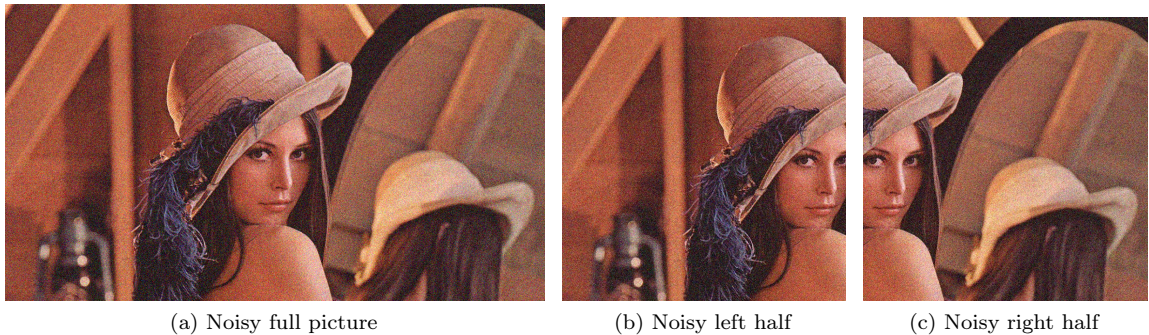


Figure 5.1: Splitting of the Lena picture into two domains (a) Original image "Lena.jpg",  $1000 \times 550$  px, 8 bit color depth (b) Left half,  $550 \times 550$  (c) Right half  $550 \times 550$

Next, the algorithm is applied to the the full picture, which takes 72 seconds, as well as to the two halves, which takes 33 seconds for each run. Then the two halves are recombined after cropping away the overlap. The results, shown in Figure 5.2, look promising. Of course, at this point some more detailed numerical error analysis should be performed but just from visual inspection there are no serious problems, like a visible brightness or color gradient for example, evident.

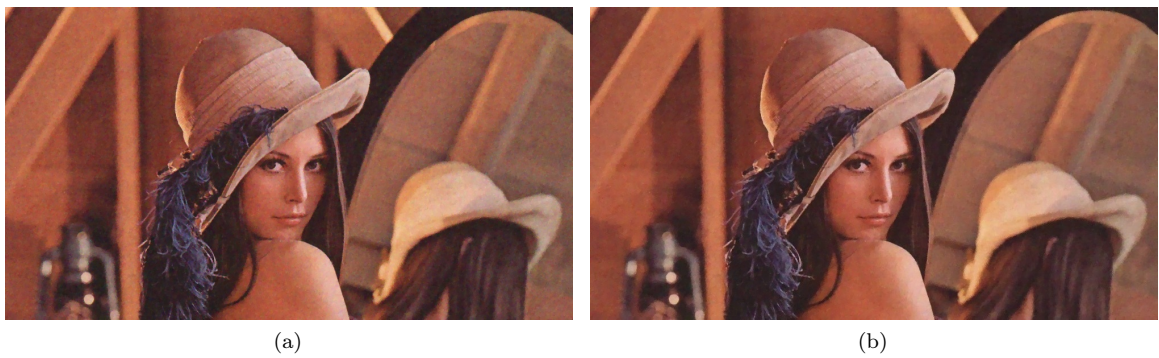


Figure 5.2: Comparison between the denoising over the full domain and denoising over two subdomains (a) Denoised full picture (b) Recombined, denoised picture halves

The advantages of this procedure are firstly, that even though there is some overhead from this procedure, a collection of smaller subproblems can be usually solved faster than one big problem and has a lower memory consumption. The speed up in the above example is not very large (66 versus 72 seconds), which is also to be expected from the subquadratic time complexity measured

in Section 4.5.2. Nevertheless, the main point is not about the speed up of serial-solving the subproblems but the lower memory demand allowing yet larger images to be processed.

Secondly, this splitting scheme can also be used to introduce an additional layer of parallelism in the form of distributed memory, many core parallelization. Each subproblem can be assigned to a different node that in turn locally applies multi-threading. By building such a distributed computing architecture on top of the solver, a significant speed up can be reached, because except from splitting and recombination there is no need for communication between the nodes during the TV minimization.

# Acknowledgements

I would like to express my sincere gratitude to Professor Dr. Philipp Grohs and to Markus Sprecher for the very interesting topic in the intersection of differential geometry, numerical analysis and software engineering I was permitted to work on in my thesis and for their support and guidance during the writing of this thesis.

I am especially indebted to Markus Sprecher for his extraordinary good supervision, commitment and uncountably many helpful comments and explanations. It was a pleasure working with and next to him and I would like to thank him also for many interesting discussions.

Furthermore, I would like to thank Günter and Angelika Höhlein for proofreading and valuable comments on style and structure.

Lastly, I would like to thank my girlfriend Luzia and my family for their continuous support and encouragement throughout my whole studies.

# Appendix A

## Listings

In this appendix full listings for the examples in the tutorial chapter are provided

Listing A.1: ./listings/tvmin\_test.cpp

```
1 #include <iostream>
2 #include <string>
3 #include <opencv2/highgui/highgui.hpp>
4
5 #include <mtvmtl/core/algo_traits.hpp>
6 #include <mtvmtl/core/data.hpp>
7 #include <mtvmtl/core/functional.hpp>
8 #include <mtvmtl/core/tvmin.hpp>
9
10 #include <vpp/vpp.hh>
11 #include <vpp/utils/opencv_bridge.hh>
12
13 using namespace mtvmtl;
14
15 typedef Manifold< EUCLIDIAN, 3 > mf_t;
16 typedef Data< mf_t, 2> data_t;
17 typedef Functional< FIRSTORDER, ISO, mf_t, data_t> func_t;
18 typedef TV_Minimizer< IRLS, func_t, mf_t, data_t, OMP > tvmin_t;
19
20
21 void DisplayImage(const char* wname, const data_t::storage_type& img, vpp::~
...image2d<vpp::uchar3>& out){
22     cv::namedWindow( wname, cv::WINDOW_NORMAL );
23
24     // Convert Picture of double to uchar
25     vpp::image2d<vpp::uchar3> vucharimg(img.domain());
26     vpp::pixel_wise(vucharimg, img) | [] (auto& i, auto& n) {
27         mf_t::value_type v = n * (double) std::numeric_limits<unsigned char>~
...>::max();
28         vpp::uchar3 vu = vpp::uchar3::Zero();
29         vu[0]=(unsigned char) v[2];
30         vu[1]=(unsigned char) v[1];
31         vu[2]=(unsigned char) v[0];
32         i = vu;
33     };
34
35     cv::imshow( wname, vpp::to_opencv(vucharimg));
36
37     out = vucharimg;
38     cv::waitKey(0);
39 }
40
41
42 int main(int argc, const char *argv[])
43 {
44 }
```

```

46   if (argc < 2){
47     std::cerr << "Usage : " << argv[0] << " image [lambda]" << std::endl;
48     return 1;
49   }
50
51   double lam=0.1;
52
53   if(argc==3)
54     lam=atof(argv[2]);
55
56   data_t myData=data_t();
57   myData.rgb_imread(argv[1]);
58
59   func_t myFunc(lam, myData);
60   myFunc.seteps2(1e-10);
61
62   tvmin_t myTVMMin(myFunc, myData);
63
64   vpp::image2d<vpp::uchar3> img;
65
66   std::string fname(argv[1]);
67
68   std::cout << "Smoothen picture to obtain initial state for Newton <
69   - iteration..." << std::endl;
70   myTVMMin.smoothening(5);
71   DisplayImage("Smoothened", myData.img_, img);
72   cv::imwrite("smoothened_" + fname, to_opencv(img));
73
74   std::cout << "Start TV minimization..." << std::endl;
75   myTVMMin.minimize();
76
77   DisplayImage("Denoised", myData.img_, img);
78   cv::imwrite("denoised_" + fname, to_opencv(img));
79
80   return 0;
81 }
```

---

Linear vectorial TV minimization

Listing A.2: ./listings/colorization\_test.cpp

---

```

1 #include <iostream>
2 #include <string>
3 #include <cmath>
4
5 #include <opencv2/highgui/highgui.hpp>
6
7 #include <mtvmtl/core/algo_traits.hpp>
8 #include <mtvmtl/core/data.hpp>
9 #include <mtvmtl/core/functional.hpp>
10 #include <mtvmtl/core/tvmin.hpp>
11
12 #include <vpp/vpp.hh>
13 #include <vpp/utils/opencv_bridge.hpp>
14
15
16
17 using namespace tvmtl;
18 typedef Manifold< SPHERE, 3 > spheremf_t;
19 typedef Manifold< EUCLIDIAN, 1 > eucmf_t;
20
21 typedef Data< spheremf_t, 2> chroma_t;
22 typedef Data< eucmf_t, 2> bright_t;
23
24 typedef Functional<FIRSTORDER, ISO, spheremf_t, chroma_t> cfunc_t;
25 typedef Functional<FIRSTORDER, ISO, eucmf_t, bright_t> bfunc_t;
26
27 typedef TV_Minimizer< IRLS, cfunc_t, spheremf_t, chroma_t, OMP > ctvmin_t;
28 typedef TV_Minimizer< IRLS, bfunc_t, eucmf_t, bright_t, OMP > btvmin_t;
29
```

```

30
31 void removeColor(chroma_t& C, const bright_t& B){
32     vpp::pixel_wise(C.img_, B.img_, C.inp_) | [&] (auto& c, const auto& b, const auto& i) {
33         if(i) {
34             c.setConstant(b[0]);
35
36             if(b[0]!=0) c.normalize();
37             else c.setConstant(1.0/256.0);
38         }
39         if(!std::isfinite(c(0))) {
40             std::cout << "NaN in RemoveColor" << std::endl;
41             std::cout << b << std::endl;
42         }
43     };
44 }
45
46 void DisplayImage(const char* wname, const chroma_t& C) {
47     cv::namedWindow(wname, cv::WINDOW_NORMAL);
48
49     // Convert Picture of double to uchar
50     vpp::image2d<vpp::uchar3> vucharimg(C.img_.domain());
51     vpp::pixel_wise(vucharimg, C.img_) | [] (auto& i, auto& n) {
52         spheremf_t::value_type v = n * (double) std::numeric_limits<unsigned char>::max();
53         vpp::uchar3 vu = vpp::uchar3::Zero();
54         vu[0]=(unsigned char) v[2];
55         vu[1]=(unsigned char) v[1];
56         vu[2]=(unsigned char) v[0];
57         i = vu;
58     };
59
60     cv::imshow(wname, vpp::to_opencv(vucharimg));
61     cv::waitKey(0);
62 }
63
64 void recombineAndShow(const chroma_t& C, const bright_t B, std::string fname, std::string wname) {
65
66     vpp::image2d<vpp::uchar3> img(C.img_.domain());
67     vpp::pixel_wise(img, C.img_, B.img_) | [] (auto& i, const auto& c, const auto& b) {
68         vpp::vdouble3 v = c * b[0] * std::sqrt(3);
69
70         double max = v.maxCoeff();
71         if(max > 1.0) v /= max;
72
73         v *= (double) std::numeric_limits<unsigned char>::max();
74
75
76         vpp::uchar3 vu = vpp::uchar3::Zero();
77         vu[0]=(unsigned char) v[2];
78         vu[1]=(unsigned char) v[1];
79         vu[2]=(unsigned char) v[0];
80         i = vu;
81     };
82     cv::namedWindow(wname, cv::WINDOW_NORMAL );
83     cv::imshow(wname, vpp::to_opencv(img));
84     cv::waitKey(0);
85
86     cv::imwrite(fname, to_opencv(img));
87 }
88
89 int main(int argc, const char *argv[])
90 {
91     Eigen::initParallel();
92
93     if (argc < 3) {

```

```

95     std::cerr << "Usage : " << argv[0] << " image [lambda] [threshold]" <
96     << std::endl;
97     return 1;
98 }
99
100 double lam=0.01;
101 double threshold=0.01;
102
103 if(argc==4){
104     lam=atof(argv[2]);
105     threshold=atof(argv[3]);
106 }
107
108 std::string fname(argv[1]);
109
110 chroma_t myChroma=chroma_t();
111 bright_t myBright=bright_t();
112
113 myBright.rgb_readBrightness(argv[1]);
114 myBright.findEdgeWeights();
115
116 myChroma.rgb_readChromaticity(argv[1]);
117 myChroma.inpaint =true;
118 myChroma.setEdgeWeights(myBright.edge_weights_);
119 myChroma.createRandInpWeights(threshold);
120 removeColor(myChroma, myBright);
121
122 // Recombine Brightness and Chromaticity parts to view Picture with \
123 // colors removed
124 recombineAndShow(myChroma, myBright, "colorless_"+fname, "Colors removed \
125 // Picture");
126
127 cfunc_t cFunc(lam, myChroma);
128 cFunc.seteps2(1e-10);
129
130 ctvmin_t cTVMIn(cFunc, myChroma);
131 cTVMIn.first_guess();
132 recombineAndShow(myChroma, myBright, "recolored_fg_"+fname, "Recolor \
133 // First Guess");
134 DisplayImage("Chromaticity First Guess", myChroma);
135
136 std::cout << "\n\n====CHROMATICITY PART====" << std::endl;
137
138 //std::cout << "Smooth picture to obtain initial state for Newton \
139 // iteration..." << std::endl;
140 //cTVMIn.smoothening(10);
141
142 std::cout << "Start TV minimization..." << std::endl;
143 cTVMIn.minimize();
144
145
146 // Recombine Brightness and Chromaticity parts of recolored Picture
147 recombineAndShow(myChroma, myBright, "recolored_"+fname, "Recolored \
148 // Picture");
149
150
151 return 0;
152 }
```

---

Colorization

Listing A.3: ./listings/dti\_tvmin\_prpt\_test3d.cpp

```

1 #include <iostream>
2 #include <cstdlib>
3 #include <string>
4 #include <sstream>
5
6 //#define TV_SPD_EXP_DEBUG
7 //#define TV_SPD_LOG_DEBUG
```

```

8
9 #define TV_DATA_DEBUG
10 // #define TV_FUNC_DEBUG
11 // #define TV_FUNC_DEBUG_VERBOSE
12 // #define TVML_TVMIN_DEBUG
13 // #define TVML_TVMIN_DEBUG_VERBOSE
14 // #define TV_VISUAL_DEBUG
15
16 #include <mtvmtl/core/algo_traits.hpp>
17 #include <mtvmtl/core/data.hpp>
18 #include <mtvmtl/core/functional.hpp>
19 #include <mtvmtl/core/tvmin.hpp>
20 #include <mtvmtl/core/visualization.hpp>
21
22 int main(int argc, const char *argv[])
23 {
24     using namespace tvmtl;
25
26     typedef Manifold< SPD, 3 > mf_t;
27     typedef Data< mf_t, 3> data_t;
28     typedef Functional<FIRSTORDER, ANISO, mf_t, data_t, 3> func_t;
29     typedef TV_Minimizer< PRPT, func_t, mf_t, data_t, OMP, 3 > tvmin_t;
30     typedef Visualization<SPD, 3, data_t, 3> visual_t;
31
32     data_t myData = data_t();
33     int nz, ny, nx;
34     nz = std::atoi(argv[2]);
35     ny = std::atoi(argv[3]);
36     nx = std::atoi(argv[4]);
37     myData.readMatrixDataFromCSV(argv[1], nz, ny, nx);
38
39
40     visual_t myVisual(myData);
41     std::stringstream fname;
42     std::string fname;
43     fname << "dti3d" << nz << "x" << ny << "x" << ny << ".png";
44     fname = "noisy_" + fname.str();
45     myVisual.saveImage(fname);
46
47     std::cout << "Starting OpenGL-Renderer..." << std::endl;
48     myVisual.GLInit("SPD(3) Ellipsoid Visualization");
49     std::cout << "Rendering finished." << std::endl;
50
51     double lam=0.7;
52     func_t myFunc(lam, myData);
53     myFunc.seteps2(0);
54
55     tvmin_t myTVMin(myFunc, myData);
56
57     std::cout << "Start TV minimization..." << std::endl;
58     myTVMin.minimize();
59
60     std::string dfname = "denoised(prpt)_" + fname.str();
61     myVisual.saveImage(dfname);
62
63     std::cout << "Starting OpenGL-Renderer..." << std::endl;
64     myVisual.GLInit("SPD(3) Ellipsoid Visualization");
65     std::cout << "Rendering finished." << std::endl;
66
67     return 0;
68 }

```

---

3D DTI TV minimization

Appendix **B**

## Derivative Computations

The following computations are based on the notation used in [22]. At the core of the computation is the following relation for the differential  $dF$  of a function  $f$ , considered as map between two matrix spaces

$$d \operatorname{vec} F(X) = \operatorname{vec} dF(X), \quad (\text{B.1})$$

where  $\operatorname{vec}$  denotes the vectorization operator  $\operatorname{vec} : \mathbb{R}^{n \times p} \rightarrow \mathbb{R}^{np}$ , which forms a vector from a matrix by column-wise stacking. In the next sections, the computation will be demonstrated for the case of the special orthogonal group. The computations for the other manifolds work analogously.

### B.1 Vectorization-Kronecker-product identities

Another important tool for the computation of derivatives are the following identities for the vectorization operator and the Kronecker product  $\otimes$ .

$$\operatorname{vec}(ABC) = (C^T \otimes A) \operatorname{vec} B \quad (\text{B.2})$$

If one of the matrices in the above product is replaced by the identity matrix  $\mathbb{1}$ , an additional set of three identities can be obtained.

$$\operatorname{vec}(AB) = (B^T \otimes A) \operatorname{vec} A \quad (\text{B.3})$$

$$= (B^T \otimes A) \operatorname{vec} \mathbb{1} \quad (\text{B.4})$$

$$= (\mathbb{1} \otimes A) \operatorname{vec} B \quad (\text{B.5})$$

$$(\text{B.6})$$

### B.2 Squared distance function on the special orthogonal group $SO(n)$

The first derivative  $\frac{\partial d^2(X,Y)}{\partial X} = -2X \log(X^T Y) =: T_4$  can be decomposed as follows

$$T_1 = X^T Y \quad (\text{B.7})$$

$$T_2 = -2X \quad (\text{B.8})$$

$$T_3 = \log T_1 \quad (\text{B.9})$$

$$T_4 = T_2 T_3. \quad (\text{B.10})$$

The derivative of the first line with respect to  $X$  is given by

$$dT_1(X) = dX^T Y \quad (\text{B.11})$$

$$d \operatorname{vec} T_1(X) = \operatorname{vec} dX^T Y \quad (\text{B.12})$$

$$= (Y^T \otimes \mathbb{1}_n) \operatorname{vec} dX^T \quad (\text{B.13})$$

$$= \underbrace{(Y^T \otimes \mathbb{1}_n) K_{nn}}_{dT_1(X)} \operatorname{vec} dX. \quad (\text{B.14})$$

Hence,

$$\frac{\partial T_1}{\partial X} = (Y^T \otimes \mathbb{1}_n) K_{nn} \quad (\text{B.15})$$

where  $K_{nn}$  denotes the so-called commutator matrix transforming the vectorization of a matrix to the vectorization of the transpose of the matrix. More details on the properties of this permutation matrix can be found in [22].

Now for the second part one has

$$dT_2(X) = -2 dX \quad (\text{B.16})$$

$$d \operatorname{vec} T_2(X) = \operatorname{vec} -2 dX = \underbrace{-2 \mathbb{1}_{n^2}}_{dT_2(X)} \quad (\text{B.17})$$

leading to the Kronecker representation

$$\frac{\partial T_2}{\partial X} = -2 \mathbb{1}_{n^2}. \quad (\text{B.18})$$

The third part yields

$$\frac{\partial T_3}{\partial X} = \frac{\partial T_3}{\partial T_1} \frac{\partial T_1}{\partial X} = d \log(Y^T \otimes \mathbb{1}_n) K_{nn}. \quad (\text{B.19})$$

Finally, only the last part is needed to put everything together. From

$$dT_3(X) = dT_2(X) T_3(X) + T_2(X) dT_3(X) \quad (\text{B.20})$$

$$d \operatorname{vec} T_2(X) = \operatorname{vec} dT_2 T_3 \operatorname{vec} T_2 dT_3 \quad (\text{B.21})$$

$$= (T_3^T \otimes \mathbb{1}_n) \operatorname{vec} dT_2 + (\mathbb{1}_n \otimes T_2) \operatorname{vec} dT_3 \quad (\text{B.22})$$

and the previous parts, one arrives at

$$\frac{\partial T_4}{\partial X} = (T_3^T \otimes \mathbb{1}_n) \frac{\partial T_2}{\partial X} + (\mathbb{1}_n \otimes T_2) \frac{\partial T_3}{\partial X}. \quad (\text{B.23})$$

Substitution of the  $T_i$  leads to the final expression presented in 2.54.

# Appendix C

## Performance metrics

In this appendix some additional performance metrics of the library are shown.

### C.1 Cache Misses

Share	Routine	Library	Share	Routine	Library
22.40	cholmod_transpose_sym	CHOLMOD	17.68	DGEMM(matrix matrix multiply)	BLAS
17.76	set_from_triplets	Eigen	17.14	DSYRK(symmetric rank-k update)	BLAS
9.35	DGEMV(matrix vector multiply)	BLAS	12.73	DTRSM(solve triangular system)	BLAS
8.96	DSYRK(symmetric rank-k update)	BLAS	11.66	set_rom_triplets(sparse initialization)	Eigen
6.22	cholmod_super_numeric	CHOLMOD	9.33	CreateCoarserGraph	METIS
6.09	DTRSV(solve linear system)	BLAS	5.68	cholmod_super_numeric	CHOLMOD

(a)  $361 \times 361$

(b)  $1280 \times 1024$

Table C.1: Share of total cache misses for IRLS minimization over  $M = \mathbb{R}^3$  (a)"Lena.jpg",  $361 \times 361$  pixel (b)"Mathematicians.jpg",  $1280 \times 1024$  pixel

Share	Routine	Library	Share	Routine	Library
9.97	set_rom_triplets(sparse initialization)	Eigen	13.77	set_rom_triplets(sparse initialization)	Eigen
8.75	clear_page	Kernel	12.72	DSYRK(symmetric rank-k update)	BLAS
5.04	memcpy_sse2_unaligned	LIBC	9.59	cholmod_super_numeric	CHOLMOD
4.55	unknown	unknown	7.34	DGEMV(matrix vector multiply)	BLAS
2.75	DGEMV(matrix vector multiply)	BLAS	7.23	DGEMM(matrix matrix multiply)	BLAS
2.41	cholmod_super_numeric	CHOLMOD	4.12	cholmod_transpose_sym	CHOLMOD

(a)  $30 \times 30$

(b)  $100 \times 100$

Table C.2: Share of cache misses for IRLS minimization over  $M = SPD(3)$  (a) Synthetic  $SPD(3)$  ,  $30 \times 30$  (b) Synthetic  $SPD(3)$  ,  $100 \times 100$

## C.2 Page Faults

Share	Routine	Library	Share	Routine	Library
30.43	cholmod_super_numeric	CHOLMOD	11.30	triplet operation	Eigen
13.07	SparseMatrix::operator=	Eigen	10.24	cholmod_super_numeric	CHOLMOD
12.33	set_from_triplets	Eigen	9.05	memcpy_sse2_unaligned	LIBC
12.25	triplet operation	Eigen	8.33	set_from_triplets	Eigen
12.13	memcpy_sse2_unaligned	LIBC	8.04	SparseMatrix::operator=	Eigen
3.54	SparseMatrix::assign	Eigen	6.12	SparseMatrix::assign	Eigen

(a)  $361 \times 361$ (b)  $1280 \times 1024$ Table C.3: Share of total page faults for IRLS minimization over  $M = \mathbb{R}^3$  (a)"Lena.jpg",  $361 \times 361$  pixel (b)"Mathematicians.jpg",  $1280 \times 1024$  pixel

Share	Routine	Library	Share	Routine	Library
23.88	unknown	unknown	20.75	SparseMatrix::operator=	Eigen
11.20	dl_relocate_object	unknown	17.41	cholmod_super_numeric	CHOLMOD
10.89	evaluateHJ	MTVMTL	15.02	evaluateHJ	MTVMTL
8.21	triplet operation	Eigen	13.65	triplet operation	Eigen
8.13	SparseMatrix::operator=	Eigen	9.37	set_from_triplets	Eigen
7.17	memset_sse2	LIBC	7.27	memcpy_sse2_unaligned	LIBC

(a)  $30 \times 30$ (b)  $100 \times 100$ Table C.4: Share of total page faults for IRLS minimization over  $M = SPD(3)$  (a) Synthetic  $SPD(3)$ ,  $30 \times 30$  (b) Synthetic  $SPD(3)$ ,  $100 \times 100$

# Bibliography

- [1] A. Barmpoutis A., B. C. Vemuri, T. M. Shepherd, and J. R. Forder. Tensor splines for interpolation and approximation of dt-mri with applications to segmentation of isolated rat hippocampi. *IEEE Trans Med Imaging*, 26(11):1537–1546, 2007. (Cited on page 56.)
- [2] D. Abrahams and A. Gurtovoy. *C++ Template Metaprogramming: Concepts, Tools, and Techniques from Boost and Beyond (C++ in Depth Series)*. Addison-Wesley Professional, 2004. (Cited on page 31.)
- [3] P. A. Absil, R. Mahony, and R. Sepulchre. *Riemannian Geometry of Grassmann Manifolds with a View on Algorithmic Computation*, volume 80. Springer Netherlands, 2004. (Cited on pages 23 and 26.)
- [4] P. A. Absil, R. Mahony, and R. Sepulchre. *Optimization algorithms on matrix manifolds*. Princeton University Press, 2009. (Cited on pages 13, 16 and 25.)
- [5] A. H. Al-Mohy, N. J. Higham, and S. D. Relton. Computing the fréchet derivative of the matrix logarithm and estimating the condition number. *SIAM Journal on Scientific Computing*, 35(4):C394–C410, 2013. (Cited on page 28.)
- [6] A. Alexandrescu. *Modern C++ Design: Generic Programming and Design Patterns Applied*. Addison-Wesley Longman Publishing Co., Inc., Boston, MA, USA, 2001. (Cited on page 31.)
- [7] S. Ali and M. Shah. A lagrangian particle dynamics approach for crowd flow segmentation and stability analysis. In *CVPR*. IEEE Computer Society, 2007. (Cited on page 54.)
- [8] V. Arsigny, P. Fillard, X. Pennec, and N. Ayache. Geometric means in a novel vector space structure on symmetric positive definite matrices. *SIAM Journal on Matrix Analysis and Applications*, 29(1):328–347, 2007. (Cited on pages 13 and 68.)
- [9] J. Canny. A computational approach to edge detection. *IEEE Transactions on Pattern Analysis and Machine Intelligence*, 8(6):679–698, 1986. (Cited on page 51.)
- [10] M. Cavegn. Total variation regularization for geometric data. *Master thesis, ETH Zürich*, 2013. (Cited on page 30.)
- [11] A. Chambolle and P.-L. Lions. Image recovery via total variation minimization and related problems. *Numerische Mathematik*, 76(2):167–188, 1997. (Cited on page 8.)
- [12] T. F. Chan, S. H. Kang, and J. Shen. Total variation denoising and enhancement of color images based on the CB and HSV color models. *Journal of Visual Communication and Image Representation*, 12(4):422–435, 2001. (Cited on page 10.)
- [13] P. L. Combettes and J.-C. Pesquet. Proximal splitting methods in signal processing. In Heinz H. Bauschke, Regina S. Burachik, Patrick L. Combettes, Veit Elser, D. Russell Luke, and Henry Wolkowicz, editors, *Fixed-Point Algorithms for Inverse Problems in Science and Engineering*, volume 49 of *Springer Optimization and Its Applications*, pages 185–212. Springer New York, 2011. (Cited on page 13.)

- [14] A. Edelman, T. A. Arias, and S. T. Smith. The geometry of algorithms with orthogonality constraints. *SIAM J. Matrix Anal. Appl.*, 20(2):303–353, 1999. (Cited on page 23.)
- [15] M. Garrigues and A. Manzanera. Video++, a modern image and video processing C++ framework. Technical report, ENSTA-ParisTech, France, 2014. (Cited on pages 37 and 42.)
- [16] P. Grohs and M. Sprecher. Total variation regularization by iteratively reweighted least squares on hadamard spaces and the sphere. Technical Report 2014-39, Seminar for Applied Mathematics, ETH Zürich, Switzerland, 2014. (Cited on pages 10, 15, 18, 30 and 62.)
- [17] N. J. Higham. Evaluating padé approximants of the matrix logarithm. *SIAM Journal on Matrix Analysis and Applications*, 22(4):1126–1135, 2001. (Cited on page 28.)
- [18] H. Karcher. Riemannian center of mass and mollifier smoothing. *Communications on Pure and Applied Mathematics*, 30(5):509–541, 1977. (Cited on pages 14 and 20.)
- [19] J. Lefevre and S. Baillet. Optical flow and advection on 2-riemannian manifolds: A common framework. *IEEE Trans. Pattern Anal. Mach. Intell.*, 30(6):1081–1092, 2008. (Cited on page 68.)
- [20] R. Lischner. *Exploring C++11*. Expert’s voice in C++. Apress, New York, 2013. (Cited on page 33.)
- [21] B. D. Lucas and T. Kanade. An iterative image registration technique with an application to stereo vision. In *Proceedings of the 7th International Joint Conference on Artificial Intelligence - Volume 2*, IJCAI’81, pages 674–679, San Francisco, CA, USA, 1981. Morgan Kaufmann Publishers Inc. (Cited on page 54.)
- [22] J. R. Magnus and H. Neudecker. *Matrix differential calculus with applications in statistics and econometrics*. J. Wiley & Sons, Chichester, New York, Weinheim, 1999. (Cited on pages 20, 77 and 78.)
- [23] M. Nägelin. Total variation regularization for tensor valued images. *Bachelor thesis, ETH Zürich*, 2014. (Cited on pages 13 and 30.)
- [24] Neuroimaging informatics technology initiative - NIfTI-1 data format. <http://nifti.nimh.nih.gov/nifti-1>. Accessed: 2015-09-25. (Cited on page 29.)
- [25] Neal Parikh and Stephen Boyd. Proximal algorithms. *Found. Trends Optim.*, 1(3):127–239, 2014. (Cited on page 13.)
- [26] P. Rodriguez and B. Wohlberg. An iteratively reweighted norm algorithm for minimization of total variation functionals. *IEEE Signal Processing Letters*, 14(12):948 – 951, 2007. (Cited on page 14.)
- [27] L. I. Rudin, S. Osher, and E. Fatemi. Nonlinear total variation based noise removal algorithms. *Physica D*, 60:259–168, 1992. (Cited on pages 8 and 10.)
- [28] H. Sato and T. Iwai. Optimization algorithms on the grassmann manifold with application to matrix eigenvalue problems. *Japan Journal of Industrial and Applied Mathematics*, 31(2):355–400, 2014. (Cited on page 23.)
- [29] Teem toolkit. <http://teem.sourceforge.net/>. Accessed: 2015-09-20. (Cited on page 41.)
- [30] T. Veldhuizen. Arrays in blitz++. In Denis Caromel, RodneyR. Oldehoeft, and Marydell Tholburn, editors, *Computing in Object-Oriented Parallel Environments*, volume 1505 of *Lecture Notes in Computer Science*, pages 223–230. Springer Berlin Heidelberg, 1998. (Cited on page 30.)
- [31] Volume image database. <http://www.volvis.org/>. Accessed: 2015-09-25. (Cited on page 52.)
- [32] A. Wedel and D. Cremers. *Stereo Scene Flow for 3D Motion Analysis*. Springer, 2011. (Cited on pages 9, 32 and 68.)

- [33] A. Weinmann, L. Demaret, and M. Storath. Total variation regularization for manifold-valued data. *SIAM Journal on Imaging Sciences*, 7(4):2226–2257, 2014. (Cited on pages 10, 13, 14 and 62.)
- [34] T. Y. Zhang and C. Y. Suen. A fast parallel algorithm for thinning digital patterns. *Commun. ACM*, 27(3):236–239, 1984. (Cited on page 54.)